Time and Spatially Resolved Photoluminescence Spectroscopy of Hot Excitons in Gallium Arsenide

Dissertation zur Erlangung des
naturwissenschaftlichen Doktorgrades
der Julius-Maximilians-Universität Würzburg

vorgelegt von

Steffen Bieker
aus Engelskirchen

Würzburg 2015

Eingereicht am: 15. Juli 2015

bei der Fakultät für Physik und Astronomie

1. Gutachter: Prof. Dr. W. Ossau

2. Gutachter: Prof. Dr. J. Geurts

3. Gutachter: Prof. Dr. M. Bayer

der Dissertation

Vorsitzender: Prof. Dr. V. Hinkov

1. Prüfer: Prof. Dr. W. Ossau

2. Prüfer: Prof. Dr. J. Geurts

3. Prüfer: Prof. Dr. R. Oppermann

im Promotionskolloquium

Tag des Promotionskolloquiums: 04. März 2016

Doktorurkunde ausgehändigt am:

List of publications

M. Beck, J. Hübner, M. Oestreich, **S. Bieker**, T. Henn, T. Kiessling, W. Ossau, and L. W. Molenkamp: *Thermodynamic origin of the slow free exciton photoluminescence rise in GaAs.* Physical Review B **93**, 081204(R) (2016). Rapid Communication.

S. Bieker, R. Stühler, T. Kiessling, W. Ossau, and L. W. Molenkamp: *Dimensional crossover of free exciton diffusion in etched GaAs wire structures.* Applied Physics Letters **107**, 122106 (2015).

S. Bieker, T. Kiessling, W. Ossau, and L. W. Molenkamp: *Correct determination of low-temperature free-exciton diffusion profiles in GaAs.* Physical Review B **92**, 121201(R) (2015). Rapid Communication.

S. Bieker, T. Henn, T. Kiessling, W. Ossau, and L. W. Molenkamp: *Spatially Resolved Thermodynamics of the Partially Ionized Exciton Gas in GaAs.* Physical Review Letters **114**, 227402 (2015).

S. Bieker, R. Pfeuffer, T. Kiessling, N. Tarakina, C. Schumacher, W. Ossau, G. Karczewski, and L. W. Molenkamp: *Polytypism and band alignment in ZnSe nanowires revealed by photoluminescence spectroscopy of embedded (Zn,Cd)Se quantum dots.* Physical Review B **91**, 125301 (2015).

S. Bieker, T. Henn, T. Kiessling, W. Ossau, and L. W. Molenkamp: *Excitonic ring formation in ultrapure bulk GaAs.* Physical Review B **90**, 201305(R) (2014). Rapid Communication.

S. Bieker, P. R. Hartmann, T. Kiessling, M. Rüth, C. Schumacher, C. Gould, W. Ossau, and L. W. Molenkamp: *Removal of GaAs growth substrates from II-VI semiconductor heterostructures.* Semiconductor Science and Technology **29**, 045016 (2014). Cover article of the issue. Featured in IOPselect.

Contents

Chapter 1

Introduction

Free excitons, i.e., Coulomb-bound pairs of electrons and holes orbiting each other, have independently been conceived by J. Frenkel and G. Wannier in the 1930s as the fundamental quantum of excitation in an ideal solid [1, 2]. However, it was only after two decades of Frenkel's and Wannier's seminal works that the existence of excitons was substantiated experimentally by a series of discrete lines in the absorption spectra of cuprous oxide crystals [3, 4]. The exciton lines emerge below the fundamental band gap energy and progressively move together towards the continuous absorption edge. This characteristic absorption signature resembles the well-known hydrogen Balmer series [5] and illustrates Wannier's conception of the exciton as the solid state analogue to the hydrogen atom.

The newly found quasiparticle has ever since attracted strong research interest, particularly in the field of condensed matter optical spectroscopy. Many different aspects of exciton physics have been addressed over the past decades, depending on the prevailing availability of optical spectroscopy and sample preparation techniques.

The work at hand is devoted to the study of *hot exciton effects* in gallium arsenide (GaAs). Being inherent to virtually all optical spectroscopy techniques involving nonresonant laser excitation and low sample temperatures, hot carrier effects have been a dominating topic since the early days of solid state physics [6]. However, the vast majority of available studies is concerned with the analysis of *hot electron* populations. We speculate that the reason for the scarceness of previous work on hot exciton effects is twofold. First, ultraclean samples allowing for the investigation of pure free exciton populations require sophisticated growth techniques and have, therefore, not been available to all researchers. Second, the temperature of a photoexcited free exciton ensemble is less readily accessible than that of an electron population.

In the present thesis we investigate the low-temperature spatiotemporal dynamics of an optically excited free exciton population in nearly defect-free GaAs. In crucial distinction from previous work, we extensively study a particular photoluminescence (PL) transition originating from the radiative annihilation of free excitons under simul-

taneous emission of two longitudinal optic (LO) phonons. It is presumably due to its inherent intensity weakness that this recombination line has rarely been studied in the past. However, investigation of the second LO-phonon replica is crucial for the quantitative assessment of hot exciton effects since its recombination line shape provides direct experimental access to the temperature of the free exciton ensemble [7, 8].

Also the Saha equation, which is the second cornerstone for the quantitative assessment of hot exciton effects, has only infrequently been considered in the past. Said equation was originally formulated in 1920 by M. Saha to describe the thermodynamics of the partially ionized hydrogen plasma in the solar chromosphere [9]. Adapted to the solid state environment, the Saha equation allows to calculate the population balance between Coulomb-bound free excitons and uncorrelated electron-hole pairs [10].

Using the second LO-phonon replica and the Saha equation to relate the precisely determined exciton temperature with the thermodynamic population balance of the partially ionized exciton gas, we quantitatively address the impact of hot exciton effects on the low-temperature photoluminescence properties of free excitons in GaAs.

We first address a fundamental long-standing question, i.e., the origin of the slow free exciton photoluminescence rise with respect to an ultrashort laser excitation pulse. To this end, we investigate for the first time the PL response of the free exciton second LO-phonon replica in order to circumvent the inherent interpretation ambiguities of the previously investigated zero-phonon line. We show that the Saha equation directly translates experimental cooling curves obtained from a time-resolved line shape analysis of the second LO-phonon replica into the buildup of a free exciton population. Only after sufficient cooling of the initially hot photocarrier cloud does the population balance shift from unbound electron-hole pairs to the free exciton state, thereby naturally explaining the delayed free exciton PL onset. Our analysis provides a coherent picture of the time evolution of an optically excited hot photocarrier population, which in bulk GaAs obviates consideration of the recently proposed Coulomb-correlated electron-hole plasma [11, 12].

We conclude our time-domain studies by addressing one aspect of the free exciton photoluminescence kinetics that is obscured in typical time-resolved PL experiments. Rather than ultrafast optical excitation, here we use $\approx 100\,\mathrm{ns}$ long laser pulses to drive the exciton system into a steady-state regime. After switching off the pump pulse, the free exciton PL intensity exhibits a pronounced increase with respect to the emission intensity during optical excitation. At high pump powers, this PL overshoot monitors the relaxation of large K vectors to the radiative zone, a process which is normally masked by the "thermodynamics-mediated" overall time evolution of the optically excited carrier cloud.

Having established the impact of hot exciton effects on the free exciton photoluminescence kinetics, we demonstrate that local heating in the carrier system also critically affects the diffusion of free excitons. We use a tightly focused laser spot to locally excite a packet of free excitons and trace its diffusive expansion by the

spatially resolved emission intensity of the free exciton second LO-phonon replica. We demonstrate that intrinsic steady-state exciton diffusion profiles, which are correctly described by the commonly used formulation of the photocarrier diffusion equation, are only observed under strictly resonant optical excitation. Slightly off-resonant excitation inevitably causes local heating at the pump spot, which results in severe distortions of the experimental diffusion profiles.

Using resonant optical excitation, we study the impact of geometric constraints on the exciton diffusion process. We, therefore, investigate the steady-state free exciton diffusion profiles in etched GaAs wire structures of various widths. We observe a dimensional crossover when the lateral wire width falls below the free exciton diffusion length.

The final two chapters of the thesis are devoted to our investigation of excitonic ring formation in bulk GaAs. At low sample temperatures we observe macroscopic free and bound exciton photoluminescence rings around a focused laser excitation spot. Such ring structures have recently been observed in related spatially resolved photoluminescence studies of indirect excitons in electrically biased coupled quantum wells [13, 14]. In the ongoing quest for excitonic Bose-Einstein condensation [15–17], the observation of macroscopic pattern formation was initially speculated to hint towards a macroscopically ordered phase of the excitons and has stimulated a surge of spatially resolved photoluminescence studies on these structures [18–33]. Here we demonstrate that free exciton ring formation in bulk GaAs is not related to Bose-Einstein condensation, but rather consistently explained by the spatially dependent thermodynamics of the partially ionized exciton gas described by the Saha equation. We directly determine pump-induced temperature gradients in the carrier system from spatially resolved line shape analyses of the second LO-phonon replica and show that the local population balance between free excitons and unbound electron hole-pairs naturally explains the emergence of free exciton ring structures.

The present thesis demonstrates that in combination with the exciton temperature obtained from the second LO-phonon replica, Saha's equation yields a concise yet comprehensive picture of the time and spatially resolved photoluminescence response of a photoexcited hot exciton cloud in high-purity GaAs.

Part I

Fundamentals, methods, and materials

Chapter 2

Fundamentals of hot excitons in cold semiconductors

The purpose of the present chapter is to provide the reader with the fundamental properties of hot excitons in bulk semiconductors. We will frequently refer to these fundamentals during our later interpretation and discussion of experimental results.

We first recall the basic crystallographic and electronic properties of bulk gallium arsenide (GaAs), which serves as the model system for the investigation of hot exciton effects in direct band gap semiconductors throughout this thesis. We review the electronic structure of the Wannier exciton and proceed with a discussion of free exciton luminescence in GaAs. Special attention is given to the second LO-phonon replica of the free exciton transition, whose recombination line shape provides direct experimental access to the temperature of a thermalized exciton ensemble. This particular transition enables the quantitative assessment of hot exciton effects.

We next discuss the thermodynamic equilibrium between Coulomb-bound free excitons and the uncorrelated electron-hole plasma (EHP). This population balance, which is described by the Saha equation, allows for a quantitative modeling of the delayed free exciton PL onset and of the free exciton ring formation effect.

The last section of the chapter is devoted to a discussion of photocarrier heating by nonresonant optical excitation. The heating of optically excited excitons, i.e., the discrepancy between the exciton temperature and that of the crystal lattice, is key to the interpretation of all experimental results presented in this thesis. We review influential previous works concerned with the investigation of related hot electron effects, which are qualitatively portable to an optically excited free exciton population. We conclude the chapter with a brief discussion of a representative data set that provides a particularly instructive understanding of the interplay between photocarrier heating and excess energy relaxation. It is this competition between heating and cooling that governs the stationary electron temperature in optically excited semiconductors.

2.1 Crystal structure and electronic band dispersion in GaAs

Gallium arsenide is the most extensively studied material system among the III-V semiconductor family and probably the most technologically important compound semiconductor [34, 35]. All results presented in this thesis are obtained on one of two high-purity epitaxial GaAs samples, which will serve as the model systems for the investigation of hot exciton effects in direct band gap semiconductors. We, therefore, review in the present section the fundamental crystallographic and electronic properties of the material system under study.

Gallium arsenide is composed to equal numbers of group-III gallium (Ga) and group-V arsenic (As) atoms. Like most III-V binary compound semiconductors, GaAs crystallizes in the zinc blende structure, in which two interpenetrating face-centered cubic sub-lattices of Ga and As atoms are displaced by $\sqrt{3}/4$ of the lattice constant $a_0 = 5.65\,\text{Å}$ [34] along the unit cell diagonal [36]. The unit cell of the GaAs crystal lattice is schematically depicted in Fig. 1 (a). Because of the diamond-like coordination of the lattice atoms, each Ga atom is tetrahedrally surrounded by four As atoms and vice versa. The GaAs crystal bonds are derived from sp^3-hybridized atomic orbitals and possess predominantly covalent character.

The GaAs electronic band structure is archetypic of zinc blende-type semiconductors. A simplified schematic of the band dispersion in the vicinity of the Brillouin zone center is depicted in Fig. 1 (b). The doubly degenerate minimum of the lowest unoccupied s-type Γ_6 conduction band (CB) and the fourfold degenerate maximum of the highest occupied p-type Γ_8 valence band (VB) [34] coincide at the Γ point $\mathbf{k} = (0,0,0)$, rendering GaAs a direct band gap semiconductor. The fundamental $\Gamma_6 \rightarrow \Gamma_8$ energy gap in bulk GaAs is $E_g = 1.519\,\text{eV}$ at liquid helium temperature [37].

Away from the Brillouin zone center, the fourfold degeneracy of the VB maximum is lifted and the Γ_8 band separates into two valance bands of different curvature [Fig. 1 (b)]. The upper band exhibiting larger effective mass is referred to as the heavy hole (HH) band. Conversely, the lower band is referred to as the light hole (LH) band. In contrast to the p-type Γ_8 VB wave functions, the s-type Γ_7 VB wave functions do not experience spin orbit coupling [38]. The Γ_7 VB is, therefore, separated by $\Delta_{\text{SO}} = 0.34\,\text{eV}$ from the (HH), (LH) bands [37] and referred to as the spin-split-off (SO) band. Since the SO band is fully occupied at low sample temperatures and since the optical excitation energies in our experiments are too low to excite electrons from the spin-split-off band into the conduction band, the SO band may be disregarded in the interpretation of our experimental results. For the same reason, the GaAs satellite conduction band valleys at the X and L points located $\approx 460\,\text{meV}$ and $310\,\text{meV}$ above the lowest conduction band minimum [39] are also disregarded from consideration.

In crude approximation, the conduction and valence band extrema in the vicinity

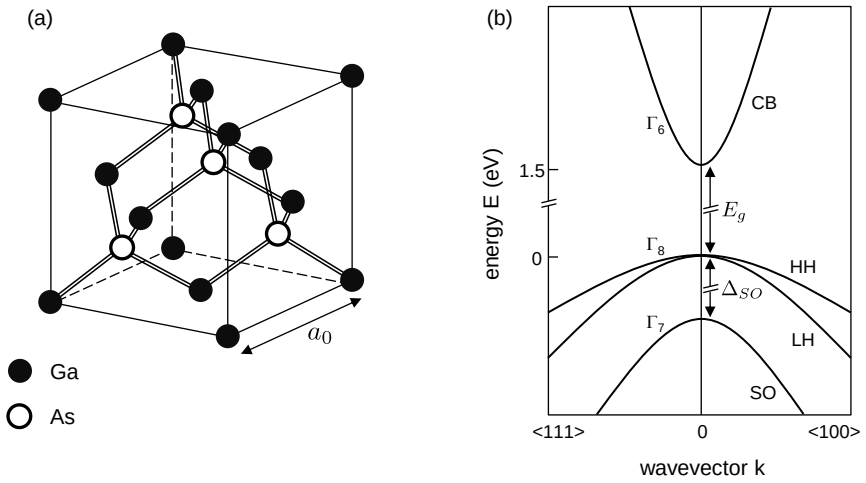

Figure 1: (a) Ball-and-stick model of the GaAs unit cell. Each gallium atom is tetrahedrally surrounded by four arsenic atoms and vice versa. Adapted from Ref [38]. (b) Schematic of the GaAs band structure in the vicinity of the Γ point. "Warping" of the valence bands is disregarded in this simplified sketch.

of the Γ point are described by parabolic dispersion relations

$$E_{CB} = E_g + \frac{\hbar^2 \mathbf{k}^2}{2m_e} \tag{2.1a}$$

$$E_{VB} = -\frac{\hbar^2 \mathbf{k}^2}{2m_{hh,lh}} \tag{2.1b}$$

with the maximum of the VB arbitrarily chosen at $E = 0$ [Fig. 1 (b)]. In this simplified picture, electrons and holes behave like free particles of charge $-|e|$ (electrons) and $+|e|$ (holes), which move freely through the crystal. The effective masses are given by the curvature of the respective CB and VB dispersion relation $\hbar^2/m_i = d^2E_i(\mathbf{k})/d\mathbf{k}^2$. For bulk GaAs at liquid helium temperature, the electron, heavy hole, and light hole effective masses are $m_e = 0.067m_0$, $m_{hh} = 0.51m_0$, and $m_{lh} = 0.082m_0$ [37] with $m_0 = 9.11 \times 10^{-31}$ kg the fee electron mass.

The GaAs conduction band is indeed nearly parabolic at the Γ point, such that eq. (2.1a) provides a good description of the CB dispersion relation. The situation is, however, more involved for the HH and LH bands. A more complete description of the valence bands than the approximation in eq. (2.1b) must take into account non-spherical contributions to the $E_{VB}(\mathbf{k})$ dispersion relations [38, 40]

$$E_{VB}(\mathbf{k}) = -\frac{\hbar^2}{2m_0} \times \left[A\mathbf{k}^2 \pm \sqrt{B^2\mathbf{k}^4 + C^2(k_x^2k_y^2 + k_y^2k_z^2 + k_x^2k_z^2)} \right] \tag{2.2}$$

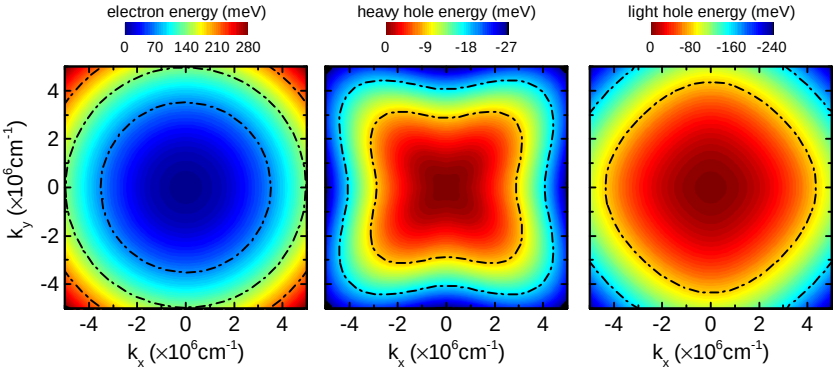

Figure 2: Contour plots of the CB, HH, and LH dispersion relations in bulk GaAs. In contrast to the CB, the surfaces of constant hole energy in the VBs are warped spheres, rendering the hole effective masses **k** vector dependent. The energy scales are chosen such that the band extrema are located at $E = 0$. Reversed color gradients indicate the opposite curvature of the conduction and valence bands.

where the plus sign corresponds to the LH band and the minus sign to the HH band, respectively. Equation (2.2) states that both branches of the Γ_8 valence band are parabolic along any direction in **k**, but the anisotropy $C \neq 0$ renders the effective masses **k**-vector dependent. The warping parameters A, B, C are related to the Kohn-Luttinger parameters γ_1, γ_2, γ_3 [41] by $A = \gamma_1$, $B = 2\gamma_2$, and $C = 12(\gamma_3^2 - \gamma_2^2)$ [40].

Figure 2 displays contour plots of the CB, HH, and LH dispersion relations in the $k_x - k_y$ plane, calculated for the GaAs Luttinger parameters $\gamma_1 = 6.98$, $\gamma_2 = 2.06$, and $\gamma_3 = 2.93$ [35]. Dash-dotted lines indicate surfaces of constant energy, which are warped spheres for the case of the heavy hole and light hole valence bands [6, 38]. We will discuss the impact of valence band warping on the excitation wavelength dependence of the stationary photocarrier temperature in optically excited semiconductors in section 2.5.3.

2.2 The Wannier exciton in bulk semiconductors

In optically excited semiconductors, incident photons of sufficient energy produce free electrons in the conduction band and free holes in the valence bands. The initially unbound charge carriers move independently through the crystal and their kinetic energies are given by $\mathbf{p}_e^2/(2m_e)$ and $\mathbf{p}_h^2/(2m_h)$, respectively, with $\mathbf{p}_e = -i\hbar\nabla_e$ and $\mathbf{p}_h = -i\hbar\nabla_h$ the electron and hole momenta [36]. The attractive Coulomb force between oppositely charged carriers eventually leads to the binding of individual electrons and holes into a new species of charge-neutral quasiparticles, which we refer to as excitons [42]. In such Coulomb-bound electron-hole pairs, both particles orbit around each other. Depending on the radius of the bound complex, we distinguish

between Wannier-Mott excitons and Frenkel excitons. The spatial extent of a Frenkel exciton is comparable to the size of a crystal unit cell with the electron-hole pair localized at a specific lattice site. This type of excitons is mostly observed in molecular crystals, polymers, and biological molecules [43]. The Wannier-Mott exciton rather extends over a large number of crystal unit cells [Fig. 3 (a)] and, in contrast to the Frenkel exciton, migrates freely through the crystal. Since this exciton species is characteristic of semiconductors [43], we are in this thesis exclusively concerned with Wannier-Mott excitons and use the less specific term (free) exciton interchangeably.

We next review the electronic structure of the free exciton state in a bulk semiconductor. Because of the large spatial extent of the exciton compared with the size of the crystal unit cell, the electrons and holes are reasonably assumed to move in a uniform dielectric medium [43]. Considering the mutual Coulomb interaction between the oppositely charged particles and neglecting exchange interaction effects [44, 45], the Hamiltonian of the bound electron-hole pair reads [42]

$$\mathscr{H}_X = -\frac{\hbar^2\nabla_e^2}{2m_e} - \frac{\hbar^2\nabla_h^2}{2m_h} - \frac{e^2}{4\pi\varepsilon_0\kappa_0|\mathbf{r}_e-\mathbf{r}_h|}\ . \tag{2.3}$$

Here, ε_0 is the permittivity of free space, κ_0 denotes the static dielectric constant of the semiconductor, and $\mathbf{r}_e$, $\mathbf{r}_h$ are the electron and hole spatial coordinates. Inspection of eq. (2.3) reveals that the Hamiltonian $\mathscr{H}_X$ of the Coulomb-attracted electron-hole pair in a semiconductor is conceptually identical to the Hamiltonian of the hydrogen atom [46]

$$\mathscr{H}_H = -\frac{\hbar^2\nabla_e^2}{2m_0} - \frac{\hbar^2\nabla_p^2}{2m_p} - \frac{e^2}{4\pi\varepsilon_0|\mathbf{r}_e-\mathbf{r}_p|} \tag{2.4}$$

with the bare electron mass m_0, the proton mass m_p, and the electron and proton spatial coordinates $\mathbf{r}_e$, $\mathbf{r}_p$. In the hydrogen atom, the electron and the ≈ 2000 times heavier proton orbit around each other. The situation is analogous to the Wannier exciton in a semiconductor, in which an electron of effective mass m_e and a hole of effective mass m_h circulate around each other. The close resemblance between both scenarios allows to directly estimate the exciton radius and binding energy by rescaling the characteristic length and energy scales of the hydrogen atom (the Bohr radius and the Rydberg energy) by substituting the effective masses and considering the dielectric constant of the semiconductor [47]. For the sake of clarity, we reproduce in the following the main steps and results of the quantum mechanical hydrogen problem [48, 49], adapted for the Coulomb-attracted electron-hole pair in a semiconductor [38, 42].

We first introduce two new coordinates, the center-of-mass coordinate $\mathbf{R}$ and the relative coordinate $\mathbf{r}$, as

$$\mathbf{R} = \frac{m_e\mathbf{r}_e + m_h\mathbf{r}_h}{m_e+m_h}\ ,\quad \mathbf{r} = \mathbf{r}_e - \mathbf{r}_h. \tag{2.5}$$

With the substitution eq. (2.5), the center-of-mass motion of the entire free exciton decouples from the relative motion of its constituents. The exciton wave function then factorizes [42]

$$\psi_X(\mathbf{R},\mathbf{r}) = \Phi(\mathbf{R})\varphi(\mathbf{r}) \tag{2.6}$$

and the Schrödinger equation $\mathscr{H}_X\psi_X = E_X\psi_X$ decomposes into two equations, each of which involves only one of the new coordinates [38]

$$\left(-\frac{\hbar^2}{2m_X}\right)\nabla^2_{\mathbf{R}}\Phi(\mathbf{R}) = E_R\Phi(\mathbf{R}) \tag{2.7a}$$

$$\left(-\frac{\hbar^2}{2\mu_X}\nabla^2_{\mathbf{r}} - \frac{e^2}{4\pi\varepsilon_0\kappa_0 r}\right)\varphi(\mathbf{r}) = E_r\varphi(\mathbf{r}). \tag{2.7b}$$

Here, $m_X = m_e + m_h$ is the effective exciton mass and $\mu_X = 1/(m_e^{-1} + m_h^{-1})$ the reduced exciton mass. The total energy of the exciton is given by the sum $E_X = E_R + E_r$.

Equation (2.7a) is analogous to the Schrödinger equation of a free particle in a semiconductor [36] and describes the motion of the exciton through the crystal, which is characterized by a wave vector $\mathbf{K}_X$. The wave function and the kinetic energy associated with the center-of-mass motion are given by [38]

$$\Phi(\mathbf{R}) \propto e^{i\mathbf{K}_X\mathbf{R}}\ ,\quad E_R = \frac{\hbar^2 K_X^2}{2m_X}\ . \tag{2.8}$$

Conversely, equation (2.7b) describes the orbiting motion of the negatively charged electron and the positively charged hole around each other. The attractive Coulomb potential depends only on the modulus of the relative coordinate $r = |\mathbf{r}|$, i.e., the radial distance between the electron and the hole. Transformation to spherical coordinates (r,θ,φ), therefore, leads to a factorization of the wave function $\varphi(\mathbf{r})$ of the form

$$\varphi(\mathbf{r}) = R_{nl}(r)Y_{lm}(\theta,\varphi). \tag{2.9}$$

The solution to the Schrödinger equation (2.7b) for the relative coordinate is worked out in standard quantum mechanics textbooks [48, 49]; $R_{nl}(r)$ denote the associated Laguerre polynomials and $Y_{lm}(\theta,\varphi)$ are the spherical harmonic functions. From the set of three quantum numbers (n,l,m), the eigenenergy E_r depends only on the principal quantum number n [38]

$$E_r = E_r(\infty) - \frac{Ry^*}{n^2}\ ,\quad Ry^* = \left(\frac{\mu_X}{m_0\kappa_0^2}\right)\times 13.6\,\mathrm{eV}. \tag{2.10}$$

When both particles are infinitely separated from each other, the attractive Coulomb force tends to zero and the energy $E_r(\infty)$ of the electron-hole pair is then equal to the band gap energy E_g. By analogy with the Rydberg constant of the hydrogen atom

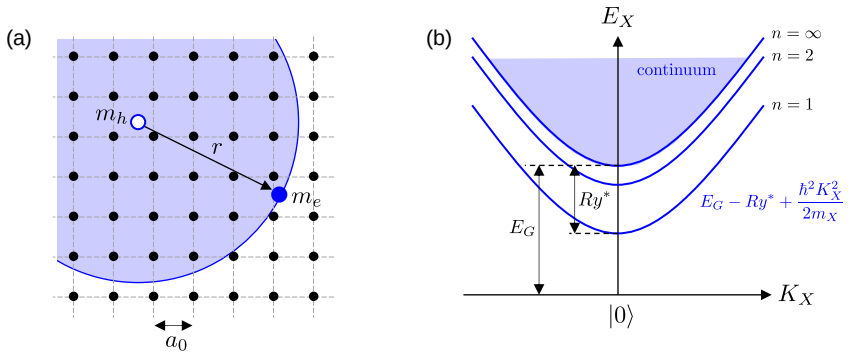

Figure 3: (a) The electron and the hole in a Wannier exciton are bound by Coulomb attraction and orbit around each other. The spatial extent of the exciton exceeds the size of the unit cell by several orders of magnitude, such that the constituting electron and hole effectively move in a uniform dielectric medium. (b) Energy scheme of a free exciton in a bulk semiconductor. $|0\rangle$ denotes the ground state of the crystal with no excitons present and Ry^* is the free exciton binding energy. After [47].

$Ry(H)$, the free exciton binding energy is termed the exciton Rydberg constant Ry^*. As discussed above, the scaling factor $\mu_X/(m_0\kappa_0^2)$ relates the exciton Rydberg energy Ry^* to the hydrogen Rydberg constant $Ry(H) = 13.6\,\text{eV}$. Combining the results of eqs. (2.8) and (2.10), we arrive at the following expression for the total energy $E_X(K_X)$ of a Wannier exciton that moves freely in a bulk semiconductor [Fig. 3 (b)]

$$E_X = E_g - \frac{Ry^*}{n^2} + \frac{\hbar K_X^2}{2m_X}\,, \quad n = 1,2,3,\ldots \tag{2.11}$$

Throughout this thesis, we are exclusively concerned with the energetic ground state of the free exciton. The experimentally determined free exciton binding energy in GaAs is $Ry^* = 4.2\,\text{meV}$ [50] and the $n = 1$ free exciton Bohr radius is $a_B = 112\,\text{Å}$ [38].

2.3 Free exciton luminescence in GaAs

2.3.1 Zero-phonon line

A free exciton that is not captured by an impurity decays radiatively after a typical lifetime of a few ns [51, 52]. The transition in the photoluminescence (PL) spectrum that results from the direct annihilation of free excitons is termed the *free exciton zero-phonon line* (FX). This PL transition should be contrasted with recombination paths that involve additional quasiparticles (e.g., phonons) during the luminescence process. Of particular interest throughout this thesis is the free exciton second LO-phonon replica, which we will discuss in the following section 2.3.2.

A strict K vector selection rule applies to the zero-phonon line. Both the free exciton energy E_X and momentum $\hbar K_X$ must be imparted to the emitted photon during the luminescence process. Because of the relatively small photon wave vectors k_ν, only a subset of the entire free exciton ensemble close to the Brillouin zone center with $K_X = k_\nu \approx 0$ contributes to the intensity of the (FX) line [52–55]. Particularly hot excitons that exhibit relatively large wave vectors are protected against radiative decay and are thus not visible in the zero-phonon line. Consequently, the emission intensity of the (FX) transition is not a direct measure of the actual free exciton density in the crystal. The interpretation of time and spatially resolved PL signals detected on the zero-phonon line is, therefore, inherently ambiguous.

In direct band gap semiconductors, the coupling between excitons and photon modes leads to the emergence of new eigenstates, the so-called exciton polaritons [56]. Although polariton effects modify, e.g., the reflectance spectrum of bulk semiconductors [57] and the recombination line shape of the (FX) zero-phonon line [58, 59], it is not necessary to consider polariton effects for the interpretation of our experimental results presented in this thesis. Because of the 0.08 meV L-T splitting in GaAs, which is smaller than the homogeneous linewidth of the free exciton resonance, the polariton concept plays only a minor role for the here investigated spatiotemporal *dynamics* of an optically excited free exciton population [60, 61].

2.3.2 LO phonon-assisted radiative decay

A competing process to the direct annihilation of free excitons is the radiative decay under simultaneous emission of integral multiples of LO phonons [7, 47]. The resulting transitions in the PL spectrum are referred to as *free exciton LO-phonon replicas*. We discuss in this section the spectral line shape and the particular significance of the two-LO phonon sideband for the studies presented in this thesis.

Because of energy conservation during the luminescence process, the LO-phonon sidebands of the free exciton transition are redshifted by integral multiples of the LO phonon energy with respect to the zero-phonon line (FX) and appear at photon energies

$$h\nu = E_X(K_X) - m\hbar\Omega_{\mathrm{LO}}\ , \quad m = 1, 2, 3... \tag{2.12}$$

in the PL spectrum. In GaAs, the LO phonon energy at 4.2 K lattice temperature is $\hbar\Omega_{\mathrm{LO}} = 36.8\,\mathrm{meV}$ [37]. The radiative decay of free excitons via the first (second, third,...) phonon replica requires the participation of a third (fourth, fifth,...) quasiparticle. The probability for such phonon-assisted radiative recombination of free excitons is drastically decreased with respect to the probability to decay by the zero-phonon first-order process [47]. Moreover, exciton-LO phonon coupling is mediated by the Fröhlich interaction, whose coupling strength scales with the degree of ionicity of the crystal lattice [38]. Most studies of free exciton phonon replicas are, therefore,

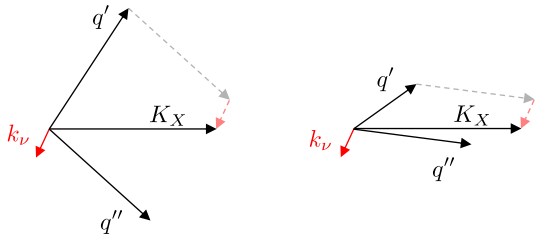

Figure 4: Free excitons with arbitrary wavevectors K_X can radiatively recombine under simultaneous emission of two LO phonons with wavevectors q' and q''. For each exciton wave vector K_X, a large number of combinations $\{K_X, q', q''\}$ exist which satisfy momentum conservation. The two phonon wavevectors q', q'' can always add up such that they compensate the center-of-mass momentum of the recombining free exciton. The strict K vector selection rule applicable to the zero-phonon line is, therefore, fully relaxed for the $(FX) - 2\hbar\Omega_{\mathrm{LO}}$ phonon replica.

performed on ionic crystals [62–64] or semiconductors with partly ionic bonds, e.g., II-VI compound semiconductors [7, 53, 65] and gallium nitride (GaN) [66–70].

Because of the predominantly covalent nature of the GaAs crystal bonds, the emission intensity of free exciton phonon sidebands is extremely weak in this material system. Virtually no literature exists[1] that reports on the observation or analysis of the $(FX) - 2\hbar\Omega_{\mathrm{LO}}$ replica in bulk GaAs. Undeterred by the lack of previous work on the $(FX) - 2\hbar\Omega_{\mathrm{LO}}$ replica and motivated by the fact that the spectral line shape of this particular transition provides direct experimental access to the temperature of a photoexcited exciton ensemble, we strive for a comprehensive analysis of the inherently weak free exciton second LO-phonon replica in this thesis.

The recombination line shape of the free exciton second LO-phonon replica is crucially predetermined by momentum conservation during the luminescence process. In a two-phonon radiative process, the exciton with wave vector K_X emits two LO phonons with wave vectors q', q'' and a photon with wave vector k_ν. In distinction from the zero-phonon radiative process, which is only accessible for excitons with $K_X = k_\nu \approx 0$, excitons with considerably larger wave vectors $K_X \gg k_\nu$ can decay radiatively by simultaneous emission of two LO phonons [7, 47, 53]. The situation is schematically depicted in Fig. 4. For each exciton wave vector K_X, a large number

[1] D. C. Reynolds et al. investigate phonon sidebands in the photoluminescence spectra of high-purity GaAs [71] and allegedly report on the first observation of excitonic phonon replicas in $Al_xGa_{1-x}As$ alloys [72]. Both studies are limited to the one-LO phonon assisted transitions and do not report on the observation of the $(FX) - 2\hbar\Omega_{\mathrm{LO}}$ replica. J. Aaviksoo et al. [73] derive a qualitative statement on the exciton temperature in a high-purity GaAs sample from inspection of the line shape of the free exciton *first* LO-phonon replica. The one-LO phonon assisted recombination line has also been observed in a high-purity GaAs sample investigated in Ref [59]. We are, however, not aware of any previous studies that investigate the $(FX) - 2\hbar\Omega_{\mathrm{LO}}$ transition in GaAs to determine the exciton temperature.

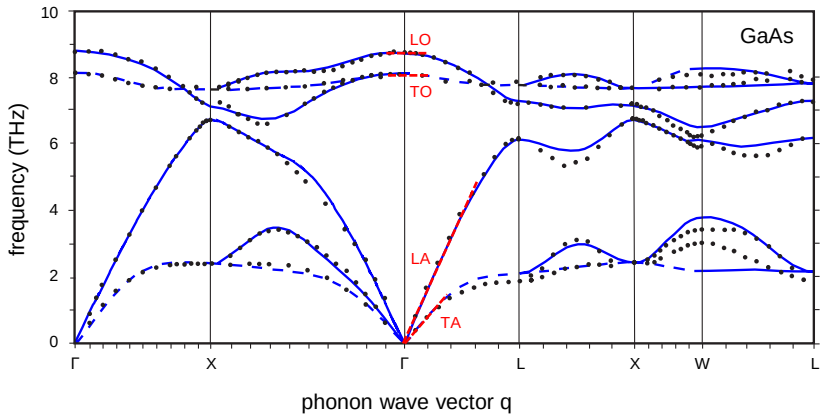

Figure 5: Phonon dispersion relation in GaAs along high-symmetry axes at $T_L = 12\,\mathrm{K}$. Data points are obtained by inelastic neutron scattering, solid lines indicate the calculation results of a rigid-ion model [74]. The energy of the LO phonon mode in bulk GaAs is 36.8 meV. The optical phonon branches are nearly dispersionless at the Brillouin zone center. Adapted from [38].

of combinations $\{K_X, k_v, q', q''\}$ exist that satisfy momentum conservation during the luminescence process. To arrive at a prediction for the $(FX) - 2\hbar\Omega_{\mathrm{LO}}$ line shape, it is important to consider two interim results.

1. It was initially pointed out by E. Gross et al. [7] that the probability for radiative decay under simultaneous emission of two LO phonons is equal for all free excitons, irrespective of their wave vector K_X. The strict K vector selection rule applicable to the (FX) zero-phonon line is hence fully relaxed for the second LO-phonon replica. This result, which was purely derived from experiment, has later been verified by B. Segall and G. D. Mahan by a theoretical treatment of the phonon assisted recombination process [8].

2. Inspection of the GaAs phonon spectrum (Fig. 5) reveals that the optical phonon branches are nearly dispersionless in the vicinity of the Γ point. The free exciton wave vectors are typically restricted to the center of the Brillouin zone, such that the LO phonons emitted during the phonon-assisted luminescence process are in good approximation monochromatic [7, 53].

Since all free excitons irrespective of their K vector contribute equally to the second LO-phonon replica and since all emitted phonons share the same energy, the recombination line shape of the $(FX) - 2\hbar\Omega_{\mathrm{LO}}$ transition directly reflects the density of occupied states among the free exciton population [7, 8, 47, 53]. From the parabolic center-of-mass kinetic energy dispersion $E_X(K_X)$ [eq. (2.11)], we infer a free exciton density of states $D_X(E_X) \propto \sqrt{E_X}$ and use Boltzmann statistics to describe the kinetic energy

distribution function of the thermalized exciton ensemble.[2] The density of occupied states, and therefore the recombination line shape of the free exciton second LO-phonon replica, is given by the product

$$I(h\nu) \propto \sqrt{h\nu - (E_g - Ry^* - 2\hbar\Omega_{\mathrm{LO}})} \times \exp\left[-\frac{h\nu - (E_g - Ry^* - 2\hbar\Omega_{\mathrm{LO}})}{k_B T_X}\right]. \quad (2.13)$$

Equation (2.13) states the important result that the well-defined line shape of the $(FX) - 2\hbar\Omega_{\mathrm{LO}}$ transition is exclusively determined by the temperature T_X of the free exciton ensemble. We, therefore, directly obtain T_X from a Maxwellian line shape analysis of the free exciton second LO-phonon replica.[3]

To illustrate the result of eq. (2.13), we show in Fig. 6 the $(FX) - 2\hbar\Omega_{\mathrm{LO}}$ PL spectra of a GaAs epilayer (sample B, cf. section 4.2) at three representative lattice temperatures. Solid blue lines indicate the respective Maxwellian fits to the data. The asymmetric line shape of the second LO-phonon replica resembles the density of occupied states $\propto \sqrt{E} \times \exp[-E/(k_B T_X)]$ in the exciton population. At elevated lattice temperatures, the broadening of the transition indicates very instructively the increased occupation of high-energy states in the tail of the Boltzmann distribution function. We furthermore note that at low lattice temperatures, the exciton temperature T_X is significantly increased with respect to T_L. This overheating is typical for optically excited semiconductors at low lattice temperatures. We will discuss the photocarrier heating effect and its characteristic dependence on various excitation parameters in section 2.5.

2.4 Thermodynamics of the partially ionized exciton gas

We previously employed in section 2.2 the conceptual analogue between the hydrogen atom and a Wannier exciton in a bulk semiconductor to derive the free exciton energy structure. In the present section, we repeatedly exploit the analogy with atomic hydrogen to derive an equation that describes the temperature dependent ionization equilibrium of a free exciton population.

[2] As we will later discuss in section 2.5, an optically excited exciton population thermalizes within a couple of ps [75] by efficient exciton-exciton and exciton-free carrier scattering. We, therefore, assume thermalized distribution functions for all applied excitation conditions on all experimentally accessible time scales. The kinetic energy distribution function is then described by Boltzmann statistics with a well-defined temperature T_X.

[3] For the sake of completeness, we note that the exciton temperature T_X can in principle also be obtained from a line shape analysis of the *first* LO-phonon replica of the free exciton transition, which is given by $I \propto E^{3/2} \times \exp[-E/(k_B T_X)]$ [7, 67]. Although the one-LO phonon assisted recombination line offers the advantage of being more intense than the $(FX) - 2\hbar\Omega_{\mathrm{LO}}$ line, the severe distortion by the spectrally nearby (e, A^0) and (D^0, A^0) transitions renders a robust line shape analysis of the first LO-phonon replica unfeasible.

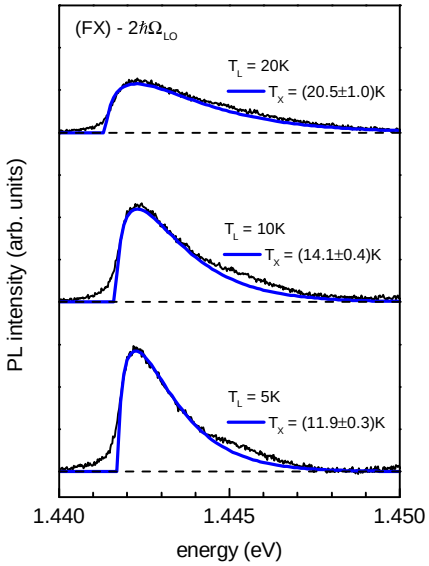

Figure 6: Representative Maxwellian line shape analyses of the free exciton second LO-phonon replica, from which the exciton temperature T_X is obtained. The broadening of the $(FX) - 2\hbar\Omega_{\mathrm{LO}}$ transition reflects very instructively the occupation of high-energy states in the tail of the Boltzmann distribution function at elevated lattice temperatures. The fitting range is $1.442\,\mathrm{eV} \leq h\nu \leq 1.444\,\mathrm{eV}$.

In optically excited semiconductors at finite temperatures, thermal breakup of free excitons into uncorrelated electron-hole pairs

$$X \overset{\Delta E}{\rightleftharpoons} e + h, \quad \Delta E = Ry^* = 4.2\,\mathrm{meV}$$

leads to the coexistence of two photocarrier sub-ensembles, i.e., Coulomb-bound excitons and the uncorrelated electron-hole plasma (EHP). By analogy with the ionization equilibrium of atomic hydrogen

$$H \overset{\Delta E}{\rightleftharpoons} H^+ + e, \quad \Delta E = Ry(H) = 13.6\,\mathrm{eV}$$

described by the Saha equation [9], a related equation can be derived that describes the thermodynamic population balance of a partially ionized exciton gas in a semiconductor. This ionization equilibrium between excitons and unbound charge carriers is crucially influenced by the exciton temperature T_X and the photocarrier pair density n_0 in the crystal.

We reproduce here a derivation of the Saha equation, which is obtained from a consideration of the canonical partition function of the partially ionized exciton gas [76]. For the sake of illustration, we first consider the particularly instructive

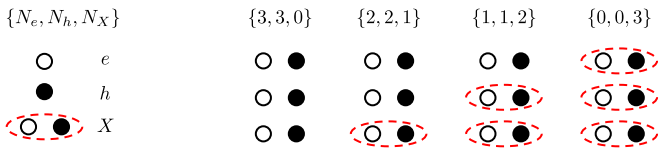

Figure 7: Schematic of the four possible states of an ensemble of three electron-hole pairs considered in the partition function Z_{tot}. All pairs may bind into free excitons or thermally dissociate into uncorrelated electron-hole pairs.

case of a population of only three electron-hole pairs. The four possible states of the entire photocarrier population are depicted in Fig. 7. The ensemble may be completely or partially ionized, or all electron-hole pairs may be bound into free excitons. The ensemble partition function Z_{tot} is given by the sum of the individual partition functions for all allowed configurations depicted in Fig. 7 [77]

$$Z_{\text{tot}} = \frac{Z_e^3}{3!}\frac{Z_h^3}{3!} + \frac{Z_e^2}{2!}\frac{Z_h^2}{2!}\frac{Z_X^1}{1!} + \frac{Z_e^1}{1!}\frac{Z_h^1}{1!}\frac{Z_X^2}{2!} + \frac{Z_X^3}{3!}. \tag{2.14}$$

When normalized to Z_{tot}, each summand in eq. (2.14) describes the relative probability for the system to occupy the respective state. Factorials in the denominators account for the indistinguishability of electrons, holes, and free excitons, respectively. Z_e, Z_h, and Z_X denote the one-particle partition functions of individual electrons and holes with energy $p^2/2m_{e,h}$ and of free excitons with energy $p^2/2m_X - Ry^*$. Neglecting internal degeneracy factors,[4] the individual partition functions are given by [77]

$$Z_{e,h} = \frac{1}{h^3}\int_V d^3r \int d^3p \;\; e^{-\frac{p^2}{2m_{e,h}k_BT_X}} = V\left(\frac{m_{e,h}k_BT_X}{2\pi\hbar^2}\right)^{3/2} \tag{2.15a}$$

$$Z_X = \frac{1}{h^3}\int_V d^3r \int d^3p \;\; e^{-\frac{p^2}{2m_Xk_BT_X}} \; e^{\frac{Ry^*}{k_BT_X}} = V\left(\frac{m_Xk_BT_X}{2\pi\hbar^2}\right)^{3/2} e^{\frac{Ry^*}{k_BT_X}}. \tag{2.15b}$$

For arbitrary numbers N_e, N_h, and N_X of electrons, holes, and free excitons, the total partition function eq. (2.14) is written in a generalized form

$$Z_{\text{tot}} = \sum_{\{N_e,N_h,N_X\}} \frac{Z_e^{N_e}}{N_e!}\frac{Z_h^{N_h}}{N_h!}\frac{Z_X^{N_X}}{N_X!}. \tag{2.16}$$

[4] The degeneracy factors g_e, g_h, and g_X of the involved photocarrier species (electrons, holes, and free excitons) are not precisely known. Eventually, the individual degeneracy factors account for an additional factor $g^* = (g_eg_h)/g_X$ in the Saha equation (2.17), which only rescales the total photocarrier pair density n_0. Our analysis presented in chapters 5 and 9 will suggest that $g^* \approx 8$.

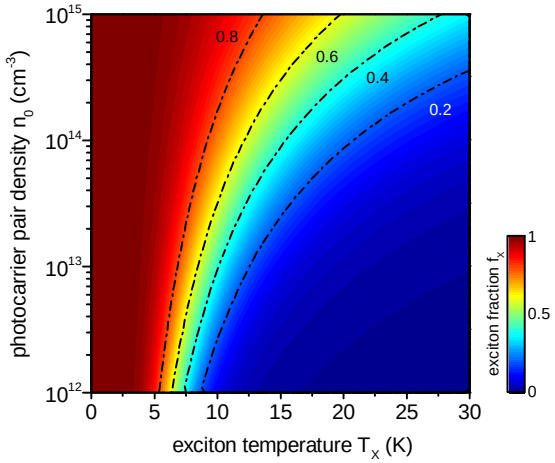

Figure 8: Phase diagram of the partially ionized exciton gas in bulk GaAs described by the Saha equation. Color indicates the relative fraction $f_X = n_X/n_0$ of free excitons among the entire photocarrier population. At elevated temperatures, thermal breakup of Coulomb-bound free excitons into pairs of uncorrelated charge carriers shifts the population balance towards the electron-hole plasma. Interestingly, at fixed temperature, an increase of the total pair density n_0 stabilizes the exciton state and increases the relative exciton fraction in the photocarrier population. Screening effects are neglected.

The sum is performed over all allowed combinations $\{N_e, N_h, N_X\}$ of single particle numbers. Particle conservation demands that if N_X is decreased by one, N_e *and* N_h must be increased by one, i.e., one free exciton is converted into one uncorrelated electron-hole pair.

For a sufficiently large photocarrier population at finite temperatures, the two limiting cases of all charge carriers bound into free excitons or complete ionization of the exciton gas are both very unlikely. The partition function Z_{tot} peaks around a particular configuration $\{N_e, N_h, N_X\}$ associated with the state of largest probability. For a sufficiently large photocarrier population, two successive summands in eq. (2.16) are then approximately equal

$$\frac{Z_e^{N_e}}{N_e!}\frac{Z_h^{N_h}}{N_h!}\frac{Z_X^{N_X}}{N_X!} \approx \frac{Z_e^{N_e+1}}{(N_e+1)!}\frac{Z_h^{N_h+1}}{(N_h+1)!}\frac{Z_X^{N_X-1}}{(N_X-1)!}$$

which leads to the condition

$$\frac{Z_e Z_h}{Z_X} = \frac{(N_e+1)(N_h+1)}{N_X} \xrightarrow{N_e, N_h \gg 1} \frac{N_e N_h}{N_X}.$$

Substituting the one-particle partition functions Z_i [eq. (2.15)] and the electron, hole, and free exciton densities $n_i = N_i/V$, $(i = e, h, X)$, we arrive at the Saha equation for

the partially ionized exciton gas in a bulk semiconductor [10, 78, 79]

$$\frac{n_e n_h}{n_X} = \left(\frac{k_B T_X}{2\pi\hbar^2}\right)^{3/2} \left(\frac{m_e m_h}{m_X}\right)^{3/2} \exp\left(-\frac{Ry^*}{k_B T_X}\right). \tag{2.17}$$

With the substitutions $n_X = f_X n_0$ and $n_e = n_h = (1 - f_X) n_0$, we can compute from the Saha equation (2.17) the relative fraction f_X of free excitons in a photocarrier population of pair density n_0 at a given temperature T_X.

The resulting contour plot $f_X(n_0, T_X)$ is shown in Fig. 8. Two general trends characterize the thermodynamics of the partially ionized exciton gas. Thermal breakup of Coulomb-bound excitons at elevated temperatures T_X shifts the population balance towards the uncorrelated electron-hole plasma. At fixed T_X, however, an increase of the photocarrier pair density n_0 causes a relative increase of the free exciton population. This stabilization of the free exciton state at increased carrier densities continues until screening of the attractive Coulomb interaction leads to a Mott-transition [80] from the partially ionized exciton gas to a fully uncorrelated EHP [10, 81]. Above a critical photocarrier density n_0^{crit}, bound electron-hole pairs are no longer stable and consequently no free excitons exist [43]. For bulk GaAs, the critical Mott density is on the order of $n_0^{crit} \approx 3 \times 10^{16}\,\mathrm{cm}^{-3}$ [82, 83]. This value is beyond the experimentally employed photocarrier densities in this thesis, such that the influence of screening effects on the properties of the partially ionized exciton gas can be neglected.

2.5 Fundamentals of photocarrier heating and cooling

The investigation of hot carrier effects in semiconductors and semiconductor nanostructures has been a dominating topic since the early days of solid state physics [6]. Particularly during the 1960s – 1980s, numerous experimental and theoretical studies were conducted to assess hot carrier distribution functions and to identify the mechanisms of hot carrier excess energy and momentum relaxation. First insights into the physics of hot carrier effects were obtained by high-field transport measurements, from which the processes and rates of various scattering mechanisms were derived [6, 84, 85]. Reviews on transport-related aspects of hot carrier physics can be found in Refs. [84, 86, 87]. Since the late 1960s [6], methods of optical spectroscopy have increasingly been employed to provide, e.g., direct access to the energy distribution functions of hot carrier populations [88] and to gain complementary information to those obtained from transport experiments. Comprehensive reviews on the spectroscopy of hot carrier effects can be found in Refs. [6, 54] and in the authoritative reference work by J. Shah [85].

Hot carrier effects are inherent to all spectroscopic studies involving nonresonant optical excitation at low sample temperatures. Moreover, the quantitative understanding of experimental results obtained under such excitation conditions often requires consideration of pump-induced heating in the carrier system.

The investigation of hot carrier effects is also at the heart of this thesis. Given the wealth of studies reported in the literature and the availability of textbooks and comprehensive review articles on hot carrier effects [6, 54, 85], an in-depth review of the subject is beyond the scope of this thesis. In the present section, we restrict ourselves to recall only the most important fundamentals of photocarrier heating and excess energy relaxation, which are essential for our later interpretation of experimental results. We discuss a representative data set that summarizes the dependence of the photocarrier temperature on various experimental parameters, thereby providing a particularly intuitive understanding of the competition between photocarrier heating and excess energy relaxation.

In contrast to the vast majority of previous studies that have investigated *hot electron* populations, we are in this thesis concerned with the manifestation of *hot exciton effects* [54] in bulk semiconductors. However, the underlying principles of hot photocarrier excitation and excess energy relaxation are conceptually the same for both particle species. The resulting dependence of the electron temperature on experimental parameters, which we review in this section, is hence qualitatively portable to hot exciton populations.

2.5.1 Overview and classification of carrier relaxation regimes

Following the classification by J. Shah [85], a semiconductor that is optically excited by a short laser pulse will run through four stages of carrier relaxation, i.e., the coherent regime, the non-thermal regime, the hot-carrier regime, and the isothermal regime.

The coherent regime At short time delays with respect to an ultrafast laser pulse, the excitation in the semiconductor exhibits a well-defined phase relationship with the electromagnetic field of the laser pulse [85]. Scattering processes that destroy this phase relationship typically occur on the fs or few-ps time scale [89, 90], which necessitates ultrafast optical spectroscopy techniques to probe processes in the coherent regime.[5] The experiments presented in this thesis either utilize continuous-wave optical excitation or the $\gtrsim 500\,\mathrm{ps}$ timing resolution of our time-resolved PL detection scheme (cf. section 3.2.1) is beyond the time scale of coherence effects. For the interpretation of our experimental results, the coherent regime can thus be disregarded from consideration.

The non-thermal regime Nonresonant optical excitation by an ultrashort laser pulse produces free carrier populations in the bands, which exhibit relatively sharp energy distribution functions at $t = 0$ [95]. The situation is schematically depicted in Fig. 9.

[5] The observed effects are often particularly instructive manifestations of basic quantum mechanics [85] and include, but are not limited to, exciton dephasing [89, 90], exciton quantum beats [91], the AC Stark effect on excitonic states [92, 93], and the observation of Bloch oscillations [94].

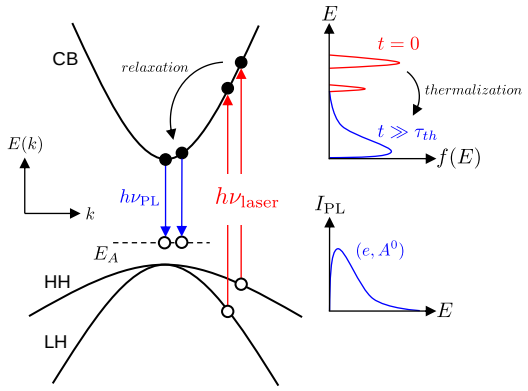

Figure 9: Nonresonant optical excitation produces free carrier populations with relatively sharp energy distribution functions (red), whose widths are determined by the warping of the respective valence band. Efficient electron-electron scattering causes energy redistribution in the photocarrier system until a Boltzmann-distribution function (blue) is established after $\tau_{th} \lesssim 10\,\text{ps}$. The thermalized hot photocarrier ensemble can then be assigned a temperature and subsequently relaxes its excess energy by optical and acoustic phonon emission. In a sample that exhibits shallow acceptor levels, the electron temperature T_e is obtained from a line shape analysis of the electron-to neutral acceptor transition (e,A^0). Note that due to its strong localization in real space, the acceptor state is smeared out in **k** space, such that the line shape of the (e,A^0) PL transition directly reflects the density of occupied states of the electron population in the conduction band.

The carrier populations peak at the excess energies transferred to the respective particle species by the incident photons and, therefore, cannot be described by a temperature [6, 85, 95]. A variety of scattering processes facilitate energy redistribution in the photocarrier system and establish a (thermalized) Boltzmann energy distribution function within a characteristic thermalization time τ_{th}. The photocarrier population can then be assigned a temperature, which most often exceeds that of the crystal lattice. Numerous experiments have been performed to identify the relevant scattering mechanisms and to asses the characteristic time scale of the thermalization process. Experimentally derived thermalization times vary from 10 to 100 fs to the order of 10 ps [75, 96–98]. The large spread of observed thermalization times is most probably due to the carrier density dependence of electron-electron scattering, which is the most efficient thermalization mechanism [85]. The authors of Ref. [75] demonstrate that thermalization following nonresonant optical excitation occurs on a time scale of $\tau_{th} \approx 15\,\text{ps}$ at an excitation density of $4 \times 10^{14}\,\text{cm}^{-3}$ and significantly faster at increased excitation densities. Because of the limited timing resolution of our photoluminescence detection scheme (cf. section 3.2.1), the experiments presented in this thesis are not sensitive to the non-thermal regime. We can, therefore, reasonably

assume thermalized photocarrier and free exciton energy distribution functions at all excitation conditions.

The hot carrier regime After thermalization, the optically excited semiconductor enters the hot carrier regime. The latter is characterized by Boltzmann-distributed charge carrier and exciton populations, whose effective temperature typically exceeds the lattice temperature T_L. Such hot photocarrier ensembles subsequently relax their excess energy by emission of optical and acoustic phonons [99] until the carrier temperature eventually reaches T_L. The experiments presented in this thesis are mainly performed in the hot carrier regime. We hence discuss in the following section the most relevant mechanisms of excess energy relaxation, i.e., optical and acoustic phonon coupling.

The isothermal regime The isothermal regime is eventually reached after all photocarriers have relaxed their excess energy such that photoexcited electrons, holes, and excitons are in thermal equilibrium with the crystal lattice. However, the presence of excess electron-hole pairs distinguishes the isothermal regime from the thermodynamic equilibrium state of the semiconductor, which is only reached after the annihilation of all photoexcited charge carriers and excitons [85].

2.5.2 Excess energy relaxation by phonon coupling

Two competing mechanisms allow for the excess energy relaxation of optically excited electrons, i.e., Coulomb scattering with (cold) background electrons and emission of optical and acoustic phonons. The former process, however, only provides a relaxation channel from the perspective of a single hot electron. Because of energy conservation, electron-electron scattering does not contribute to the excess energy relaxation of the entire photocarrier population. Net cooling of the hot electron ensemble mandates transfer of excess energy to the crystal lattice, which is mediated by the emission of optical and acoustic phonons. We postpone the discussion of Coulomb scattering in the carrier system to a later part of this section and first discuss the different mechanisms of heat dissipation by phonon emission.

The GaAs phonon dispersion relation (Fig. 5) reveals four phonon modes at the Γ point, three of which interact with electrons located at $\mathbf{k} = 0$ [6]. Hot electrons may dissipate heat to the crystal lattice by emission of longitudinal optic (LO), longitudinal acoustic (LA), and transverse acoustic (TA) phonons. Particles with *s*-type symmetry in zinc blende-type semiconductors, however, do not experience coupling to the transverse optic (TO) phonon mode [38].

Optical and acoustic phonons transfer different quanta of excess energy to the lattice, thereby providing varyingly efficient energy-loss channels to the hot electron population. While 36.8 meV [37] of the electron excess energy is imparted to the

crystal lattice by emission of a single LO phonon, the energy transfer by acoustic phonon emission is significantly smaller and typically on the order of $\hbar\Omega \lesssim 3\,\mathrm{meV}$ [6] per scattering event.

Moreover, different electron-phonon interactions are responsible for the emission of optical and acoustic phonons.[6] In addition to the varying scales of energy transfer discussed above, the coupling strengths of the different electron-phonon interactions also influence the cooling efficiency of each energy-loss channel. In a Maxwellian hot electron population of temperature T_e, the average energy-loss rates per electron by piezoelectric (pe), deformation potential (dp), and polar-optic (op) phonon coupling have been given by R. Ulbrich [99] as

$$\left\langle \frac{dE}{dt} \right\rangle_{\mathrm{dp}} = -\left\{ \frac{8\sqrt{2}E_1^2 m_e^{5/2}(k_B T_e)^{3/2}}{\pi^{3/2}\hbar^4 \rho} \right\} \left(\frac{T_e - T_L}{T_e} \right) \tag{2.18a}$$

$$\left\langle \frac{dE}{dt} \right\rangle_{\mathrm{pe}} = -\left\{ \frac{64a\sqrt{\pi}e^2 e_{14}^2 m_e^{3/2}\sqrt{k_B T_e}}{\sqrt{2}\hbar^2 (4\pi\varepsilon_0)^2 \kappa_0^2 \rho} \right\} \left(\frac{T_e - T_L}{T_e} \right) \tag{2.18b}$$

$$\left\langle \frac{dE}{dt} \right\rangle_{\mathrm{op}} = -\left\{ \frac{\sqrt{2m_e}(\hbar\Omega_{\mathrm{LO}})^{3/2} e^2 (\kappa_\infty^{-1} - \kappa_0^{-1})}{4\pi\varepsilon_0 \hbar^2} \right\} \cdots$$
$$\times \left[\exp\left(-\frac{\hbar\Omega_{\mathrm{LO}}}{k_B T_e} \right) - \exp\left(-\frac{\hbar\Omega_{\mathrm{LO}}}{k_B T_L} \right) \right] \tag{2.18c}$$

with $E_1 = 6.3\,\mathrm{eV}$ the deformation potential constant, $\rho = 5.32\,\mathrm{g\,cm^{-3}}$ the mass density of the crystal, $e_{14} = 0.16\,\mathrm{C\,m^{-2}}$ the piezoelectric coupling constant, $a = 0.4$ a dimensionless factor [99], and $\kappa_\infty = 10.9$ and $\kappa_0 = 12.5$ the high- and low-frequency dielectric constants in bulk GaAs [34].[7]

The combined average energy loss rate per electron due to all three phonon coupling mechanisms

$$\left\langle \frac{dE}{dt} \right\rangle_{\mathrm{tot}} = \left\langle \frac{dE}{dt} \right\rangle_{\mathrm{dp}} + \left\langle \frac{dE}{dt} \right\rangle_{\mathrm{pe}} + \left\langle \frac{dE}{dt} \right\rangle_{\mathrm{op}} \tag{2.19}$$

is plotted in Fig. 10 as a function of T_e. The total loss rate $\langle dE/dt \rangle_{\mathrm{tot}}(T_e)$ exhibits a peculiar dependence on the electron temperature T_e (note the semilogarithmic scale). The characteristic $\langle dE/dt \rangle_{\mathrm{tot}}(T_e)$ progression is crucial for an understanding of most photocarrier heating effects.

LO phonon emission is only accessible for electrons with energy $E_e \geq \hbar\Omega_{\mathrm{LO}}$ [6]. At temperatures $T_e \gtrsim 30\,\mathrm{K}$, LO phonon emission by the relatively small number of

[6] In zinc blende-type crystals, which lack a center of inversion symmetry, strain fields associated with LA and TA phonons produce electric fields that give rise to the piezoelectric electron-phonon interaction. The slight shift of the band edge energies induced by the strain fields of LA phonons is the underlying mechanism of the deformation potential electron-phonon coupling. The very efficient electron-LO phonon coupling is mediated by the polar optical Fröhlich interaction [38, 84].

[7] The cooling rates are given in cgs units in Ref. [99], which we converted to SI units in eqs. (2.18).

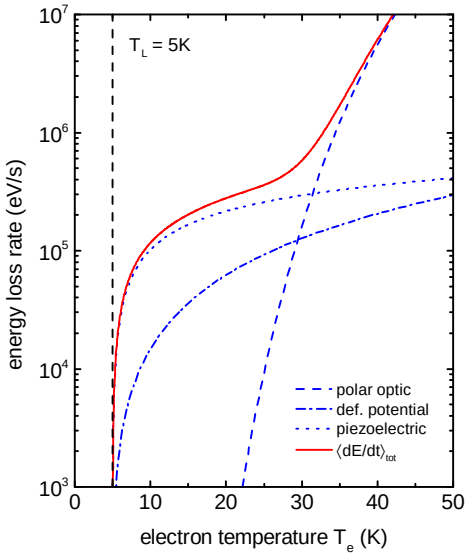

Figure 10: Average energy loss rate per electron as a function of the electron temperature after R. Ulbrich [99]. Polar optic coupling accounts for efficient photocarrier cooling by rapid LO phonon emission at relatively high electron temperatures $T_e > 30\,\mathrm{K}$. Below the "knee" at $T_e \approx 25\,\mathrm{K}$, excess energy relaxation proceeds by the significantly less efficient processes of acoustic phonon emission.

electrons that reside in the high energy tail of the Boltzmann distribution function facilitates already the efficient cooling of the entire photocarrier population. Expectedly, the cooling rate steeply increases at elevated electron temperatures $T_e \gg 30\,\mathrm{K}$ due to the increasing number of relatively energetic electrons for which LO phonon emission is kinematically possible. The polar-optic contribution to the total energy-loss rate, however, collapses at low electron temperatures. The $\langle dE/dt \rangle_{\mathrm{tot}}(T_e)$ curve exhibits a drastic decline for decreasing electron temperatures with a characteristic "knee" at $T_e \approx 25\,\mathrm{K}$. A hot carrier population whose temperature has reached $\approx 25\,\mathrm{K}$ can only relax its excess energy further by the less efficient emission of acoustic phonons.

We emphasize once again that eqs. (2.18) describe the cooling rate of a hot *electron* population and that different rates are certainly expected for holes[8] and free excitons. However, to the best of our knowledge, no previous studies report on the average energy loss rates of free excitons in bulk GaAs.[9] Throughout this thesis, we are mostly

[8] Valence band warping and p-type symmetry of the hole wave functions render the calculation of average energy loss rates more complicated than for the case of electrons [6]. The reduction of the polar-optic coupling strength is countered by the additional availability of nonpolar hole-optical phonon scattering. Ultimately, the average energy loss rates for holes are approximately a factor of 2.5 increased over that for electrons in bulk GaAs [6, 85].

[9] Many works on electron cooling in bulk GaAs utilize a time-resolved photoluminescence study of the free electron-to neutral acceptor transition (e, A^0), from which the temperature of the electron ensemble

not concerned with the exact exciton cooling rates, but rather with the qualitative dependence of the exciton temperature on various experimental parameters. The latter is crucially predetermined by the temperature progression of the average energy loss rates $\langle dE/dt \rangle_{\mathrm{tot}}(T_X)$ and we reasonably expect that the exciton cooling rates are qualitatively comparable to that of free electrons depicted in Fig. 10.

We discuss in the following section a representative data set to familiarize the reader with the typical dependences of the electron temperature on various experimental parameters. The purpose of the discussion is to provide a qualitative and intuitive understanding how the interplay between photocarrier heating and excess energy relaxation governs the carrier temperature in an optically excited semiconductor, i.e., in a typical photoluminescence experiment.

2.5.3 Electron temperature in optically excited semiconductors

The effect of the cooling rates eqs. (2.18) on the transient electron temperature $T_e(t)$ in a time-resolved experiment is rather straightforward. Following a short laser pulse, electrons first relax their excess energy by repeated emission of LO phonons until the residual excess energy falls below $\hbar\Omega_{\mathrm{LO}}$ [99]. This fast cascade emission proceeds simultaneously to the thermalization of the entire photocarrier population. After 100 to 200 ps, the thermalized ensemble reaches a temperature on the order of $T_e \approx 30\,\mathrm{K}$ [100, 101] and cools then further towards the lattice temperature by the less efficient emission of acoustic phonons. The latter regime of the transient cooling typically extends over a time scale of 10 to 100 ns [102].

The situation is more involved under continuous-wave optical excitation. In a standard PL experiment, nonresonant laser excitation acts as a continuous heat source to the photocarrier population. The steady-state electron temperature T_e results from the power balance between this heat source and the combined excess energy-loss rates eqs. (2.18) acting as the heat sink: the excess energy deposited in the electronic system per unit time must equal the amount of excess energy dissipated to the crystal lattice during the same time [88, 99]. Typically, the limited efficiencies of the cooling rates $\langle dE/dt \rangle_{\mathrm{tot}}(T_e)$ at low lattice temperatures cause a significant overheating of the electron population with respect to the crystal lattice.

The power balance between photocarrier heating and cooling, and thereby the stationary electron temperature T_e, is crucially influenced by various experimental parameters, e.g., excitation density, lattice temperature, and excitation wavelength. In the course of this thesis, we will find that certain experimental features exhibit the very same distinctive dependence on excitation density, lattice temperature, and

T_e is obtained (cf. section 2.5.3). Such time-resolved cooling curves $T_e(t)$ allow for a determination of the average energy-loss rates $\langle dE/dt \rangle(T_e)_{\mathrm{tot}}$ [99]. The exciton temperature, however, can only be obtained from the spectral analysis of LO-phonon assisted luminescence transitions [70]. We speculate that one reason for the lack of literature on exciton cooling in bulk GaAs is the inherently weak emission intensity of the free exciton LO-phonon sidebands.

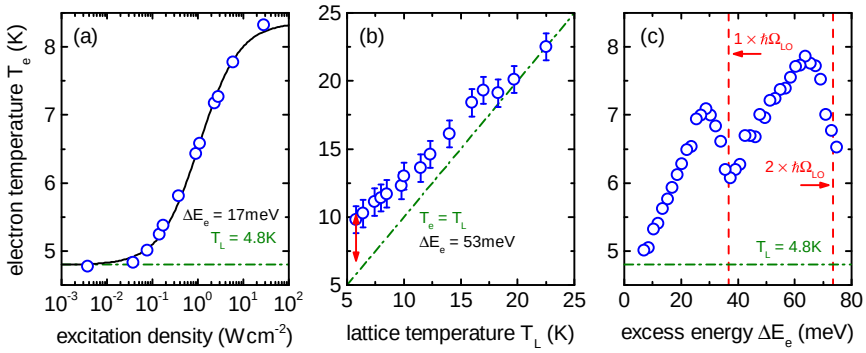

Figure 11: Dependence of the steady-state electron temperature T_e on excitation density, lattice temperature, and electron excess energy. (a) Electrons are in thermal equilibrium with the crystal lattice in the low-excitation limit. Moderate excitation densities already cause a significant heating of the photocarrier population. (b) The pump-induced heating is most pronounced at low lattice temperatures and disappears for $T_L \gtrsim 23\,\mathrm{K}$ [104]. (c) The salient excess energy dependence of the electron temperature indicates efficient dissipation of integral multiples of the $\hbar\Omega_{\mathrm{LO}}$ phonon energy by rapid LO phonon cascade emission.

excitation wavelength. We will conclude from this resemblance that the observed features are related to an overheating of the exciton system caused by nonresonant optical excitation. We, therefore, summarize in Fig. 11 the characteristic dependence of the electron temperature T_e on optical excitation parameters.

All data presented in Fig. 11 are obtained on an unintentionally n-doped bulk GaAs sample (sample A, cf. section 4.1). The steady-state electron temperature T_e is obtained from a line shape analysis of the free electron-to neutral carbon acceptor $(e,A^0)_{\mathrm{C}}$ transition.[10]

Excitation density dependence As shown in Fig. 11 (a), the electron temperature increases monotonically for increasing excitation densities. At the chosen excitation wavelength, each electron is excited with $\Delta E_e \approx 17\,\mathrm{meV}$ excess energy, which is redistributed in the entire electron system by Coulomb scattering. In the low-excitation limit $P_{\mathrm{exc}} < 0.1\,\mathrm{W\,cm^{-2}}$, the number of cold intrinsic electrons significantly exceeds the number of hot photoexcited electrons, such that the thermalized ensemble effectively remains at the lattice temperature T_L. At increased excitation densities, the balance

[10] The (e,A^0) luminescence transition arises from electrons in the conduction band that recombine radiatively with holes localized at neutral acceptor sites (Fig. 9). Because of the energetically discrete final state, the recombination line shape reflects the density of occupied states among the electron population. Neglecting the slight electron **k** vector dependence of the recombination probability and assuming Boltzmann statistics for the electron energy distribution function, the PL line shape of the (e,A^0) transition is given by $I(h\nu) \propto \sqrt{h\nu - E_g + E_A} \times \exp\left[-(h\nu - E_g + E_A)/(k_B T_e)\right]$ with E_A the binding energy of the respective acceptor species [103].

between intrinsic (cold) and photoexcited (hot) electrons is reversed. More excess energy is deposited in the electron system and T_e consistently increases. We note that at least in relatively low-doped samples, moderate excitation densities already cause a significant heating of the photocarrier ensemble. At low sample temperatures, heating effects in the carrier system are virtually unavoidable in all spectroscopic experiments that involve nonresonant optical excitation.

Lattice temperature dependence The lattice temperature dependence of the stationary electron temperature T_e is reported in Fig. 11 (b). The overheating of the nonresonantly excited photocarrier population is most pronounced at low sample temperatures and decreases for increasing T_L. At $T_L \gtrsim 23\,\mathrm{K}$, electrons are in thermal equilibrium with the crystal lattice ($T_e = T_L$).

This lattice temperature dependence of the stationary electron temperature T_e directly reflects the temperature dependence of the average energy loss rates depicted in Fig. 10. At high temperatures $T_e \gtrsim 30\,\mathrm{K}$, LO phonon emission is kinematically possible for electrons that reside in the high-energy tail of the Boltzmann energy distribution function. The large energy transfer per scattering event enables efficient cooling of the entire electron population. The $\langle dE/dt \rangle (T_e)$ characteristic, however, exhibits a steep decline for decreasing temperatures. Below the "knee" at $T_e \approx 25\,\mathrm{K}$, the collapse of the cooling rate due to the limited efficiency of piezoelectric and deformation potential scattering causes the observed pronounced overheating at low sample temperatures.

Excess energy dependence The steady-state electron temperature T_e exhibits a distinct dependence on excitation excess energy, which can be controlled by variation of the laser excitation wavelength λ_{exc}. Because of the different curvature of the conduction and valence bands (i.e., different effective masses of free electrons and holes) the entire excess energy of the incident photon is asymmetrically shared between the photoexcited electrons and holes. The amount of excess energy ΔE_e imparted to the electron is given by [105]

$$\Delta E_e = (E_{\mathrm{Ph}} - E_g) \times \left(1 + \frac{m_e}{m_{hh}}\right)^{-1} \tag{2.20}$$

with $E_{\mathrm{Ph}} = hc/\lambda_{\mathrm{exc}}$ the photon energy, E_g the band gap energy, and m_e, m_{hh} the electron and heavy hole effective masses. In GaAs, $m_{hh} \gg m_e$, such that the greater part of the total excess energy $E_{\mathrm{Ph}} - E_g$ is transferred to the electron. Noteworthy, monochromatic laser excitation does not allow for the optical excitation of electrons at perfectly well-defined excess energies. This is because valence band warping accounts for a broadening of the initial electron energy distribution function (cf. Fig. 2) whose "width" is typically on the order of 10 % of the average excess energy ΔE_e [6].

The characteristic excess energy dependence $T_e(\Delta E_e)$ is depicted in Fig. 11 (c). At increased photon energies, more excess energy is deposited in the carrier system. However, the rate of excess energy dissipation (the cooling efficiency) *per electron* remains unchanged. For moderate excess energies $\Delta E_e \lesssim 30\,\mathrm{meV}$, a monotonic increase of the stationary electron temperature T_e as a function of increasing ΔE_e is expectedly observed in the experiment. A deviation from this trend occurs when the electron excess energy coincides with integral multiples of the LO phonon energy $\hbar\Omega_{\mathrm{LO}} = 36.8\,\mathrm{meV}$. The pronounced dips in the $T_e(\Delta E_e)$ progression demonstrate very intuitively the efficient relaxation of multiples of $\hbar\Omega_{\mathrm{LO}}$ excess energy to the crystal lattice by rapid LO phonon emission. The "width" of the valley at 36.8 meV excess energy is due to the valence band warping (cf. section 2.1), which washes out the initial electron energy distribution function in the conduction band.

The non-monotonous (oscillatory) excess energy dependence of the electron temperature is the most characteristic fingerprint of heating effects in the photocarrier system [105]. However, the LO phonon dips in the the $T_e(\Delta E_e)$ progression are less pronounced at high excitation densities [106–108], which is understood by considering electron-electron scattering as a competing mechanism to the fast initial LO phonon cascade emission.

At high excitation densities, Coulomb scattering [89] mediates redistribution of the excitation excess energy ΔE_e in the entire carrier population even before LO phonon emission occurs. The efficiency of Coulomb scattering is a strong function of the electron density and, therefore, possibly bypasses the LO phonon emission at high excitation densities. At low excitation densities, the LO phonon cascade completes before the remaining excess energy is redistributed in the electron system. One observes then the characteristic oscillatory $T_e(\Delta E_e)$ dependence shown in Fig. 11 (c).

Chapter 3

Optical instrumentation

All experiments presented in this thesis are carried out on a low-temperature time and spatially resolved micro-photoluminescence (μ-PL) setup. A schematic drawing of the setup is shown in Fig. 12. We briefly discuss in the present chapter the components of the μ-PL setup and the working principle of the time and spatially resolved PL detection schemes.

The sample is mounted on the coldfinger of a liquid helium flow optical cryostat (model Cryovac Konti-Cryostat-Mikro), which allows variation of the sample temperature between 5 K and room temperature. Apiezon N Grease is used to provide good thermal contact between the sample and the cryostat coldfinger. The cryostat is mounted on a x-y translation stage equipped with micrometer screws for lateral fine positioning of the excitation laser spot on the sample surface.

Tunable optical excitation is provided by a continuous-wave (cw) Ti:Sapphire laser (model Coherent MBR-110) pumped at 532 nm by a frequency-doubled Nd:YVO_4 solid state laser (model Coherent Verdi V10). The laser module is located in the neighboring laboratory and the excitation laser light is routed to our μ-PL setup by single mode optical fibers. We use a standard prism-monochromator (plasma line filter) to suppress stray light resulting from the broadband fluorescence of the Ti:Sapphire crystal. Spectral filtering of the excitation laser beam proves to be crucial for our experiments. The inherently weak emission intensity of the free exciton second LO-phonon replica is otherwise masked by laser stray light, which renders a spectral line shape analysis of that transition unfeasible.

The cryostat and all optical components are mounted on an optical table equipped with an active vibration isolation system to maintain stable focusing conditions during the experiments.

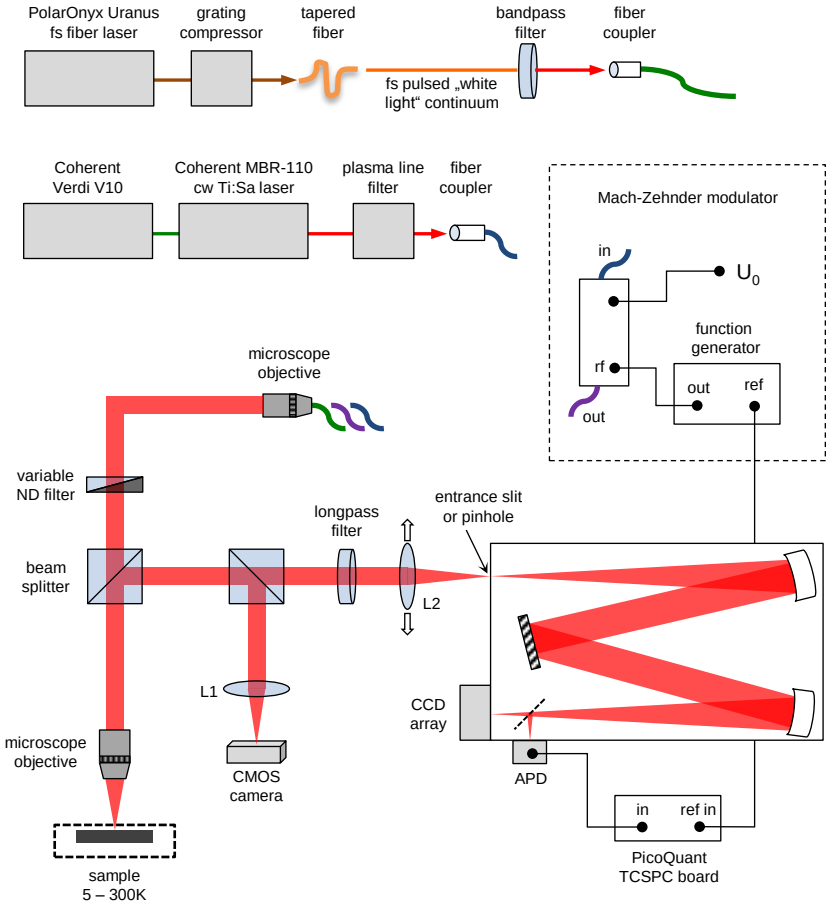

Figure 12: Schematic of the time and spatially resolved μ-PL setup. Optical excitation is provided by either a tunable continuous-wave (cw) Ti:Sapphire laser or a pulsed "white light" supercontinuum fiber-laser source. Both laser systems are located in the neighboring laboratory. Laser light is routed to the μ-PL setup by single mode optical fibers. Box-shaped excitation pulses are generated from the cw Ti:Sapphire laser by a fiber-coupled Mach-Zehnder modulator, which is driven by a function generator. The excitation laser spot is focused on the sample surface, a magnified image of which is projected in the monochromator entrance slit plane. Spatially resolved PL images are detected by a LN_2-cooled CCD array. Photoluminescence transients are detected by the time-correlated single photon counting technique.

3.1 Spatially resolved PL imaging

We use a confocal measurement geometry to realize a spatially resolved detection scheme. After exiting the optical fiber, the laser beam is collimated by a standard microscope objective. The laser light is passed through a pellicle beam splitter and coupled into an infinity-corrected apochromatic Mitutoyo microscope objective (focal length 10 mm, 0.4 numerical aperture). The laser beam is focused at normal incidence on the sample surface. Lens L1 projects a 20× magnified image of the sample surface on the sensor of a CMOS camera (model Thorlabs DCC1545M). The 3.6 µm ($1/e$) full width of the Gaussian excitation spot is determined from the magnified image of the laser spot reflected from the sample surface [Fig. 13 (d)].

Luminescence is collected by the focusing objective and directed towards a 1 m focal length monochromator (model Jobin Yvon HR1000) equipped with a 1200 mm^{-1} grating. A suitable dielectric long pass filter separates the luminescence from the excitation laser light.

Spatially resolved photoluminescence (SRPL) images are obtained by the following routine. Lens L2 (focal length 150 mm) projects a 15× magnified image of the sample surface in the plane of the monochromator entrance slit. The width of the vertical entrance slit assembly is reduced and lens L2 is adjusted such that luminescence is only collected from a region of the sample surface indicated in Fig. 13 (d) by the blue lines. When operated in zeroth diffraction order, the monochromator projects an image of the entrance slit on the sensor of a liquid-nitrogen-cooled CCD array (model Princeton Instruments LN/CCD-1100PF). In first diffraction order, the grating disperses the luminescence in horizontal direction, but leaves the vertical coordinate unaffected. The CCD array then detects a spatially resolved PL image: wavelength information is contained in the horizontal pixel number, spatial information is contained in the vertical pixel number. Wavelength calibration is carried out by the emission lines from a PEN-RAY krypton gas lamp. Spatial information is reconstructed from the 15× magnification ratio and the 24 µm pixel size of the CCD detector.

For the sake of illustration, we present in Fig. 13 (a) a representative raw data set obtained on a high purity GaAs sample (sample A, cf. section 4.1) by the described SRPL detection scheme. The position of the monochromator grating is chosen such that the SRPL image captures the excitonic region of the GaAs emission spectrum. Color indicates the emitted PL intensity. The spatial extent of the excitation laser spot is indicated for reference by the red profile. Horizontal line cuts through the 2D data set [indicated by the dashed line in Fig. 13 (c)] yield PL spectra at a given position, i.e., at a fixed distance from the excitation spot. Vertical line cuts [dash-dotted line in Fig. 13 (b)] yield spatial PL profiles at a fixed excitation wavelength, i.e., on a specific PL transition in the spectrum. Apparently, luminescence is detected at large distances from the excitation spot. This indicates that excitons, which are only created at the excitation center, diffuse several 10 µm before recombining radiatively. In part III of

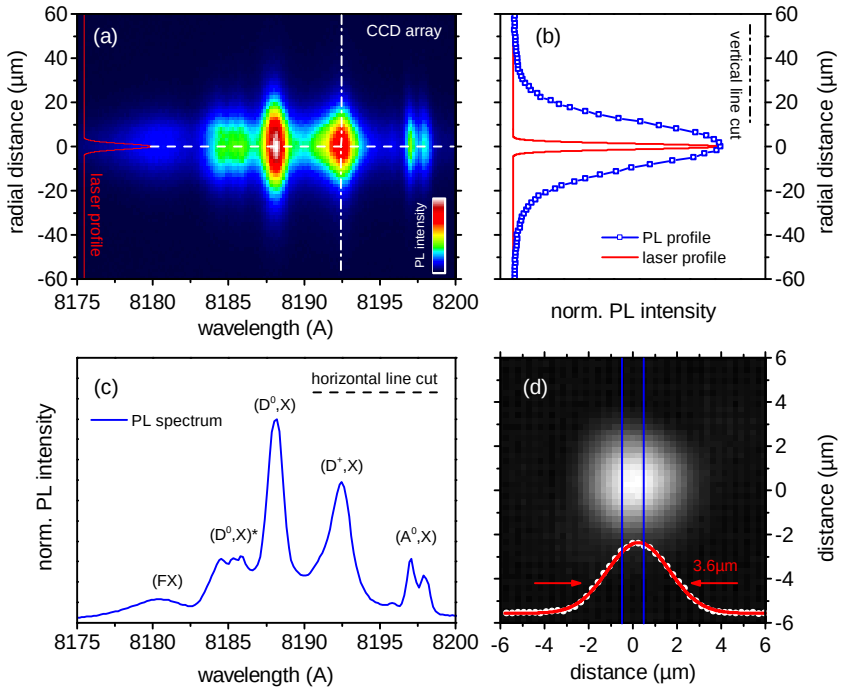

Figure 13: (a) Representative SRPL raw data set detected by the CCD array. Luminescence is dispersed in horizontal direction, spatial information is contained in the vertical pixel number of the 2D image. Note that PL is detected at large distances from the excitation spot (red profile), indicating significant photocarrier diffusion before radiative recombination takes place. (b) Vertical line cuts yield spatial PL profiles at a given detection wavelength. (c) Horizontal line cuts through the 2D data set yield PL spectra at a fixed distance from the excitation spot. Assignment of the free and bound exciton PL transitions is discussed in chapter 4. (d) A magnified image of the laser spot reflected from the sample surface is projected on a CMOS camera chip to monitor the excitation conditions. The $(1/e)$ full width of the laser spot is 3.6 µm. Blue lines indicate the PL detection area in a typical SRPL experiment.

this thesis, we will analyze such SRPL images to study the diffusion of free excitons and to investigate the free and bound exciton ring formation in high-purity GaAs.

3.2 Time-resolved PL detection

We use the time-correlated single photon counting (TCSPC) technique to record time-resolved photoluminescence (TRPL) signals. Depending on the purpose of our measurements, we employ two different excitation schemes. The first one uses sub-ps laser pulses for ultrafast optical excitation. The second one uses step-like laser excitation (≈ 100 ns excitation pulse length) to investigate the decay of a photocarrier population from a stationary initial state.

3.2.1 Ultrafast optical excitation

This measurement scheme is the "standard" TCSPC setup [109], which is used for virtually all TRPL studies by the TCSPC technique reported in the literature. Optical excitation is typically provided by a laser system that generates ultrashort laser pulses on the ps time scale. In our experiments, we use the output of an ultrafast "white light" supercontinuum fiber-laser source, which generates sub-ps excitation pulses at a repetition rate of 36.5 MHz (27 ns pulse-to-pulse interval). A (750 ± 40) nm dielectric bandpass filter selects a suitable spectral slice from the 400 to 1600 nm output continuum for above-bandgap optical excitation. The reader may consult Ref. [110] and references therein for details on the working principle of the "white light" laser source.

Every δ-like laser pulse excites a certain photocarrier population, which then decays radiatively. In a typical experimental situation, all photoexcited electron-hole pairs have decayed before the arrival of the next laser pulse. The procedure of photocarrier creation and annihilation repeats then at the frequency of the laser pulse train.

A single photon counting module (model PicoQuant TimeHarp 200) is used to acquire time-resolved PL signals. The timing reference is set by a fast photo diode, which translates the pulse train of the "white light" laser into a series of voltage pulses. Luminescence photons are detected by an avalanche photo diode (APD), which generates voltage pulses upon the arrival of single photons. The APD output is passed to the single photon counting board, which measures the time delay Δt between arrival of the luminescence photon and the respective laser pulse. This measurement is repeatedly carried out until a full histogram of photon detection events as a function of Δt reports the time-resolved decay process of the photocarrier population.

The sub-ps temporal width of our laser pulses is orders of magnitude smaller than the timing resolution of the TCSPC hardware. We exploit this circumstance to characterize the timing resolution of our setup by the following procedure. The monochromator is tuned to the laser excitation wavelength such that the APD directly detects the appropriately attenuated laser pulse train. From the temporal broadening of the δ-like excitation pulses [Fig. 14 (a)], we estimate the overall timing resolution of our TCSPC setup of ≈ 500 ps. The asymmetrically broadened shape of the excitation laser pulse is referred to as the instrument response function (IRF). The finite width of the IRF has to be considered in any later data analysis routine. A typical procedure is to assume a model function that describes the PL response of the sample to a δ-like excitation pulse. The convolution of this model function with the IRF is then adjusted for best agreement with experiment. Decay times that are directly obtained from TCSPC raw data disregard the broadening effect of the IRF finite width and potentially overestimate the actual photocarrier decay times.

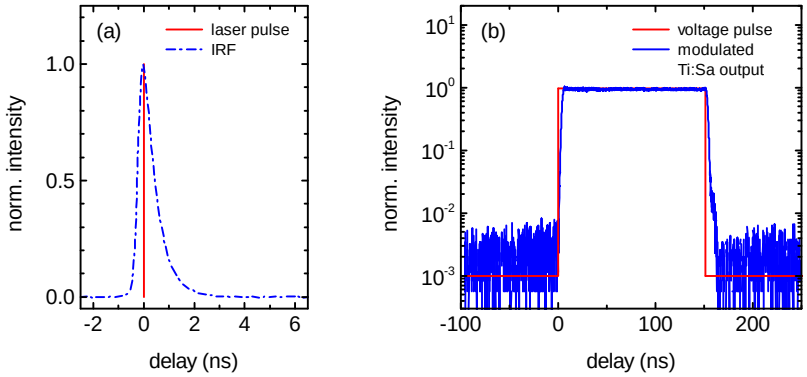

Figure 14: (a) The temporal broadening of a δ-like laser pulse recorded by the TCSPC detection scheme determines the overall timing resolution of the setup. (b) A fiber-coupled Mach Zehnder modulator allows for the step-like modulation of a cw laser source. Such box-shaped laser pulses of tunable excitation wavelength are crucial for our experiments presented in chapter 6.

3.2.2 Long excitation pulses

The luminescence kinetics of the photocarrier population following ultrafast optical excitation results from the convoluted interplay of exciton formation, thermalization, excess energy relaxation, radiative, and non-radiative decay processes. We will discuss these processes and their mutual interconnection in chapter 6. We note, however, that a specific subset of these processes can be addressed individually by proper choice of the excitation pulse shape. In chapter 6, we investigate the free exciton PL response in GaAs sample to box-shaped excitation pulses of $\approx 100\,\mathrm{ns}$ duration. We discuss the rationale behind this particular choice of excitation conditions in chapter 6 and describe here only the generation of the desired step-like laser pulses.

The spectrally filtered and linearly polarized output of the cw Ti:Sapphire laser is coupled into a polarization-maintaining single mode optical fiber. The end of this fiber is attached to a fiber-coupled Mach-Zehnder modulator (model Jenoptik AM830b), the working principle of which is schematically depicted in Fig. 15. The incoming laser light is split into two components of equal optical power and guided in two parallel $LiNbO_3$ waveguide channels. Coplanar electrodes enable the application of in-plane electric fields in both channels. By the electro-optic effect, an external electric field changes the refractive index of the ferroelectric active medium $LiNbO_3$ and introduces a phase difference between the guided light in both branches. Proper tuning of the phase shift by variation of the electric field strength leads to destructive interference at the output of the modulator [111].

The optical output power vs. modulation voltage characteristic is depicted in Fig. 15. A step-like modulation voltage, the high (low) levels of which are chosen to

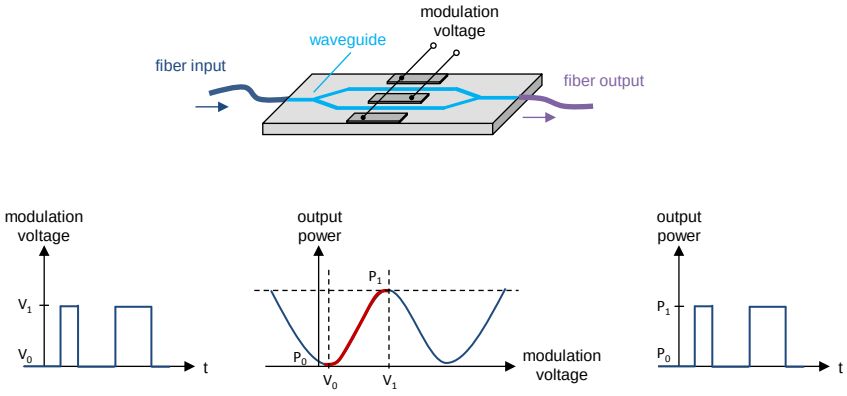

Figure 15: Schematic of the fiber-coupled Mach-Zehnder modulator. Incoming laser light is split and guided in two parallel ferroelectric waveguide channels. Application of an electric field changes the transmission state of the modulator. Proper choice of the modulation voltage levels allows for the generation of laser pulses that exhibit arbitrary frequency and duty cycle. Adapted from [111].

meet the maximum (minimum) transmission state of the modulator device, causes a step-like modulation of a cw laser input. In our setup (cf. dashed box in Fig. 12), the modulator is driven by a function generator (model HP 3314A) at the desired frequency and duty cycle. The low level of the modulation voltage is set by a standard laboratory voltage supply.

We show in Fig. 14 (b) a typical box-shaped excitation pulse obtained from our amplitude modulator assembly. The modulation voltage pulse is plotted as a reference. The extinction ratio between the on and off state of the modulated laser pulse is on the order of 1 : 1000. The modulator introduces a slight distortion of the rectangular voltage pulse shape with a 90 to 10 % edge steepness of ≈ 2.5 ns. The amplitude modulator is particularly useful in combination with a tunable cw Ti:Sapphire laser, which provides access to custom-shaped excitation pulses of variable excitation wavelength.

3.3 Time and spatially resolved detection scheme

We utilize the following detection scheme to trace luminescence signals with simultaneous temporal and spatial resolution. As for the SRPL setup described in section 3.1, the excitation laser is focused to a Gaussian spot of 3.6 µm $(1/e)$ full width on the sample surface. For time *and* spatially resolved μ-PL measurements, we use the spectrally sliced output of the pulsed "white light" laser source described in section 3.2.1. Here, too, luminescence is collected in a confocal geometry by the focusing objective and lens L2 projects a 15× magnified image of the sample surface in the monochromator

entrance slit plane.

For the detection scheme described here, the vertical entrance slit assembly is replaced by a 50 µm diameter pinhole (Fig. 12). The pinhole, which is positioned in the L2 image plane, selects luminescence from a well-defined position on the sample surface and blocks PL that was emitted from any other region of the sample. Lens L2 is mounted on a three-axis translation stage, the x-µm drive of which is moved by a stepper motor. Scanning the entire PL image across the fixed pinhole allows to map out the spatially resolved PL distribution on the sample surface. The spatially selected luminescence is then dispersed in the monochromator and detected by the APD. The TCSPC technique is used to record the time evolution of the PL signal at a given spatial coordinate.

Repeating this time-resolved data acquisition at every position of a two-dimensional SRPL map yields a three-dimensional data set that contains full information on the time and spatially resolved PL response of the sample. We can extract from this data set a series of momentary PL images as a function of time delay with respect to the laser pulse to visualize the time-resolved photocarrier diffusion process in real space.

In a typical experimental situation, the SRPL images are radially symmetric with respect to the excitation spot. Full information on the isotropic diffusion process is then contained in a time-resolved series of centrical line scans through the momentary SRPL images.

Chapter 4

Sample characterization

All experiments reported in this thesis are conducted on one of two high-purity GaAs samples. We briefly summarize in this chapter the available basic information on both sample structures and discuss the assignment of the recombination lines in the low-temperature PL spectra.

4.1 Sample A

Sample A is a 70 µm thick layer of (001)-oriented, unintentionally *n*-doped liquid phase epitaxy (LPE) grown GaAs, which exhibits a residual impurity concentration on the order of 1×10^{13} to $1 \times 10^{14}\,\mathrm{cm}^{-3}$. The excellent GaAs sample was provided by E. Bauser, Max-Planck-Institut für Festkörperforschung, Stuttgart.[11]

The excitonic and impurity-related regions of the PL spectrum under weak optical excitation are shown in Fig. 16. The well-defined excitonic PL spectrum attests to the exceptional crystalline quality of the investigated sample. Text labels indicate the usual assignment of excitonic and impurity-related transitions [34].

Free exciton line (FX) denotes the radiative recombination of free excitons. The asymmetric doublet is a consequence of the polariton effect in a thick GaAs layer and indicates the presence of residual neutral donor impurities in the sample [58, 59].

Bound exciton lines The transitions labeled (D^0,X) and (A^0,X) are due to the recombination of excitons localized at shallow neutral donors and acceptors, respectively.

[11] LPE samples grown by E. Bauser (1934-1996) are widely appreciated as high quality GaAs samples that typically reveal sharp PL transitions and exceptionally high mobilities [112]. Although we are not concerned with "traditional" transport experiments throughout this thesis, high mobilities (and hence large exciton diffusion lengths) are a prerequisite for the manifestation of the free and bound exciton ring formation effects, which we discuss in chapters 8 and 9.

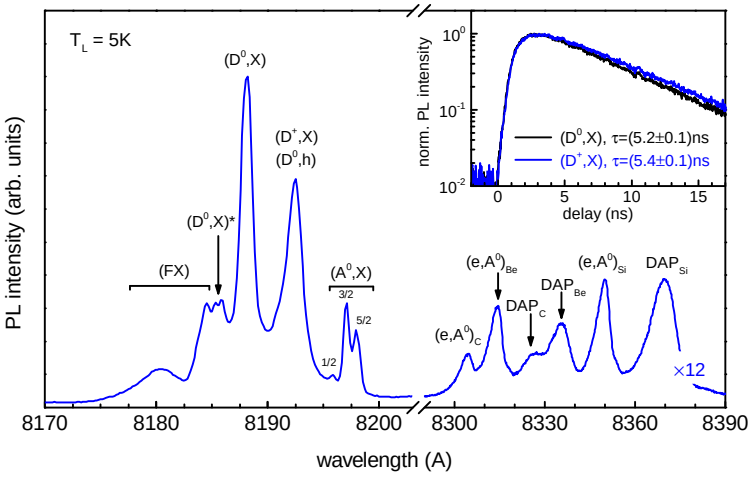

Figure 16: Photoluminescence spectrum of sample A under defocused weak optical excitation. Text labels indicate excitonic and free-to-bound transitions in the usual nomenclature [34]. The sharp exciton lines and the comparatively weak emission intensity of the impurity transitions attest the high quality of the sample. TRPL traces detected on the (D^0,X) transition and the 8192 Å line are reported in the inset. The nearly identical decay times indicate that the 8192 Å line is of predominantly excitonic, i.e., (D^+,X) origin. Our results presented in chapter 8 will independently corroborate this assignment.

The fine structure splitting of the (A^0,X) transition results from jj-coupling between the exciton and the residual hole on the neutral acceptor site [113]. The series of transitions denoted as $(D^0,X)^*$ is ascribed to excited states of the donor bound exciton [114].

Unambiguous assignment of the 8192 Å line mandates additional characterization since the recombination line of excitons localized at ionized donor sites (D^+,X) and the neutral donor-hole transition (D^0,h) occur at the same energetic position in the spectrum [115].

To elucidate the origin of the respective PL line, we perform time-resolved photoluminescence (TRPL) measurements on different transitions in the spectrum. The results are reported in the inset of Fig. 16. We observe nearly identical decay times of (5.2 ± 0.1) ns on the (D^0,X) transition and (5.4 ± 0.1) ns on the 8192 Å line. These decay times are typical for excitonic transitions [51, 52]. We conclude that the 8192 Å line is of predominantly excitonic, i.e., (D^+,X) origin. Our analysis of the spatially resolved PL profiles, which we discuss in the course of chapter 8, will independently corroborate the (D^+,X) assignment.

Free-to-bound transitions The spectral positions of the electron-to neutral acceptor transitions (e,A^0) and the related donor-acceptor pair transitions (D^0,A^0) reveal carbon, beryllium, and silicon as the predominant residual acceptor species in active

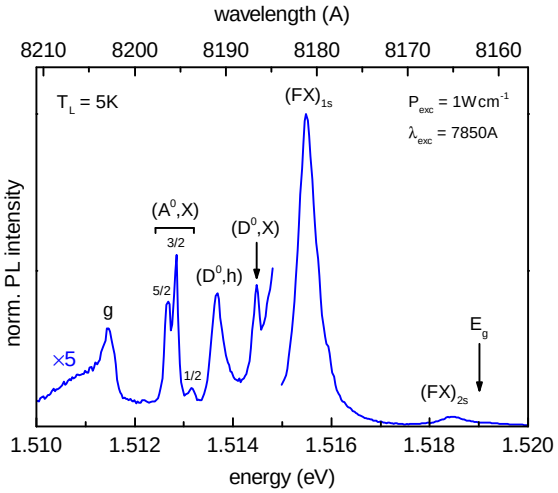

Figure 17: Low-temperature PL spectrum of sample B under homogeneous weak excitation. The spectrum is dominated by the free exciton recombination line (FX), which indicates the exceptionally low residual impurity concentration in the active GaAs layer. Appearance of the 2s exciton transition corroborates the high quality of the sample. Text labels indicate the usual nomenclature of free and bound exciton transitions [34].

GaAs layer [34]. The weak emission intensity of the impurity-related recombination lines compared with the strong excitonic PL transitions corroborates the low residual impurity concentration in the sample.

4.2 Sample B

Except for the data presented in Fig. 11 and chapter 8, all measurements presented in this thesis are performed on sample B. This sample is a nominally undoped 1.5 µm thick epilayer of (001)-oriented molecular beam epitaxy (MBE) grown GaAs. The active layer is sandwiched between one 250 periods GaAs/$Al_{0.09}Ga_{0.91}As$ superlattice below and one 80 periods superlattice of equal composition on top to prevent optically excited excitons from diffusing out of the layer and to suppress surface recombination [116]. The sample was grown at Philips Research Laboratories, Redhill, UK by J. J. Harris and C. T. Foxon and is another piece of the same wafer that was previously investigated in Ref. [52].

Assignment of excitonic PL transitions The excitonic region of the low-temperature PL spectrum is displayed in Fig. 17. The spectrum is dominated by the free exciton recombination line (FX), which indicates the exceptional purity of the sample. From a comparison with spectra reported in the literature [73, 114], we estimate a residual impurity concentration of $\lesssim 1 \times 10^{12}\,\mathrm{cm}^{-3}$ in the active GaAs layer. Appearance of

both the 1s and 2s free exciton recombination lines [52] further attests to the high quality of the sample.

Because of the exceptionally low residual impurity density, we detect only weak bound exciton luminescence. The group of three peaks centered at 1.5129 eV is assigned to shallow acceptor-bound excitons. The $\{1/2, 3/2, 5/2\}$ fine structure splitting of the (A^0, X) line results from jj-coupling between the exciton and the residual hole on the neutral acceptor site [113]. From the spectral position of the free electron-to neutral acceptor transition (e, A^0) (not shown in Fig. 17), we identify carbon as the predominant residual acceptor species in the active GaAs layer.

The transition labeled (D^0, X) results from excitons localized at shallow donors and the emission line at 1.5137 eV is assigned to the free hole-to-neutral donor transition (D^0, h).[12] The so-called g line [52] belongs to a series of PL lines attributed to excitons localized at structural defects of the crystal lattice [117, 118].

Excitation density dependence of the free exciton linewidth The excitation density dependence of the excitonic PL spectrum is shown in Fig. 18 (a). We observe a monotonous broadening of the free exciton line [119], which is caused by efficient exciton-exciton and exciton-free carrier scattering at increased excitation densities. L. Schultheis et al. have investigated the mechanisms of exciton line broadening in bulk GaAs by the time-resolved degenerate four-wave mixing technique [60, 89]. This method provides experimental access to the excitonic phase coherence time T_2, which is related to the homogeneous free exciton linewidth as $\Gamma \propto 1/T_2$. By selectively exciting background populations of free excitons and unbound electron-hole pairs, the authors find that scattering of excitons with free carriers is ≈ 10 times more efficient than exciton-exciton scattering. In the low-excitation limit, the phase coherence time saturates. The T_2 time (and hence the exciton linewidth) is then only limited by scattering with acoustic phonons.

The qualitative dependence of the full-width at half maximum (FWHM) of the (FX) line, which is plotted in Fig. 18 (b) as a function of the excitation density, is in good agreement with the results obtained by L. Schultheis et al. [60, 89]. In the low-excitation limit $P_{\mathrm{exc}} < 0.1\,\mathrm{W\,cm^{-2}}$, the linewidth is only determined by scattering with acoustic phonons and, therefore, does not depend on the excitation density. At increased P_{exc}, the linewidth increases monotonically by efficient exciton-free carrier scattering [see also Fig. 26 (c)].

Temperature dependence of the excitonic PL spectrum We show in Fig. 18 (c) the excitonic PL spectrum as a function of the sample temperature T_L. The evolution

[12] If present, the PL transition of excitons localized at ionized donor sites (D^+, X) is expected at the same detection energy as the (D^0, h) transition [115]. We favor here the (D^0, h) assignment because of the asymmetric line shape of the transition, which exhibits a pronounced tail on the high-energy flank. This is expected for a free-to-bound PL transition, but not for a bound exciton recombination line.

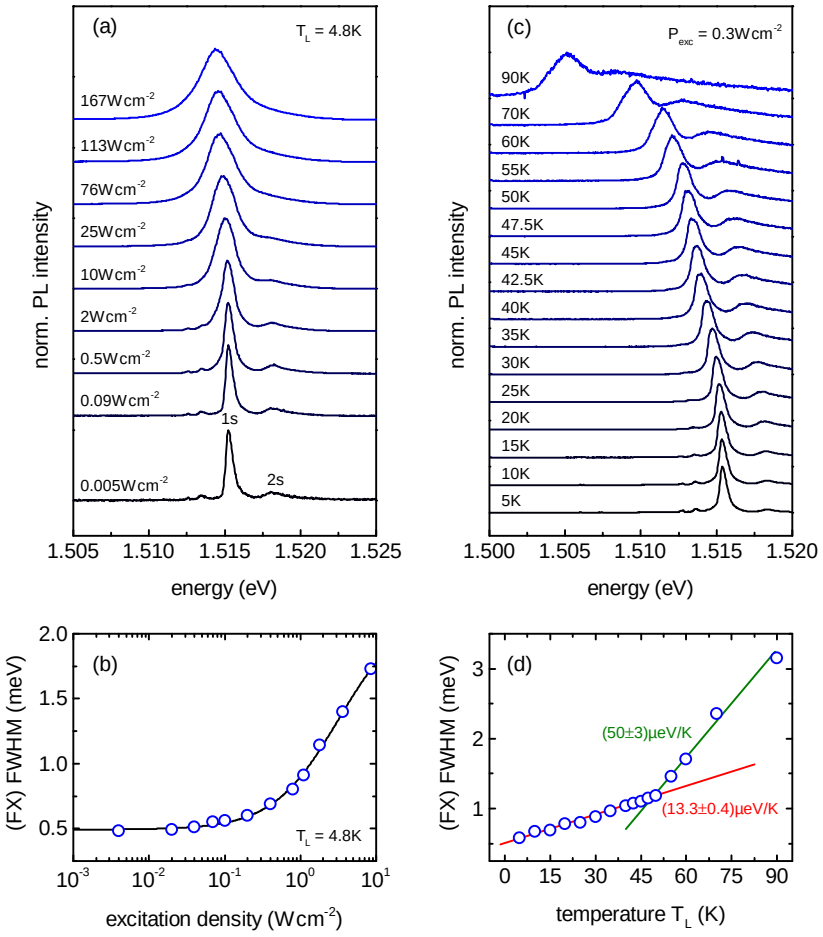

Figure 18: (a) The width of free exciton zero-phonon line (FX) increases for increasing excitation densities. The slight shift towards smaller detection energies potentially indicates spurious lattice heating at high pump powers. We note, however, that such lattice heating would not interfere with our later interpretation of the free exciton TRPL traces discussed in chapters 5 and 6. (b) The linewidth in the low-excitation limit is caused by acoustic phonon scattering and allows to estimate the phase relaxation time T_2. (c) The shift of the (FX) line at increased sample temperatures monitors the narrowing of the fundamental band gap. Note that free exciton luminescence is detected at lattice temperatures $k_B T_L \geq 4.2\,\mathrm{meV}$, which is naturally explained by the Saha equation. (d) The broadening of the (FX) line at elevated sample temperatures is due to the increased phonon scattering rates.

of the spectrum is characterized by three general trends.

1. Upon increasing T_L, the (FX) transition shifts to smaller detection energies. This redshift is induced by the narrowing of the fundamental semiconductor band gap at elevated lattice temperatures [120, 121].

2. The width of the (FX) line increases for increasing lattice temperatures. This temperature broadening is closely related to the broadening of the free exciton line at increased excitation densities. As discussed above, the free exciton phase coherence time T_2 reduces by scattering with other excitons, individual charge carriers, and phonons. In the low-excitation limit at low sample temperatures [cf. Fig. 18 (b)], acoustic phonon scattering limits the T_2 time and hence governs the (FX) linewidth. For $5\,\mathrm{K} < T_L < 50\,\mathrm{K}$, the (FX) linewidth increases at a rate of $(13.3 \pm 0.4)\,\mu\mathrm{eV\,K^{-1}}$. This value is in good agreement with the $17\,\mu\mathrm{eV\,K^{-1}}$ line broadening reported in Ref. [90], which was also assigned to scattering with acoustic phonons. For $T_L \geq 50\,\mathrm{K}$, the width of the free exciton line increases more rapidly at a rate of $(50 \pm 3)\,\mu\mathrm{eV\,K^{-1}}$. We speculate that the enhanced broadening is caused by scattering with LO phonons, which are only populated at elevated lattice temperatures.

3. At increased lattice temperatures, the PL intensity of direct band-to-band transitions increases while the intensity of the (FX) line progressively reduces. This trend is due to the thermal breakup of free excitons into unbound electron-hole pairs. However, free exciton luminescence is still detected at relatively high lattice temperatures $T_L \gg 48\,\mathrm{K}$, for which $k_B T_L$ significantly exceeds the free exciton binding energy of 4.2 meV. This observation might appear counterintuitive at first sight. Recent works have, therefore, proposed an alternative assignment of the (FX) PL line.

   Instead of being caused by the radiative recombination of free excitons, A. Amo et al. [83] interpret the (FX) line as a signature of the Coulomb-correlated electron-hole plasma (EHP), which was recently proposed by M. Kira et al. [11, 12]. The Coulomb-correlated EHP is predicted to account for a PL line at the spectral position of the 1s (FX) resonance. Noteworthy, this anticipated PL transition obviates the existence of free excitons in the crystal.

   We, however, strongly favor the "traditional" assignment of the (FX) line. This is because the Saha ionization equilibrium (Fig. 8) predicts the existence of free excitons even at relatively high sample temperatures $T_L \gg 48\,\mathrm{K}$. The relative fraction of free excitons in the entire photocarrier population is then certainly small. However, free exciton radiative decay is significantly more efficient than the bimolecular recombination of the EHP [83, 122], such that free exciton luminescence dominates the PL spectrum even at $T_L = 90\,\mathrm{K}$. The less frequently

considered Saha equation hence provides a very natural explanation for the presence of free exciton luminescence at elevated sample temperatures and puts the recent interpretation of the (FX) line as a signature of the Coulomb-correlated EHP [83] into question.

In summary, sample B is a high quality GaAs epilayer that exhibits a negligible residual impurity concentration, providing an ideal model system for the investigation of the undisturbed luminescence kinetics of free excitons in bulk semiconductors. As we discuss in chapter 7, the effectively two-dimensional sample geometry with the relatively thin active layer sandwiched between two GaAs/$Al_{0.09}Ga_{0.91}$As superlattices also renders sample B the ideal testbed system for the investigation of the intrinsic free exciton diffusion process.

Part II

Kinetics of free exciton luminescence in high-purity GaAs

Chapter 5

Free exciton photoluminescence rise — transient thermodynamic equilibrium between excitons and the uncorrelated electron-hole plasma

Time-resolved photoluminescence (TRPL) spectroscopy is widely used to investigate the time evolution of photoexcited exciton populations in semiconductors and semiconductor nanostructures [85]. Most commonly, ultrafast laser sources with pulse duration on the ps time scale provide above-bandgap optical excitation and the emitted free exciton PL intensity is recorded by time-resolved detection schemes. Although the method is widely utilized, three major obstacles often impede an unambiguous interpretation of such free exciton TRPL traces.

1. The time evolution of the photocarrier ensemble results from the convoluted interplay of free exciton formation, thermalization, excess energy relaxation, and radiative and nonradiative decay kinetics [6, 54, 99, 123]. All of these processes may happen on comparable time scales and their relative contributions to the observed PL kinetics depend sensitively on the applied excitation wavelength, excitation density, and lattice temperature.

2. Because of momentum conservation during the luminescence process, only free excitons in the radiative zone at $K \approx 0$ decay radiatively [7, 52, 55]. The time-dependent emission intensity of the free exciton zero-phonon line (FX) is hence *not* a direct measure of the actual time evolution of the free exciton population in the crystal, a fact which is a major obstacle to the unambiguous

interpretation of such (FX) TRPL signals.

3. Observation of the undisturbed *intrinsic* free exciton kinetics requires the investigation of ultra-high purity samples, which are not readily available to all investigators. Even in lightly doped semiconductors, excitons efficiently localize at residual impurity states [47]. Experimental (FX) TRPL transients then often reflect primarily the population dynamics among defect-induced carrier reservoirs [124–127].

Our studies presented in chapters 5 and 6 of this thesis address the convoluted interplay of excess energy relaxation (cooling) and radiative recombination during the decay of a photoexcited hot exciton population. We here investigate a piece of high-purity GaAs (sample B, cf. section 4.2), which because of its exceptionally low defect concentration allows us to study the undisturbed *intrinsic* time evolution of a free exciton ensemble.

In the present chapter, we address a long-standing fundamental question, i.e., the nature of the slow free exciton photoluminescence rise with respect to an ultrafast laser excitation pulse [73, 83, 126, 128–136]. The delayed PL onset has attracted intense research interest for nearly three decades. A general consensus on its microscopic origin, however, has still not been reached.

Clearly, an unequivocal study of the time evolution of a photoexcited free exciton ensemble is challenging because of the inherent interpretation ambiguities of the (FX) zero-phonon line. We, therefore, investigate for the first time the time evolution of an optically excited free exciton ensemble by TRPL traces detected on the free exciton second LO-phonon replica $(FX)-2\hbar\Omega_{\mathrm{LO}}$. The strict K vector selection rule applicable to the (FX) zero-phonon line is fully relaxed for the radiative annihilation of free excitons under simultaneous emission of two LO phonons. This is because the wave vectors of the two LO phonons can always add up such that they compensate for the center of mass momentum of the recombining exciton [7, 8]. In crucial distinction from previous TRPL studies of the (FX) zero-phonon line, we here trace the actual time-evolution of the free exciton density, which is not distorted by the relaxation of large K vector excitons to the radiative zone. Moreover, a time-resolved line shape analysis of the $(FX)-2\hbar\Omega_{\mathrm{LO}}$ replica provides direct experimental access to the exciton cooling curve $T_X(t)$.

Having directly determined the cooling dynamics from experiment, we next address the impact of the exciton cooling on the transient thermodynamic quasi-equilibrium between free excitons and unbound electron-hole pairs, which is fundamentally described by the Saha equation (cf. section 2.4). It has previously been shown that the Saha equation allows for a precise description of the spatially dependent population balance of the partially ionized exciton gas under continuous-wave laser excitation in bulk GaAs [137] (cf. our discussion in chapter 9) and of the time evolution of a photoexcited exciton gas in semiconductor quantum wells [133, 138]. We here demon-

strate that the experimental free exciton TRPL traces in bulk GaAs, and in particular the slow photoluminescence rise, are also consistently described by the shift of the thermodynamic ionization equilibrium from the uncorrelated electron-hole plasma (EHP) to the free exciton state.

5.1 PL rise time of the (FX) zero-phonon line vs. second LO-phonon replica

As a consequence of momentum conservation during the luminescence process, only a subset of the entire free exciton population close to the Brillouin zone center with $K \approx 0$ can recombine radiatively [52, 54, 55] (cf. our discussion in section 2.3). The emission intensity of the (FX) zero-phonon line is hence not a direct measure of the actual free exciton density $n_X(t)$ in the crystal, rendering the interpretation of such (FX) TRPL traces inherently ambiguous. From an investigation of the zero-phonon line alone, it is particularly difficult to conclude whether the slow PL onset results from the relatively slow buildup of a free exciton population or if it merely monitors the arrival of large K vector excitons in the radiative zone.

Fundamentally advancing previous studies of the free exciton zero-phonon line, we analyze TRPL traces detected on the free exciton second LO-phonon replica. As previously discussed (cf. Fig. 4 and our discussion in section 2.3.2), the K vector selection rule that applies to the (FX) zero-phonon line is fully relaxed for the radiative annihilation of free excitons under simultaneous emission of two LO phonons [7, 8]. The time-resolved integrated emission intensity of the $(FX) - 2\hbar\Omega_{\mathrm{LO}}$ phonon replica thereby monitors the unambiguous time evolution of the *entire* exciton population. If the slow (FX) PL onset was mainly caused by the relaxation of large K vector excitons to $K \approx 0$, we would expect a significantly faster luminescence onset of the $(FX) - 2\hbar\Omega_{\mathrm{LO}}$ replica.

We show in Fig. 19 the comparison of TRPL traces detected on the (FX) zero-phonon line and on the $(FX) - 2\hbar\Omega_{\mathrm{LO}}$ replica at two representative excitation densities. Expectedly and in agreement with previous TRPL studies reported in the literature [73, 83, 126, 135, 136], we observe a significantly delayed (FX) PL onset with respect to the excitation laser pulse at both excitation densities.

We first consider the case of moderate excitation density $P_{\mathrm{exc}} = 40\,\mathrm{W\,cm^{-2}}$ (upper panel). Comparison of the (FX) and the $(FX) - 2\hbar\Omega_{\mathrm{LO}}$ luminescence response yields two important observations.

1. Analogous to the (FX) zero-phonon line, we also observe a significantly delayed arrival of the PL maximum of the second LO-phonon replica.

2. Close inspection of the TRPL traces reveals a slight time shift between both curves. The PL maximum of the $(FX) - 2\hbar\Omega_{\mathrm{LO}}$ trace arrives slightly earlier.

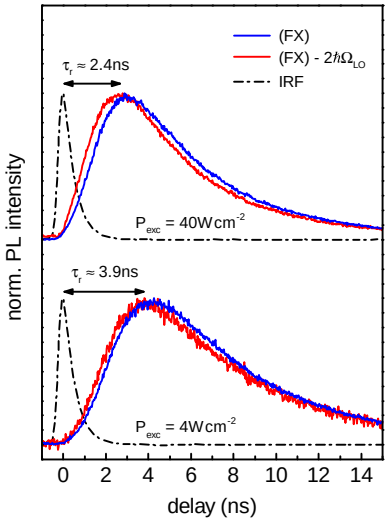

Figure 19: In a TRPL experiment with ultrashort laser excitation pulses, we observe a significantly delayed free exciton PL onset. At moderate excitation density of $P_{\mathrm{exc}} = 40\,\mathrm{W\,cm^{-2}}$, the PL maximum of the (FX) zero-phonon line exhibits a slight additional time delay with respect to the free exciton second LO-phonon replica $(FX) - 2\hbar\Omega_{\mathrm{LO}}$. This slight time shift indicates the slow relaxation of large K vector excitons to the radiative zone at $K \approx 0$. We furthermore observe that the PL rise time τ_r increases for decreasing excitation densities. In the low-excitation limit ($P_{\mathrm{exc}} = 4\,\mathrm{W\,cm^{-2}}$), the PL maxima of both transitions converge. The luminescence onset is then fully dominated by the slow buildup of a free exciton population in the sample.

As a new result, our measurement unambiguously clarifies that the delayed (FX) PL onset is not mainly caused by the relaxation of large K vector excitons to the Brillouin zone center. Monitoring the entire exciton density, the long PL rise time of the $(FX) - 2\hbar\Omega_{\mathrm{LO}}$ replica rather evinces a relatively slow buildup of the free exciton population. Only the slight time shift between both curves, i.e., the delayed arrival of the (FX) PL maximum *with respect to the free exciton population peak* $n_X(t)$, is caused by the relaxation of large K vector excitons to the radiative zone.

Figure 19 furthermore reveals a dependence of the PL rise time τ_r, defined as the time delay before the arrival of the free exciton PL maximum [83], on P_{exc}. At a decreased excitation density of $P_{\mathrm{exc}} = 4\,\mathrm{W\,cm^{-2}}$ (lower panel), the luminescence maxima of both transitions shift to longer delays. Moreover, the TRPL traces of the (FX) zero-phonon line and of the second LO-phonon replica converge. In the low-excitation limit, the time evolution of the free exciton density $n_X(t)$ masks the slight additional time shift between the (FX) and the $(FX) - 2\hbar\Omega_{\mathrm{LO}}$ TRPL traces. The PL onset of both transitions is then fully dominated by the slow free exciton population buildup.

5.2 Qualitative interpretation of the slow free exciton population buildup

Having established that the delayed free exciton PL onset actually mirrors the slow buildup of a free exciton population, we now turn to a discussion of the mechanism that governs the time evolution of the free exciton density $n_X(t)$. In the current section, we briefly outline our qualitative interpretation of the slow PL onset.

Fundamentally, the slow photoluminescence rise is governed by the time-dependent thermodynamic equilibrium between free excitons and the uncorrelated electron-hole plasma described by the Saha equation. As discussed in section 2.4, the population balance between free excitons and the EHP is crucially influenced by both the exciton temperature T_X and the total photocarrier pair density n_0.

In a typical TRPL experiment, off-resonant optical excitation creates an initially hot photocarrier population. The hot carrier cloud cools towards T_L by emission of optical and acoustic phonons and simultaneously dilutes by concurrent radiative decay [6, 85].

At low and medium excitation powers, the EHP is thermodynamically favored at early delays because of the pronounced photocarrier heating. The peak exciton density only occurs after the photocarrier ensemble has sufficiently cooled, such that the population balance shifts from the EHP towards the Coulomb-bound excitons. Although the total photocarrier pair density $n_0(t)$ decreases *monotonically* after the excitation pulse, the exciton density $n_X(t)$ reaches its maximum after a few ns delay with respect to the pulse, thereby causing the slow free exciton PL onset.

At high excitation powers, despite the high initial carrier temperature, exciton formation is still already thermodynamically favored at early delays because of the high pair density n_0. We, therefore, consistently observe in experiment an earlier arrival of the free exciton PL maximum at high excitation densities [cf. Fig. 19].

5.3 Quantitative model description

Since the free exciton PL onset is crucially influenced by the transient photocarrier cooling governing the dynamic equilibrium between free excitons and unbound electron-hole pairs, we first consider the exciton cooling curve $T_X(t)$.

Exciton cooling Previous works have studied the transient cooling of optically excited *hot electron* populations from a time-resolved line shape analysis of the free electron-to-neutral acceptor transition (e,A^0) [99]. On the contrary, the temperature of a free exciton ensemble is not readily obtained from the line shape of the (FX) zero-phonon line and we are not aware of any previous study that reports experimental exciton cooling curves in high-purity GaAs. The exciton temperature, however, can be obtained from the spectral analysis of the (FX) second LO-phonon replica,

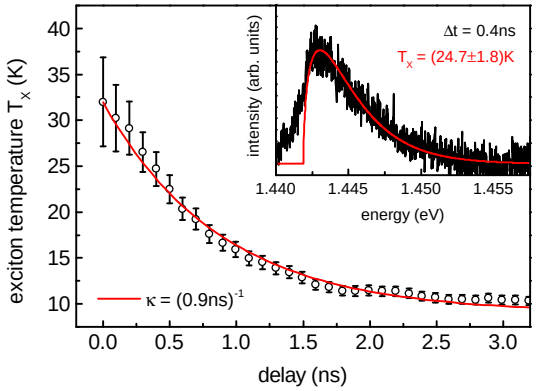

Figure 20: Transient cooling of the nonresonantly excited exciton population. Data points are obtained from Maxwellian line shape analyses of the $(FX)-2\hbar\Omega_{\mathrm{LO}}$ phonon replica. The solid red curve indicates a Newtonian cooling with a time constant $\kappa = (0.9\,\mathrm{ns})^{-1}$. Recombination heating prevents full equilibration of the photocarrier ensemble with the crystal lattice. A representative spectrum and Maxwellian line shape fit to the $(FX)-2\hbar\Omega_{\mathrm{LO}}$ replica is shown in the inset.

which mirrors the density of occupied states of a free exciton population [7, 8] (cf. section 2.3.2). A time-resolved Maxwellian line shape analysis of the $(FX)-2\hbar\Omega_{\mathrm{LO}}$ transition, therefore, provides direct experimental access to the transient temperature of the hot exciton ensemble [70].

A representative cooling curve $T_X(t)$ at $P_{\mathrm{exc}} = 100\,\mu\mathrm{W}$ is shown in Fig. 20.[13] The monotonic decrease of the exciton temperature is well described by straightforward Newtonian cooling

$$\frac{d}{dt}T_X = -\kappa(T_X - T_0) \tag{5.1}$$

with a cooling constant $\kappa = (0.9\,\mathrm{ns})^{-1}$ and a final exciton temperature $T_0 = 9\,\mathrm{K}$ which is higher than the lattice temperature.

Compared with the peculiar temperature dependence of the *electron* cooling rates after R. Ulbrich [99] (cf. section 2.5.2), a constant exciton cooling rate κ allows for a surprisingly good approximation of the actual cooling curve $T_X(t)$ in the range

[13] The data presented in Fig. 20 and Fig. 21 (a) were taken in collaboration with the University of Hannover by M. Beck. In derogation from the setup described in section 3.2.1, optical excitation at $\lambda_{\mathrm{exc}} = 7800\,\text{Å}$ is provided by a pulsed Ti:Sapphire laser. The pulse width of $\approx 2\,\mathrm{ps}$ is determined from autocorrelation measurements. To prevent measurement artifacts originating from previous excitation pulses [136], the repetition rate is reduced to 4 MHz by a pulse picker (extinction ratio $< 1:1500$). The laser beam is focused on the sample surface by a $f = 200\,\mathrm{mm}$ achromatic lens to a $(1/e^2)$ intensity spot diameter of 95 µm. The luminescence is dispersed in a 250 mm focal length imaging spectrometer equipped with a $1200\,\mathrm{mm}^{-1}$ grating. Time resolved PL spectra are detected by a streak camera equipped with a two-dimensional charge-coupled device (CCD). All measurements reported in the present chapter are performed at $T_L = 5\,\mathrm{K}$ lattice temperature.

$9\,\mathrm{K} \leq T_X \leq 32\,\mathrm{K}$. The exact reason why that is remains elusive. We note, however, that the exciton ensemble relaxes its excess energy more efficiently than one would expect from eq. (2.18) for a pure electron population. We speculate that the higher exciton cooling rate reflects the hole contribution to the cooling process, for which ≈ 2.5 times larger cooling rates have been reported [85].

The fact that $T_0 = 9\,\mathrm{K}$ does not coincide with the lattice temperature $T_L = 5\,\mathrm{K}$ is a consequence of momentum conservation during the luminescence process. From the thermalized free exciton ensemble that exhibits a Boltzmann kinetic energy distribution, only excitons at $K \approx 0$ recombine radiatively [7, 52, 55]. The luminescence process, therefore, selectively removes low-energy excitons from the entire ensemble (cf. our discussion in chapter 6). The remaining kinetic energy is redistributed among the left over excitons, the temperature of which (in the absence of competing cooling channels) thus increases. The selective radiative decay of low-energy excitons at $K \approx 0$ effectively serves as a heating mechanism to the exciton population. At long delay times, this *recombination heating* [139, 140] compensates the cooling rate due to acoustic phonon emission and accounts for the discrepancy between T_0 and T_L.

For the purpose of our model description, we verified that the cooling constant κ and the final exciton temperature T_0 do not depend on P_{exc} in the investigated excitation density range. The starting temperatures of the model cooling curves are individually determined for each excitation power P_{exc}.[14]

Time evolution of the free exciton density As time elapses, the photocarrier ensemble dilutes by concurrent free exciton and EHP recombination. For the sake of simplicity we, however, neglect the weaker bimolecular EHP recombination and assume that $n_0(t)$ decays exclusively by the much more efficient channel of free exciton radiative decay [83, 122] (cf. the negligible emission intensity from direct band-to-band transitions in the low-temperature PL spectrum of sample B, Fig. 17). The relative fraction $f_X(n_0, T_X)$ of free excitons in the photocarrier population of pair density n_0 is given by the Saha equation (2.17). The time evolution of the photocarrier pair density $n_0(t)$ is then described by the rate equation

$$\frac{d}{dt} n_0 = -\frac{n_0 \times f_X(n_0, T_X)}{\tau} \tag{5.2}$$

which is coupled with eq. (5.1) by the implicit time dependence of $f_X[n_0, T_X(t)]$. For each excitation density P_{exc}, the ensemble lifetime τ is chosen for best agreement with experiment.

[14] We note, however, that for excitation densities $P_{\mathrm{exc}} > 100\,\mu\mathrm{W}$, the $(FX) - 2\hbar\Omega_{\mathrm{LO}}$ line shape at short delays is severely distorted by the spectrally nearby LO-phonon replica of the donor-acceptor pair transition $(D^0, A_C^0) - \hbar\Omega_{\mathrm{LO}}$, which impedes a robust determination of the starting temperature. From the peculiar temperature dependence of the average cooling rates [99] (Fig. 10), we assume $T_X(0) \approx 32\,\mathrm{K}$ for $P_{\mathrm{exc}} > 100\,\mu\mathrm{W}$.

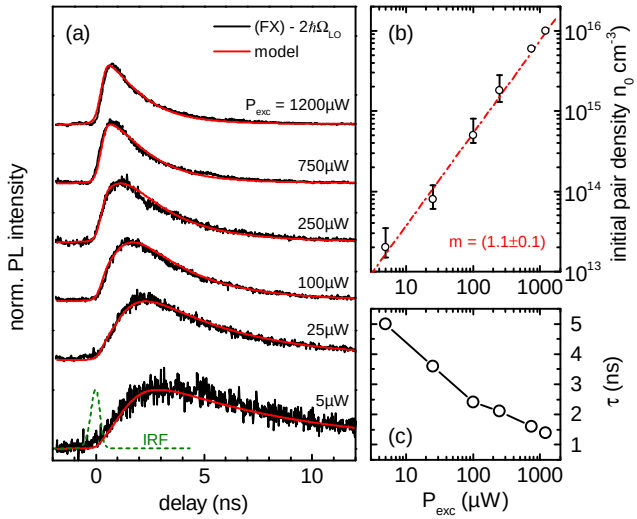

Figure 21: (a) Excitation power dependence of the PL time traces detected on the free exciton second LO-phonon replica $(FX)-2\hbar\Omega_{\mathrm{LO}}$. Solid red lines are our model results. (b) The total photocarrier density per excitation pulse extracted from our model scales linearly with the time-averaged optical excitation density P_{exc}. We note that the PL onset at $P_{\mathrm{exc}} = 750\,\mu\mathrm{W}$ and $1200\,\mu\mathrm{W}$ is dominated by the width of the instrument response function (IRF). We, therefore, disregard the respective data points for the power law fit. (c) Decay times τ used in the model.

Finally, from the Saha equation (2.17), the time evolution of the free exciton density $n_X(t)$ is related to the pair density $n_0(t)$ as

$$n_X(t) = n_0(t) \times f_X(n_0, T_X). \tag{5.3}$$

5.4 Comparison with experiment

A comparison of our conceptual model with the experimental $n_X(t)$ time evolution is reported in Fig. 21 (a). We show here the spectrally integrated emission intensity of the second LO-phonon replica at various excitation densities, which directly monitors the time evolution of the free exciton density $n_X(t)$ [a representative $(FX)-2\hbar\Omega_{\mathrm{LO}}$ spectrum is shown in the inset of Fig. 20].

For each excitation density, we numerically solve the coupled equations (5.1)-(5.3) and fit the convolution of the calculated $n_X(t)$ with the measured instrument response function (IRF) to the $(FX)-2\hbar\Omega_{\mathrm{LO}}$ time traces. Excellent agreement with experiment [Fig. 21 (a)] is obtained by only adjusting the photocarrier density $n_0(t=0)$, i.e., the number of photoexcited electron-hole pairs per excitation pulse, and the ensemble lifetime τ. Our model correctly reproduces the slow buildup of the free exciton population and the shift of the PL maximum as a function of P_{exc}.

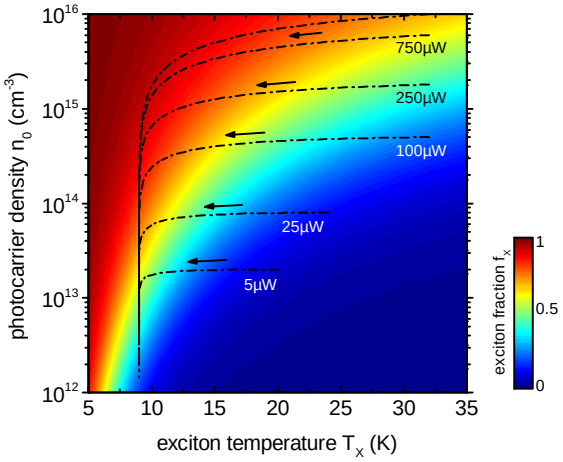

Figure 22: Contour plot of the thermodynamic equilibrium of the partially ionized exciton gas described by the Saha equation. Color indicates the exciton fraction $f_X = n_X/n_0$ in a photocarrier population of total pair density n_0. Exciton formation is thermodynamically favored at high photocarrier densities and low temperatures. Dash-dotted lines indicate the trajectories of the model time traces shown in Fig. 21 (a).

The initial pair density $n_0(t=0)$ obtained from our model analysis is plotted in Fig. 21 (b) as a function of the time-averaged excitation power P_{exc}. We regard the linear scaling of the density $n_0(t=0)$ with P_{exc} as strong evidence that our model captures the essential physics controlling the time evolution of the free exciton population.[15]

The lifetimes τ used in our model are reported in Fig. 21 (c). The decrease for increasing excitation densities is qualitatively explained by our results presented in chapter 6. Efficient exciton-exciton and exciton-free carrier scattering cause a broadening of the (FX) zero-phonon line whose linewidth ΔE increases as a function of the optical excitation density [89]. Since only excitons in the radiative zone with energy $E \leq \Delta E$ recombine radiatively [52, 55], the ensemble lifetime τ consistently decreases for increasing excitation densities. We note that this observation is not in conflict with the relaxed K vector selection rule of the second LO-phonon replica analyzed by us; because of the inherent intensity weakness of the $(FX) - 2\hbar\Omega_{\text{LO}}$ transition, the time evolution of the exciton population is still completely governed by the orders of magnitude stronger (FX) zero-phonon recombination depending on ΔE.

[15] We note that the degeneracy factors of the involved photocarrier species (electrons, holes, and free excitons) are not precisely known, which aggravates a quantitative comparison of the model $n_0(t=0)$ with the estimated photocarrier densities by considering the repetition rate of the laser pulse train and the excitation volume. Since the degeneracy factors only rescale $n_0(t=0)$, but do not depend on the excitation parameters, we investigate the more meaningful scaling behavior of the model peak density with the experimental excitation power (cf. section 9.3). A rough estimate, however, yields a combined degeneracy factor of $g^* \approx 8$.

Figure 22 once again summarizes our model results and provides a particularly instructive picture for the slow (FX) PL onset. Each dash-dotted line in the Saha phase diagram represents the trajectory of a model TRPL trace from Fig. 21 (a). The starting point of each trajectory is given by the initial exciton temperature and the total photocarrier pair density excited per laser pulse. Because of the pronounced overheating, unbound electron-hole pairs are thermodynamically favored at $t = 0$. As time elapses, cooling and concurrent radiative decay account for the delayed arrival of the free exciton population maximum. As the excitation density increases, the increasing initial pair density stabilizes the exciton state already at early times and accounts for the gradual shift of the free exciton population peak to shorter delays.

5.5 Summary and conclusion

We have performed TRPL measurements of the free exciton second LO-phonon replica in a high purity GaAs epilayer to trace the undistorted time evolution of a nonresonantly excited free exciton population. Settling a long-standing fundamental question, our study unambiguously demonstrates that the delayed (FX) PL onset is not caused by mere momentum relaxation of large K vector excitons to the radiative zone, but rather by the transient dynamics of the less frequently considered thermodynamic Saha equilibrium between free excitons and the uncorrelated electron-hole plasma. A conceptual model based on the interplay of transient cooling and concurrent dilution by radiative decay quantitatively describes the slow free exciton photoluminescence rise by the time-dependent population balance between excitons and unbound charge carriers.

Previous TRPL studies of the (FX) PL onset [83] have interpreted their results in terms of the recently proposed Coulomb-correlated electron-hole plasma [11, 12]. We note that throughout the investigated excitation density range, the Coulomb-correlated EHP is not needed for a consistent explanation of the slow (FX) PL onset and for the shift of the luminescence maximum as a function of P_{exc}. The Saha equation rather provides a natural alternative explanation for both the presence of free exciton luminescence at relatively high lattice temperatures (cf. our discussion in section 4.2) and for the slow buildup of a free exciton population following pulsed optical excitation.

Moreover, we have to the best of our knowledge presented the first experimental exciton cooling curve in bulk GaAs. Our study directly reveals that the cooling dynamics of a hot free exciton ensemble is crucially affected by recombination heating. The initially hot exciton cloud does not fully equilibrate with the crystal lattice even after long delay times with respect to the laser excitation pulse. This finding potentially has detrimental implications for the search of excitonic Bose-Einstein condensates, which require the preparation of ultracold free exciton ensembles.

Chapter 6

Free exciton photoluminescence rise beyond Saha's equation

In the previous chapter, we have investigated the free exciton photoluminescence (PL) rise in high-purity GaAs following ultrafast optical excitation. We have demonstrated that the slow free exciton PL onset is caused by the transient cooling of the initially hot photocarrier cloud, which governs the conversion of unbound electron-hole pairs into free excitons.

In the present chapter, we demonstrate that one aspect of the free exciton luminescence kinetics, which is usually masked by the thermodynamic time evolution of the entire photocarrier population (chapter 5), is revealed under quasi-stationary optical excitation conditions. In contrast to virtually all TRPL studies reported in the literature, we here use 85 ns box-shaped laser pules rather than ultrafast optical excitation. This particular excitation scheme reduces the degree of complexity of the free exciton decay process by eliminating the influence of exciton formation [123] and photocarrier thermalization effects [75, 85]. The *free decay*[16] of the exciton population then proceeds from a well-defined steady-state, such that the decay dynamics are solely governed by the interplay of excess energy relaxation (cooling) and free exciton radiative recombination. When the laser pulse is switched off, we observe a prominent increase of the free exciton PL intensity with respect to the emission intensity during the quasi-continuous-wave excitation.

We conclude from the distinct dependence on sample temperature and excitation wavelength that this initial free exciton luminescence increase is also caused by the transient cooling of the hot exciton population. At high excitation densities, however, the PL overshoot after pulse action is not due to the thermodynamic population balance between unbound electron-hole pairs and free excitons, but rather due to the relaxation

[16] The term "free decay" relates to a previous work by H. Münzel et al. [102]. The authors introduce it to contrast their long excitation pulse scheme with the commonly applied ultrashort laser pulses.

of large K vector excitons to the radiative zone.

6.1 Free decay of a photoexcited exciton population

Figure 23 displays representative TRPL transients, recorded on distinct spectral slices of the free exciton recombination line (FX). The measurements are taken at $T_L = 5\,\mathrm{K}$ lattice temperature for a moderate excitation power of $P_{\mathrm{exc}} = 10\,\mu\mathrm{W}$.[17] Optical excitation at $\lambda_{\mathrm{exc}} = 7850\,\text{Å}$ is provided by a step-like modulated diode laser.[18] The time axis is chosen such that the excitation source is switched off at 0 ns delay.

All TRPL transients share two characteristic features. First, when the excitation source is switched on, the PL intensity does not instantly reach its stationary value. The exciton ensemble needs tens of ns to enter a steady-state regime. Second, after the excitation pulse is switched off, the emitted PL intensity *increases* and reaches a maximum after a delay of $\approx 2.5\,\mathrm{ns}$. Depending on the detection wavelength, this relative PL increase is as high as 35 %.

The PL overshoot after the excitation pulse occurs at all spectral positions within the (FX) recombination line. This rules out that the initial PL increase merely results from a spectral shift or transformation of the (FX) line as a function of delay time.

All following measurements are performed with the entrance and exit slits of the monochromator opened such that we detect the spectrally integrated (FX) luminescence as indicated in the inset of Fig. 23.

[17] For the sake of comparability with continuous-wave optical excitation, all P_{exc} readings in this chapter denote the excitation power during the excitation laser pulse rather than the time-averaged excitation density.

[18] We show in Fig. 23 schematically ideal step-like laser excitation, neglecting two imperfections of the actual pulse shape. First, the diode laser exhibits a pronounced overshoot at the rising edge of the excitation pulse. This potentially leads to a distortion of the PL onset [cf. Fig. 26 (a)]. The trailing edge of the excitation pulse, however, is not affected by such a deformation. Second, the 90 to 10 % fall times of the laser pulses are $\approx 2.5\,\mathrm{ns}$. In a "standard" TRPL experiment, which uses ultrafast laser pulses and a TCSPC detection scheme, the width of the instrument response function limits the overall timing resolution of the experiment. Both the time-resolution of the TCSPC hardware *and* the width of the exciting laser pulses are then important. For the case of our long excitation pulses, however, the 2.5 ns slope of the trailing pulse edge does not impair the overall time resolution. This is because during pulse action, a large exciton population is generated. The spurious excitation light during the trailing edge of the laser pulse only accounts for minute corrections to the stationary exciton population, which has built up during the previous 85 ns excitation pulse (compare the long PL rise times). We, therefore, neglect the imperfection of the applied laser pulses in our analysis and reasonably assume step-like laser excitation.

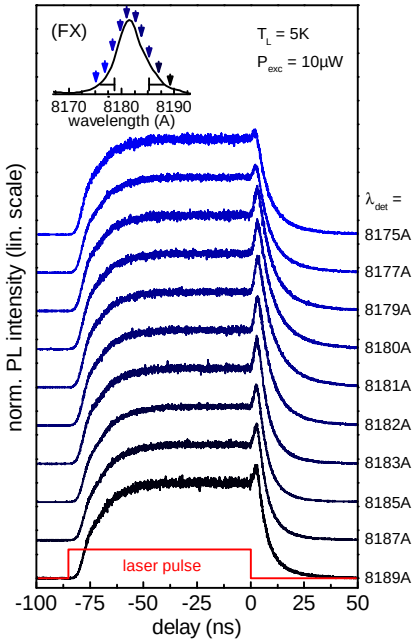

Figure 23: Photoluminescence time traces measured at $T_L = 5\,\mathrm{K}$ for distinct spectral slices λ_{det} of the (FX) recombination line indicated in the inset. The free exciton PL intensity *increases* after the excitation source is switched off at 0 ns delay (cf. red box). Note that the spectral resolution indicated in the inset relates to all following measurements for which we opened the monochromator slits to detect the (FX) line spectrally integrated.

6.2 Dependence of the luminescence overshoot on excitation parameters

Having previously established that the delayed free exciton PL response to ultrafast laser pulses is caused by the transient cooling of the initially hot photocarrier cloud (cf. chapter 5), it is natural to assume that an overheating of the nonresonantly excited exciton population is also the reason for the initial PL increase observed in the free decay experiment. We, therefore, briefly examine the dependence of the (FX) PL overshoot on sample temperature and excitation excess energy to corroborate this hypothesis.

6.2.1 Lattice temperature dependence

We show in Fig. 24 (a) TRPL transients detected on the (FX) line for various sample temperatures. At a fixed excitation power of $P_{\mathrm{exc}} = 10\,\mu\mathrm{W}$, the magnitude of the initial PL increase reduces as the lattice temperature T_L is increased. No significant PL

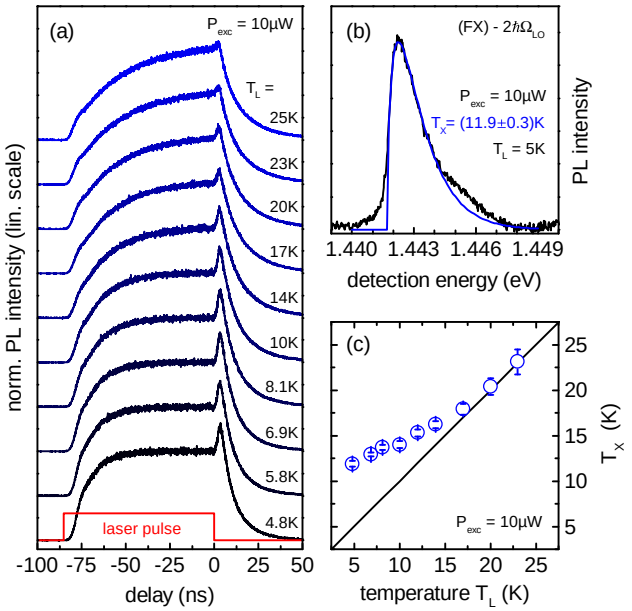

Figure 24: (a) The magnitude of the initial PL increase reduces for increasing lattice temperatures and disappears for $T_L \gtrsim 23\,\mathrm{K}$. (b) Representative line shape analysis of the free exciton second LO-phonon replica from which we obtain the exciton temperature T_X. (c) T_X and T_L converge at the same lattice temperature $T_L \gtrsim 23\,\mathrm{K}$ where the PL overshoot disappears.

overshoot after the excitation pulse is observed for $T_L \gtrsim 23\,\mathrm{K}$. The emitted PL intensity then decays monotonically after pulse action.

This lattice temperature dependence supports our conjecture that the PL overshoot is caused by an overheating of the photoexcited exciton population with respect to the crystal lattice. To highlight the interconnection, we perform a PL experiment under continuous-wave (cw) optical excitation and determine the exciton temperature T_X from a Maxwellian line shape analysis of the second LO-phonon replica of the free exciton transition $(FX) - 2\hbar\Omega_{\mathrm{LO}}$ [7, 8] [Fig. 24 (b)]. The cw excitation power P_{exc} is chosen to match the excitation density during the 85 ns excitation pulse. The exciton temperature obtained from the second LO-phonon replica in the cw measurement is then the same as T_X in the steady-state regime of the time-resolved experiment, i.e., at the moment when the excitation pulse is switched off.

We show in Fig. 24 (c) this steady-state exciton temperature as a function of T_L. At low lattice temperatures, a pronounced heating of the nonresonantly excited exciton ensemble is observed. The magnitude of the overheating reduces for increasing sample temperatures. For $T_L \gtrsim 23\,\mathrm{K}$, the excitons are in thermal equilibrium with the crystal lattice [cf. Fig. 11 (b)]. At the same sample temperature, the PL overshoot in the TRPL experiment disappears, which corroborates the hot exciton population as the cause of

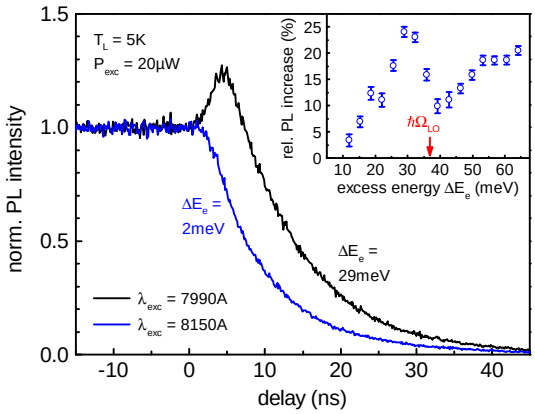

Figure 25: (FX) free decay time traces following nonresonant and near-resonant optical excitation. The initial PL increase disappears at near-band edge optical excitation ($\lambda_{\mathrm{exc}} = 8150\,\text{Å}$). The inset shows the dependence of the relative PL increase on electron excess energy ΔE_e. The dip at $\hbar\Omega_{\mathrm{LO}} = 36.8\,\mathrm{meV}$ excess energy is characteristic of photocarrier heating and confirms our interpretation that the PL increase is related to the steady-state exciton temperature $T_{X,0}$.

the initial PL increase.

6.2.2 Excitation wavelength dependence

Assuming that the PL overshoot after pulse action is caused by pump-induced heating of the carrier system, we expect a distinct dependence of the initial PL increase on the excitation excess energy. This dependence is indeed observed in experiment. We show in Fig. 25 the (FX) TRPL transients recorded at two representative excitation wavelengths λ_{exc}. Under nonresonant optical excitation ($\lambda_{\mathrm{exc}} = 7990\,\text{Å}$), we observe the delayed arrival of the PL emission maximum. When the excitation wavelength is tuned closer to the GaAs band gap, the magnitude of the initial PL increase reduces and eventually disappears at near-resonant optical excitation ($\lambda_{\mathrm{exc}} = 8150\,\text{Å}$).

The detailed excitation wavelength dependence of the initial PL increase is depicted in the inset of Fig. 25. We plot here the magnitude of the PL overshoot as a function of the excess energy $\Delta E_e = (E_{\mathrm{Ph}} - E_g) \times (1 + m_e/m_{hh})^{-1}$ imparted to each photoexcited electron (cf. section 2.5.3).

The overshoot first increases with increasing electron excess energies ΔE_e. This is because for small excess energies, the full amount of ΔE_e is transferred to the photocarrier population and the steady-state exciton temperature hence increases.

Conversely, two competing processes are available for photoexcited electrons with an initial $\Delta E_e \geq \hbar\Omega_{\mathrm{LO}}$: scattering with members of the thermalized steady-state photocarrier population and fast initial LO phonon emission. Only the first process leads to a transfer of the entire amount of excess energy to the photocarrier population.

In the case of fast initial LO phonon emission before carrier-carrier scattering occurs, a significant fraction of the initial electron excess energy is not transferred to the carrier ensemble, but directly to the crystal lattice. Only the remaining fraction of ΔE_e after LO phonon emission is then redistributed in the carrier ensemble [106–108]. We, therefore, observe a deviation from the monotonous progression of the PL overshoot when the excess energy coincides with the GaAs LO phonon energy of $\hbar\Omega_{\mathrm{LO}} = 36.8\,\mathrm{meV}$.

This excess energy dependence, which exhibits a pronounced signature at integral multiples of $\hbar\Omega_{\mathrm{LO}}$, is most characteristic of heating effects in the carrier system [105, 141] [cf. Fig. 11 (c) and our discussion in section 2.5.3]. The dip in the relative PL increase, which resembles the first minimum in the effective carrier temperature due to the efficient excess energy relaxation by fast LO phonon emission, hence corroborates our interpretation that the (FX) luminescence overshoot is caused by the pump-induced overheating of the exciton ensemble.

6.3 Interpretation of the free exciton PL overshoot

Having identified the pump-induced heating of the photoexcited exciton ensemble as the reason for the initial PL increase, we now discuss how the transient cooling after the excitation pulse translates into the observed (FX) PL overshoot.

6.3.1 Transient thermodynamics vs. relaxation to the radiative zone

We inspect the excitation density dependence of the free exciton photoluminescence overshoot shown in Fig. 26 (a). The magnitude of the PL overshoot first increases as P_{exc} is increased from 3 µW to 10 µW. This increase results from the pump power dependence of the steady-state exciton temperature T_X, which increases monotonically for increasing excitation densities [Fig. 26 (b)]. However, the magnitude of the PL overshoot saturates at moderate pump powers $25\,\mu\mathrm{W} \leq P_{\mathrm{exc}} \leq 100\,\mu\mathrm{W}$ and eventually decreases as the pump power is further increased to $P_{\mathrm{exc}} \gtrsim 300\,\mu\mathrm{W}$.

In the light of our previous discussion of the delayed (FX) PL onset following pulsed optical excitation (chapter 5), the initial PL increase at low and moderate exaction densities is readily explained by the thermodynamics of the partially ionized exciton gas described by the Saha equation. During pulse action, the exciton ensemble enters a steady-state regime, which is characterized by a stationary photocarrier pair density and temperature. Because of the Saha ionization equilibrium, only a fraction of all photoexcited electron-hole pairs bind into free excitons. When the laser pulse is switched off, the initially hot photocarrier ensemble cools down and the thermodynamic population balance shifts towards the free exciton state, causing the delayed free exciton PL maximum.

At elevated excitation densities, however, the binding of uncorrelated electron-hole pairs into free excitons is increasingly favored despite the pump-induced heating (cf.

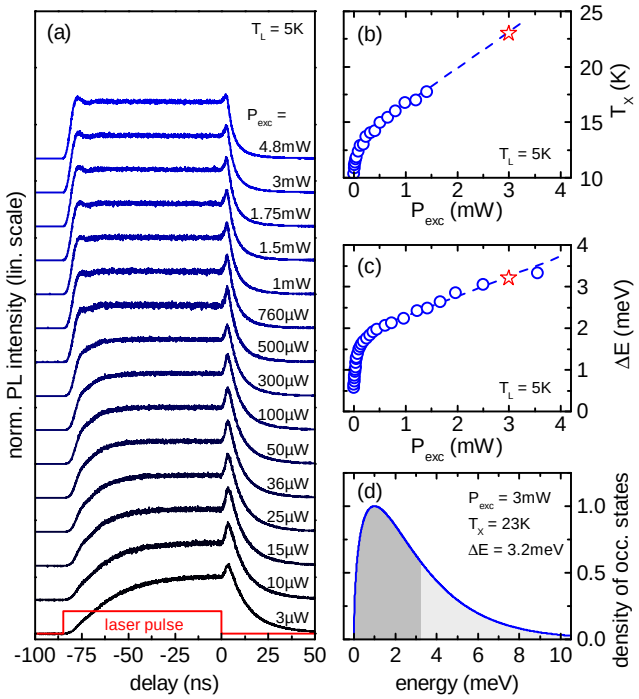

Figure 26: (a) Free exciton PL time traces for various excitation powers. (b) Pump power dependence of the stationary exciton temperature T_X. (c) Broadening of the free exciton zero-phonon line as a function of P_{exc}. ΔE denotes the FWHM of the (FX) line. Red markers indicate the values used in our conceptual model of the (FX) PL overshoot. (d) In the high-excitation limit, the free exciton state is already thermodynamically stabilized during the excitation pulse. The PL overshoot then results from the relaxation of large K vector excitons to the radiative zone. The light shading indicates the reservoir of optically inactive free excitons, which are not visible in the zero-phonon line during the excitation pulse.

the Saha phase diagram in Fig. 22). We, therefore, consistently observe in experiment a saturation and decrease of the initial PL increase at moderate pump powers. This trend is analogous to the drop of the free exciton PL rise time at increased excitation densities discussed in the previous chapter [cf. Figs. 19 and 21 (a)].

In the high-excitation limit, the thermodynamic population balance described by the Saha equation is ultimately dominated by free excitons. Following ultrafast optical excitation at high pump powers, we hence observe an immediate free exciton PL response [cf. Fig. 21 (a)]. By analogy, we would not expect an initial (FX) PL increase in the free decay experiment. Interestingly, Fig. 26 (a) reveals a slight PL overshoot even at the highest pump powers.

To elucidate the microscopic origin of the initial (FX) PL increase in the high-excitation limit, we compare in Fig. 27 the TRPL traces detected on the free exciton

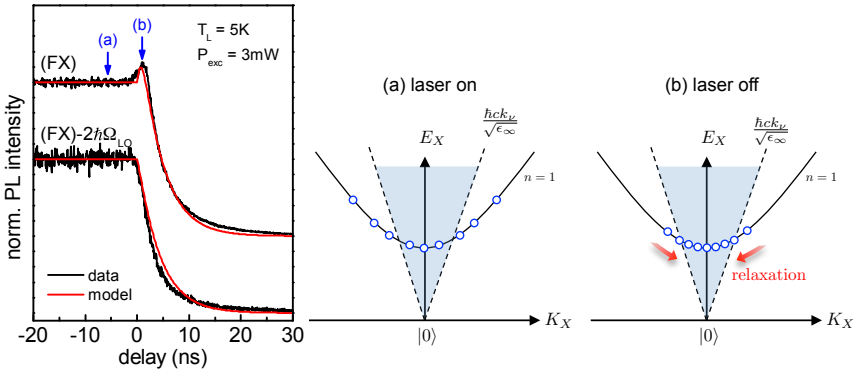

Figure 27: Comparison of free decay TRPL transients detected on the free exciton zero-phonon line and on the second LO-phonon replica. The PL overshoot is only observed on the (FX) zero-phonon line, indicating the relaxation of initially hot excitons to the radiative zone (cf. blue-shaded area in the schematic drawing). Conversely, the total exciton density decreases monotonically after the excitation pulse.

zero-phonon line and on the second LO-phonon replica at $P_{\mathrm{exc}} = 3\,\mathrm{mW}$. Importantly, the PL overshoot is only observed on the zero-phonon line while the emission intensity of the second LO-phonon replica decreases monotonically after pulse action. The absence of the PL overshoot of the $(FX) - 2\hbar\Omega_{\mathrm{LO}}$ replica evinces that it is not an increase of the total exciton density that causes the initial (FX) PL increase.

Our qualitative interpretation of the free exciton PL overshoot in the high-excitation limit is schematically depicted in Fig. 27. Because of photocarrier heating during the excitation pulse, free excitons accumulate at large K vector states where they are protected against radiative decay. After switching off the pump pulse (i.e., the external heat source), the exciton population shifts towards the Brillouin zone center by relaxing its excess energy to the crystal lattice. The experimentally observed (FX) PL overshoot thus monitors the arrival of the initially hot excitons at the radiative zone.

In the following section, we conceive a straightforward conceptual model to substantiate our physical picture of the (FX) PL overshoot.

6.3.2 Model description

The excess energy relaxation of the initially hot exciton ensemble is described by the same cooling dynamics that we established for the here investigated sample in the previous chapter (sample B). In this high-purity GaAs epilayer, the transient exciton temperature is described by Newtonian cooling

$$\frac{d}{dt}T_X = -\kappa\,(T_X - T_0) \tag{6.1}$$

with a cooling constant $\kappa = (0.9\,\mathrm{ns})^{-1}$ and a final exciton temperature of $T_0 = 9\,\mathrm{K}$. The 23 K starting temperature of the cooling curve is estimated from an extrapolation of the experimental P_{exc}-progression obtained from cw spectroscopy of the $(FX) - 2\hbar\Omega_{\mathrm{LO}}$ line [Fig. 26 (b)].

We next consider the decay of the free exciton population. We assume a parabolic exciton center-of-mass kinetic energy dispersion with a density of states $D_X(E_X) \propto \sqrt{E_X}$ and use Boltzmann statistics to describe the exciton kinetic energy distribution function of the thermalized ensemble. Only the fraction

$$r(T_X) \propto \int_0^{\Delta E} dE_X \sqrt{E_X} \times \exp\left[-E_X/(k_B T_X)\right] \tag{6.2}$$

of the entire exciton population is close enough to the Brillouin zone center to contribute to radiative decay [52,55]. The cutoff-energy $\Delta E = 3.2\,\mathrm{meV}$ of the radiative zone is the experimentally observed PL linewidth of the (FX) zero-phonon line at $P_{\mathrm{exc}} = 3\,\mathrm{mW}$ [cf. Fig. 26 (c)].[19] Since only the fraction $r(T_X)$ of the entire free exciton population decays radiatively, the time evolution of the total exciton density n_X is described by the rate equation

$$\frac{d}{dt} n_X = -\frac{n_X}{\tau_X} r(T_X) \tag{6.3}$$

where $\tau_X = 4\,\mathrm{ns}$ [52] denotes the intrinsic radiative lifetime of optically active free excitons with $E_X \leq \Delta E$. The momentary PL intensity is $\propto |\frac{d}{dt} n_X(t)|$. Figure 27 shows that our conceptual model reproduces both the magnitude and the delayed arrival of the PL overshoot.

The starting point of the conceptual model, i.e., the free exciton density of occupied states during the excitation pulse, is depicted in Fig 26 (d). The dark shading indicates the fraction of optically active excitons. During the excitation pulse, excitons with $E \geq \Delta E$ (light shading) are not subject to radiative decay. As time elapses, the mean energy of the ensemble reduces and the density of occupied states narrows. Although the total exciton density decreases monotonically after the excitation pulse, the number of optically active excitons *in the radiative zone* temporarily peaks after a delay of $\approx 2.5\,\mathrm{ns}$.

Our conceptual model certainly draws an oversimplified picture of the convoluted interplay of exciton cooling and radiative recombination by neglecting the thermodynamic population balance between free excitons and the uncorrelated electron-hole plasma (EHP). In the high-excitation limit, however, it demonstrates an aspect of the free exciton luminescence kinetics that is obscured in typical TRPL studies by the overall time evolution of the entire photocarrier population.

[19] For a full quantitative description of the initial (FX) PL increase, also the cut-off energy ΔE should enter the model as an implicitly time-dependent quantity. This would, however, involve additional assumptions and model parameters while not providing a better conceptual understanding of the PL overshoot.

We finally note that all TRPL traces in the free decay experiment deviate from a single exponential decay. The exciton population always decays slower (less efficiently) at longer delays. Two distinct mechanisms account for this trend.

1. In the framework of our conceptual model, such deviations are expected from the implicit time dependence of the momentary decay rate $r[T_X(t), \Delta E(t)]\tau_X^{-1}$. Resonant optical excitation would in principle minimize the pump-induced exciton heating and thus eliminate the implicit time dependence due to the transient cooling after pulse action. However, the implicit time dependence of the decay rate $r\tau_X^{-1}$ due to the (FX) zero-phonon linewidth remains. After pulse action, the photocarrier ensemble dilutes and the cut-off energy ΔE decreases. As time elapses, the relative fraction of excitons in the radiative zone decreases, such that the entire exciton population then decays less efficiently.

2. The diluting photocarrier population favors the dissociation of free excitons into unbound electron-hole pairs due to the Saha thermodynamic equilibrium [10, 138]. Compared with free exciton radiative recombination, the bimolecular decay of the EHP is significantly less efficient [83, 122]. The time-dependent population balance between free excitons and the uncorrelated EHP, therefore, also renders the momentary decay rate of the entire photocarrier ensemble implicitly time-dependent.

Part III

Spatially resolved PL spectroscopy of hot excitons in GaAs

Chapter 7

Dimensional crossover of free exciton diffusion in etched GaAs wire structures

In spatially resolved photoluminescence (SRPL) experiments, the excitation laser beam is tightly focused to a typical spot diameter of a couple of μm on the sample surface. Electrons, holes, and excitons, which are only created in this relatively small excitation volume, move freely through the crystal until they are eventually captured by impurities or annihilate by radiative or nonradiative decay. In high purity semiconductors that exhibit low residual impurity concentrations, the length scale of photocarrier migration can significantly exceed the spatial extent of the pump spot. SRPL detection schemes monitoring the spatial distribution of the luminescence intensity then provide direct experimental access to photocarrier transport processes. In distinction from traditional transport experiments, spatially resolved optical spectroscopy techniques obviate the application of electric fields and are not limited to the investigation of charged particles.

Chapters 7 – 9 of this thesis are devoted to such SRPL experiments to study the diffusion of free excitons in high-purity GaAs. We, therefore, discuss in the present chapter the solutions of the stationary photocarrier diffusion equation in representative sample geometries and compare the calculated diffusion profiles with experimental exciton density profiles.

We assess the stationary free exciton diffusion profiles by the spectrally integrated emission intensity of the free exciton second LO-phonon replica. This allows us to circumvent the inherent interpretation ambiguities of the previously investigated zero-phonon line. We demonstrate that intrinsic free exciton diffusion profiles, which are correctly described by the commonly used formulation of the photocarrier diffusion equation, are only observed *under strictly resonant optical excitation*. Even under slightly off-resonant excitation, the exciton diffusion profile is severely distorted by

local heating in the photocarrier system.

Having established suitable excitation conditions for the observation of undistorted exciton diffusion profiles by the SRPL technique, we investigate the effect of a geometric constraint on the diffusive expansion of a locally excited free exciton packet. We, therefore, study the evolution of the stationary exciton diffusion profiles in etched GaAs wire structures of varying widths $4\,\mu\text{m} \leq w \leq 40\,\mu\text{m}$. In the as-grown sample (sample B, cf. section 4.2), the exciton diffusion profile is described by the stationary solution to the two-dimensional photocarrier diffusion equation. This is because the large diffusion length L renders the 1.5 µm thin slab of epitaxial GaAs an effectively two-dimensional model system. We observe a dimensional crossover when the wire width w is gradually reduced. When the lateral width w falls below the diffusion length L, the sample geometry becomes effectively one-dimensional. The experimental exciton diffusion profile is then expectedly reproduced by the stationary solution to the 1D photocarrier diffusion equation.

7.1 The photocarrier diffusion equation

The spatiotemporal expansion of a locally excited photocarrier packet is fundamentally described by the standard diffusion equation [142]

$$\frac{\partial}{\partial t} n(\mathbf{x},t) = \nabla \cdot [D\, \nabla n(\mathbf{x},t)] \tag{7.1}$$

where $n(\mathbf{x},t)$ denotes the photocarrier density and D the diffusion coefficient. Unless otherwise noted, we assume that the diffusion constant D is really a constant and does not depend on the spatial coordinate $\mathbf{x}$. We incorporate two additional terms into eq. (7.1) to adapt to the actual conditions in a typical SRPL experiment. The first one is a loss term that accounts for radiative decay processes. The second one is a generation term that represents the continuous-wave or pulsed laser excitation source. The inhomogeneous partial differential equation describing photocarrier diffusion in bulk semiconductors then reads [143, 144]

$$\frac{\partial}{\partial t} n(\mathbf{x},t) = D\, \nabla^2 n(\mathbf{x},t) - \frac{n(\mathbf{x},t)}{\tau} + g(\mathbf{x},t) \tag{7.2}$$

with a characteristic decay time τ and a generation rate $g(\mathbf{x},t)$ due to optical excitation.

The assumption of a spatially isotropic diffusion process allows for a further simplification of eq. (7.2). The photocarrier density profile $n(\mathbf{x},t) \rightarrow n(r,t)$ then depends only on the radial distance r with respect to the excitation laser spot.[20] The

[20] In polar coordinates, the radial distance is $r \geq 0$. However, we use the term "radial distance" in a looser and broader sense throughout this thesis. This is because experimental SRPL images are most often radially symmetric with respect to the pump spot. We then typically show centrical line scans

diffusion equation is written in polar coordinates as

$$\frac{\partial}{\partial t}n(r,t) = D\,\nabla_r^2 n(r,t) - \frac{n(r,t)}{\tau} + g(r,t). \tag{7.3}$$

Depending on the dimensionality of the diffusion volume, the one-, two-, or three-dimensional version of the Laplacian ∇_r^2 has to be inserted. Moreover, suitable boundary conditions must be chosen to reflect the actual sample geometry.

7.2 Stationary solutions to the one- and two-dimensional photocarrier diffusion equation

Analytical solutions to eq. (7.3) are not found for some widely used sample geometries, e.g., a three-dimensional half-space. The experiments presented in this chapter are, therefore, performed on a 1.5 µm thick epilayer of high-purity GaAs sandwiched between two GaAs/$Al_{0.09}Ga_{0.91}As$ superlattices (sample B, cf. section 4.2), which confine all photocarriers to the active layer. The characteristic diffusion length $L = \sqrt{D\tau}$ here exceeds the thickness of the epilayer by approximately one order of magnitude (see discussion below), rendering the lateral diffusion of free excitons in our sample effectively a two-dimensional problem [145]. We will later investigate the evolution of the stationary free exciton diffusion profiles in effectively one-dimensional etched GaAs wire structures. We, therefore, briefly review the analytical solutions of the one- and two-dimensional photocarrier diffusion equation under continuous-wave optical excitation.

Stationary solution to the two-dimensional diffusion equation The radially symmetric stationary photocarrier diffusion equation is written in two spatial dimensions as

$$D\left[\frac{\partial^2}{\partial r^2}n(r) + \frac{1}{r}\frac{\partial}{\partial r}n(r)\right] - \frac{n(r)}{\tau} + g(r) = 0. \tag{7.4}$$

The Green's function solution for a continuous-wave (cw) point source $g(r) = \delta(r)$ located at $r = 0$ is given by [146, 147]

$$G(r) = \frac{1}{2\pi D}\,K_0\left(\frac{r}{\sqrt{D\tau}}\right) \tag{7.5}$$

where K_0 denotes the zeroth-order modified Bessel function of the second kind. The characteristic length scale $L = \sqrt{D\tau}$ is commonly referred to as the *diffusion length*. The stationary diffusion profile $n(r)$ for an arbitrary source term $g(r)$, e.g., a Gaussian

through the two-dimensional SRPL image including positive and negative lateral distances to emphasize the symmetry of the data set. Using established nomenclature, the x-axis is then labelled "radial distance", although negative distances are included.

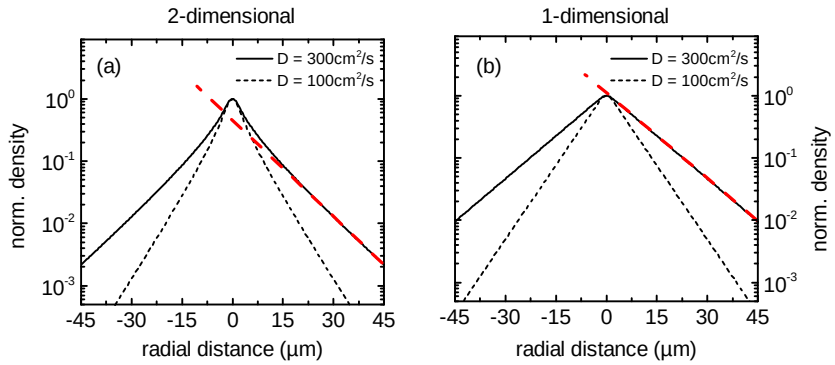

Figure 28: Solutions to the stationary photocarrier diffusion equation in (a) two and (b) one spatial dimension. The $(1/e)$ full width of the Gaussian excitation spot is 3.6 µm, the photocarrier lifetime is 3 ns. Note the slightly different scaling of the diffusion profiles for $|r| \gg \sqrt{D\tau}$ and the characteristic cusp at the center of optical excitation, which crucially distinguishes the 2D from the 1D solution.

laser excitation spot, is then given by the convolution of the Green's function solution $G(r)$ with the excitation profile $g(r)$.

Stationary solution to the one-dimensional diffusion equation The stationary photocarrier diffusion equation in one spatial dimension reads

$$D\,\frac{\partial^2}{\partial r^2}n(r) - \frac{n(r)}{\tau} + g(r) = 0 \tag{7.6}$$

whose Green's function solution for a cw point source $g(r) = \delta(r)$ is given by

$$G(r) = \frac{\sqrt{D\tau}}{2D}\exp\left(-\frac{|r|}{\sqrt{D\tau}}\right). \tag{7.7}$$

The stationary solution for an arbitrary excitation profile $g(r)$ is, here too, obtained from a convolution of the Green's function $G(r)$ with the excitation spot $g(r)$.

Comparison of 1D and 2D stationary diffusion profiles The two-dimensional and one-dimensional steady-state solutions of the photocarrier diffusion equation are displayed in Fig. 28 for two representative values of the diffusion coefficient D. We here assume a Gaussian excitation spot of 3.6 µm $(1/e)$ full width [cf. Fig. 13 (d)] and a typical free exciton lifetime of $\tau = 3$ ns [52]. For both sample dimensionalities, a larger diffusion coefficient expectedly leads to a broader diffusion profile.

The dashed tangent in Fig. 28 (a) indicates that the modified Bessel function $K_0(r/\sqrt{D\tau})$ scales like $\propto \exp[-|r|(0.9\sqrt{D\tau})^{-1}]$ for large $|r| \gg \sqrt{D\tau}$. More importantly, the tangent emphasizes the cusp around the center of excitation, which is the

characteristic feature of the 2D solution resulting from the distinct shape of the Bessel function. In a semilogarithmic plot, the 1D solution rather appears as a straight line [Fig. 28 (b)].

It is the cusp associated with the Bessel function that crucially distinguishes the stationary diffusion profile in a two-dimensional diffusion volume from that in a one-dimensional sample. We will later identify the dimensional crossover of free exciton diffusion in the etched wire structures from comparison of the experimental stationary diffusion profiles with the expected 1D and 2D solutions.

7.3 Correct determination of undistorted free exciton diffusion profiles

Having discussed the expected exciton density profiles in a one- and two-dimensional diffusion volume, we next examine the impact of optical excitation conditions on the *experimentally observed* exciton diffusion profiles. We, therefore, report in Fig. 29 the transformation of the experimental free exciton diffusion profile in the as-grown sample B as a function of the excitation wavelength λ_{exc}.

We have previously discussed that the PL intensity of the free exciton zero-phonon line (FX) only traces the subset of the free exciton ensemble that resides in the vicinity of the Brillouin zone center (cf. our discussion in section 2.3.1 and chapter 6). To monitor the *total* free exciton density $n_X(r)$, we plot in Fig. 29 the spectrally integrated emission intensity of the second LO-phonon replica $(FX) - 2\hbar\Omega_{\mathrm{LO}}$ of the free exciton transition [7, 8].

Under resonant optical excitation at the free exciton resonance ($\lambda_{\mathrm{exc}} = 8180\,\text{Å}$), the diffusion profile reveals the characteristic Bessel function shape associated with the stationary solution to the radially symmetric photocarrier diffusion equation in two spatial dimensions [Fig. 28 (a)]. The solid red line indicates a fit to the data, from which we obtain the diffusion length $L = (10.5 \pm 0.3)\,\mu\text{m}$.[21] Assuming a free exciton lifetime of $\tau = 3\,\text{ns}$ [52], this diffusion length corresponds to an exciton diffusion coefficient of $D = (371 \pm 24)\,\text{cm}^2\,\text{s}^{-1}$.

Figure 29 evinces a drastic transformation of the exciton diffusion profile as a function of the excitation wavelength. As we tune λ_{exc} to shorter wavelength (i.e., larger excess energies), the characteristic cusp around $|r| = 0$ associated with the Bessel function is washed out and the $n_X(r)$ profile flattens. A significant rounding of the diffusion profile is already seen at $\lambda_{\mathrm{exc}} = 8150\,\text{Å}$, which corresponds to an electron excess energy of merely $\Delta E_e = 2\,\text{meV}$ [105]. Obviously, the diffusion profile is then no longer correctly reproduced by the commonly used formulation of the photocarrier

[21] The fact that the characteristic diffusion length L significantly exceeds the 1.5 µm thickness of the GaAs epilayer justifies *a posteriori* our assumption that the diffusion process in the thin semiconductor slab is described by the two-dimensional photocarrier diffusion equation.

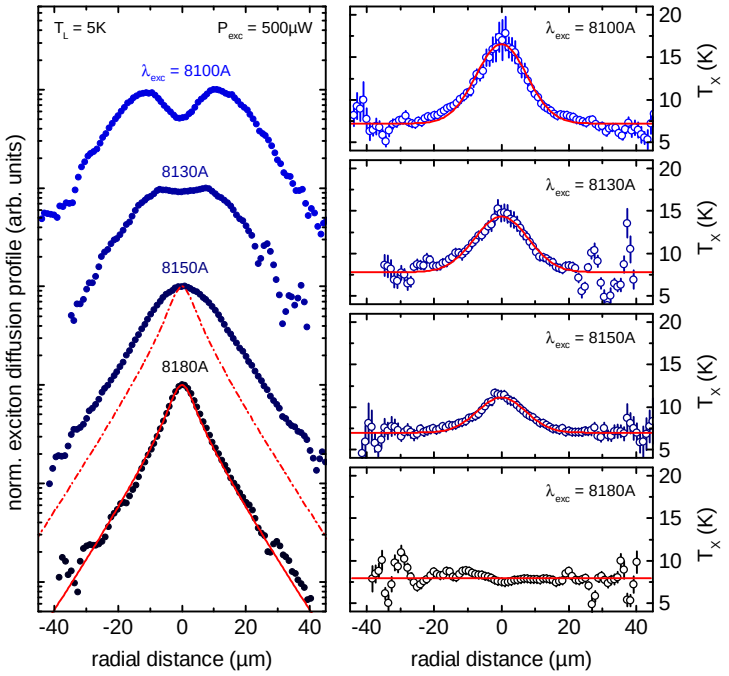

Figure 29: Transformation of the exciton diffusion profile as a function of the excitation wavelength. The profiles are vertically offset for clarity. Data points indicate the spectrally integrated emission intensity of the free exciton second LO-phonon replica. From a spatially resolved line shape analysis of the $(FX)-2\hbar\Omega_{\mathrm{LO}}$ transition, we directly obtain the exciton temperature profiles $T_X(r)$ at each excitation wavelength. Only in the case of resonant optical excitation ($\lambda_{\mathrm{exc}} = 8180\,\text{Å}$) is the resulting diffusion profile correctly described by the steady-state solution to the 2D diffusion equation (solid red line). Slight off-resonant optical excitation ($\lambda_{\mathrm{exc}} = 8150\,\text{Å}$) causes already a localized overheating in the exciton ensemble, which results in severe distortions of the experimental $n_X(r)$ profile.

diffusion equation. For comparison and to highlight the deviation from the analytical 2D solution, we show the fit to the $\lambda_{\mathrm{exc}} = 8180\,\text{Å}$ data set by the dash-dotted line.

As the excitation excess energy is further increased, the flattening of the diffusion profile progressively evolves into a pronounced quench of the free exciton density at the center of optical excitation.

To elucidate the reason for the peculiar transformation of the diffusion profile, we show in Fig. 29 on the right-hand side the corresponding exciton temperature profiles $T_X(r)$ obtained from spatially resolved Maxwellian line shape analyses of the $(FX)-2\hbar\Omega_{\mathrm{LO}}$ phonon replica [7, 8]. Only in the case of resonant optical excitation ($\lambda_{\mathrm{exc}} = 8180\,\text{Å}$), the exciton temperature profile is flat, i.e., T_X is constant at all distances r from

the excitation center.[22] Slightly off-resonant optical excitation ($\lambda_{\mathrm{exc}} = 8150\,\text{Å}$) causes already a significant overheating at the pump spot. At shorter excitation wavelengths (larger excitation excess energies), the peak exciton temperature $T_X(r=0)$ gradually increases.

The distortion of the experimental $n_X(r)$ profile from the expected Bessel function shape is unambiguously correlated with the spatial temperature gradient in the exciton system. The deviation from the calculated diffusion profile [eq. (7.5)] is caused by the localized overheating in two distinct ways.

1. The stationary solutions of the one- and two-dimensional radially symmetric photocarrier diffusion equations were derived under the assumption of a spatially non-varying diffusion coefficient D. This seemingly natural approximation fails under the practical excitation conditions in most spatially resolved spectroscopy experiments. Such experiments necessitate the use of focused laser sources, which unavoidably cause a localized overheating in the carrier system at the pump spot. Since the diffusion coefficient is typically a strong function of the temperature [148–151], local heating directly renders the diffusion coefficient $D \rightarrow D[T_X(r)]$ spatially dependent.

   A local increase of the diffusivity D at the hot spot would indeed account for a flattening of the observed diffusion profile. Such heating effects have previously been shown to influence the steady-state electron spin diffusion profiles in GaAs [152] and also prominently alter the transient diffusive expansion of an electron spin packet following pulsed optical excitation [153].

2. Recalling our discussion of the Saha equation (cf. section 2.4), the exciton temperature also crucially influences the thermodynamic population balance between free excitons and unbound charge carriers. An overheating in the photocarrier ensemble at the excitation center causes the thermal breakup of Coulomb-bound free excitons into uncorrelated electron-hole pairs. At sufficient peak temperatures, this quenching of the free exciton density eventually manifests as a concentric free exciton ring around the pump spot. We will discuss this free exciton ring formation in detail in chapter 9.

Our analysis unambiguously demonstrates that undistorted stationary exciton diffusion profiles, which are correctly described by the commonly used formulation of the photocarrier diffusion equation (7.3), are only observed under strictly resonant optical excitation. All further measurements presented in this chapter are hence performed at $\lambda_{\mathrm{exc}} = 8180\,\text{Å}$ excitation wavelength. We verified that the experimental $n_X(r)$ profile

[22] A deviation of the exciton temperature $T_X \approx 8\,\mathrm{K}$ from the lattice temperature $T_L = 5\,\mathrm{K}$ is most probably a consequence of the recombination heating effect [139, 140] (cf. our discussion in sections 5.3, 8.2, and 9.2).

does virtually not depend on the excitation power P_{exc} for the case of resonant optical excitation at the free exciton resonance.[23]

7.4 Free exciton diffusion in etched GaAs wire structures

7.4.1 Sample preparation

The GaAs wire structures for the investigation of geometric constraints on the diffusion of free excitons are prepared by the following process. A piece of the as-grown sample wafer is covered with an organic photo resist. Standard optical lithography is used to define the desired wire geometries. After development of the resist, a BaF_2/Cr etch shield is deposited on the later channels. The uncovered regions of the sample are etched down to the GaAs buffer in an Ar/Cl_2 plasma by inductively coupled plasma reactive-ion etching (ICP-RIE), such that the active GaAs layer only remains in the lithographically defined stripes. After etching, the BaF_2/Cr etch shield is removed in distilled H_2O.

A scanning electron microscopy (SEM) overview image of the finished sample is shown in Fig. 30 (a). The lateral wire widths w range from 4 to 40 µm; the wire length is 200 µm. A close-up front view of the 40 µm structure is displayed in Fig. 30 (b). The ICP-RIE dry-etching process yields remarkably well-defined stripes with perpendicular sidewalls. The position of the active GaAs layer in the sandwich structure is schematically indicated by the white marker.

7.4.2 Geometry effects on the stationary exciton diffusion profiles

Having established the appropriate excitation wavelength for the detection of undistorted free exciton diffusion profiles, we now examine the influence of a geometric constraint on the diffusion of free excitons. We, therefore, focus our laser excitation spot on the etched wire structures and detect the stationary luminescence profiles along the x direction, i.e., parallel to the stripes (cf. schematic drawing in Fig. 31). Figures 31(a)-31(d) summarize the evolution of the free exciton diffusion profile in the etched wire structures as a function of the wire width w. Data points indicate the spectrally integrated emission intensity of the free exciton second LO-phonon replica.

We compare the measured diffusion profiles with numerical solutions of the photocarrier diffusion equation for the respective sample geometries. We use a commercial finite-element solver to calculate the exciton density distribution $n(x,y)$ in the x-y-plane. The source term (the 3.6 µm Gaussian excitation spot) is positioned at the center of

[23] A slight broadening of the experimentally observed diffusion profile at increased P_{exc} is presumably a consequence of the modified population balance between free excitons and the uncorrelated electron-hole plasma. Nonetheless, the spatial density profile is always perfectly described by the Bessel function solution to the radially symmetric two-dimensional photocarrier diffusion equation.

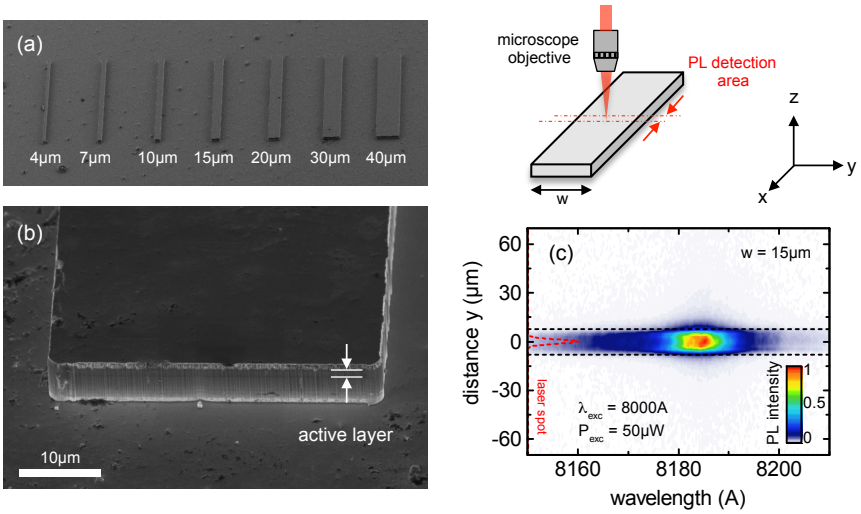

Figure 30: (a) Scanning electron microscopy (SEM) overview image of the investigated sample. (b) SEM image of the $w = 40\,\mu\text{m}$ wire. The ICP-RIE etch process yields remarkably well-defined wire structures, which exhibit perfectly rectangular sidewalls. (c) Representative SRPL image obtained on the $w = 15\,\mu\text{m}$ structure with the spatial PL detection axis aligned perpendicularly to the stripe. Optically excited free excitons are effectively constrained to the etched structure. No depletion at the channel edge is observed.

the simulation volume. The boundary conditions reflecting the sample geometry are motivated by experiment.

To this end, we show in Fig. 30 (c) a representative SRPL image obtained on the $w = 15\,\mu\text{m}$ structure with the spatial PL detection axis aligned perpendicularly to the stripe, i.e., along the y direction. Luminescence is only detected at distances $|y| \leq \frac{w}{2}$, indicating that optically excited excitons are effectively constricted to the etched wire structure and cannot escape the channel.[24] We thus assume zero exciton flux $\frac{\partial}{\partial y} n(x,y) = 0$ through the lateral channel sidewalls. We verified that the choice of boundary conditions at the front face and backside of the $200\,\mu\text{m}$ long stripes (where the exciton density has effectively dropped to zero) does not affect the simulation result. Solid blue lines in Fig. 31 are centrical line scans through the two-dimensional $n(x,y)$ simulation result. For each wire width w, the diffusion length L is fitted for best agreement with experiment.

As discussed in the previous section, we find an exciton diffusion length of $L = (10.5 \pm 0.3)\,\mu\text{m}$ in the as-grown sample [Fig. 31 (a)], which assuming a typical free exciton lifetime of $\tau = 3\,\text{ns}$ [52] corresponds to a diffusivity of $D = (371 \pm 24)\,\text{cm}^2\,\text{s}^{-1}$.

[24] We speculate that the slight halo (which is most pronounced around the peak PL intensity) is caused by stray luminescence refracted towards the microscope objective when exiting the wire or by the unavoidable aberration when imaging the steep edge of the etched stripe.

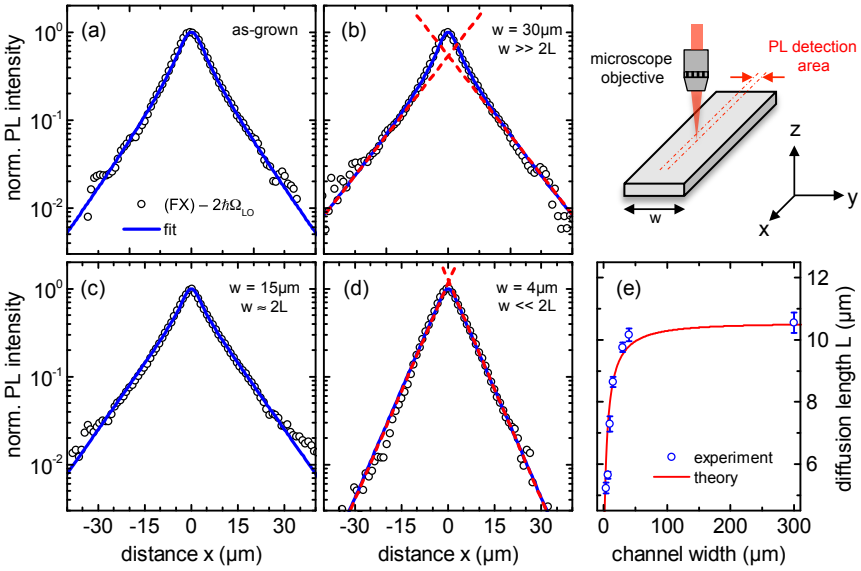

Figure 31: Evolution of the free exciton diffusion profile as a function of the wire width w. Resonant optical excitation ($\lambda_{\mathrm{exc}} = 8180\,\text{Å}$) prevents local heating in the exciton system. Data points indicate the spectrally integrated emission intensity of the $(FX) - 2\hbar\Omega_{\mathrm{LO}}$ replica. (a,b) For $w \gg 2L$ with $L = \sqrt{D\tau}$, the sample geometry remains effectively two-dimensional and the diffusion profile is given by a Bessel function. Dashed tangents emphasize the characteristic cusp of the diffusion profile at the pump spot. (c) For decreasing wire widths w, the stationary diffusion profile is increasingly affected by the channel sidewalls. (d) As expected from the stationary solution to the one-dimensional diffusion equation, the diffusion profile drops off exponentially in the limit of very narrow wires $w \ll 2L$. (e) The decrease of the diffusion length L in the narrow stripes is caused by the collapse of the free exciton lifetime τ due to surface recombination at the etched channel sidewalls.

The large diffusion length L, which significantly exceeds the 1.5 µm thickness of the active GaAs layer, renders the diffusion volume effectively two-dimensional. The stationary exciton density profile, therefore, exhibits the characteristic cusp around the pump spot associated with the Bessel function solution to the 2D stationary photocarrier diffusion equation.

For comparatively broad stripes $w \gg 2L$ [Fig. 31 (b)], the sample geometry remains effectively two-dimensional and the resulting diffusion profile hence remains unchanged. Dashed tangents are shown to indicate the exponential drop-off of the diffusion profile at large distances from the pump spot and to emphasize the cusp around $x = 0$.

At decreased $w = 15\,\mu\text{m}$ [Fig. 31 (c)], the lateral wire width becomes comparable to two times the diffusion length L and the cusp around $x = 0$ is progressively washed out. This is because more excitons now diffusively reach the channel edge, such that

the lateral boundaries increasingly affect the stationary diffusion profile.

In the limit of very narrow channels $w \ll 2L$, the sample geometry becomes effectively one-dimensional. This dimensional crossover is consistently seen in Fig. 31 (d) where we show the measured exciton diffusion profile in the 4 µm wire. Dashed tangents emphasize that the diffusion profile now drops off exponentially at *all* radial distances from the pump spot, which expectedly mirrors the analytical solution to the 1D diffusion equation.

7.4.3 Influence of the wire sidewalls on the exciton diffusion length

In our finite element simulation, the only fitting parameter for the stationary diffusion profiles is the characteristic diffusion length $L = \sqrt{D\tau}$ [cf. eqs. (7.5) and (7.7)]. The fitted diffusion lengths L in the etched wire structures are plotted in Fig. 31 (e) as a function of the wire width w (the value obtained on the as-grown sample is shown at $w = 300\,\mu\text{m}$). We observe a pronounced quench of the free exciton diffusion length in the narrow stripes.

Since the exciton diffusivity D is independent of the sample geometry, the collapse of the diffusion length $L = \sqrt{D\tau}$ must be caused by a drop of the exciton lifetime τ. This effect has independently been observed in time-resolved photoluminescence studies on etched wire structures of single quantum well samples. The authors of Refs. [154, 155] observe a decrease of the exciton lifetime for decreasing wire widths, which is attributed to surface recombination at the etched wire sidewalls as a parallel nonradiative decay channel. Expectedly, the parasitic surface recombination is only operational in wires which are relatively narrow compared with the exciton diffusion length.

The reduction of the effective lifetime by exciton diffusion to the channel sidewalls is consistently reproduced by the choice of boundary conditions at the open wire surfaces. Replacing the previously assumed zero-flux boundary condition with $D\frac{\partial}{\partial y}n(x,y) = -Sn(x,y)$ at the lateral wire surfaces leads to the following set of equations [154]

$$\tau_{\text{eff}}^{-1} = \tau_0^{-1} + \tau_{\text{geo}}^{-1} \tag{7.8a}$$

$$\tau_{\text{geo}} = w^2/(4\beta^2 D) \tag{7.8b}$$

$$\beta \tan\beta = wS/(2D). \tag{7.8c}$$

Here, τ_0 is the exciton lifetime in the as-grown sample, τ_{eff} is the effective exciton lifetime in the etched wire structures, and S is the surface recombination velocity.

For $D = 371\,\text{cm}^2\,\text{s}^{-1}$ and $\tau_0 = 3\,\text{ns}$, [52] eqs. (7.8a)-(7.8c) yield τ_{eff} for a given sample geometry. From this effective lifetime, we calculate the expected diffusion length $L = \sqrt{D\tau_{\text{eff}}}$ as a function of the wire width w. Best agreement with experiment [red curve in Fig. 30 (e)] is obtained for a surface recombination velocity of

$S = 1.3\,\mu\mathrm{m\,ns}^{-1}$. This value is in good agreement with GaAs surface recombination velocities reported in the literature [154].

We regard the perfect agreement with experiment as convincing evidence that the collapse of the diffusion length in the etched GaAs wire structures is caused by the diffusion of free excitons to the channel sidewalls, which facilitate nonradiative surface recombination.

7.5 Summary and conclusion

We have investigated the diffusion of free excitons in a nearly defect-free GaAs sample using the SRPL technique. In distinction from previous studies of the (FX) zero-phonon line, we have used the emission intensity of the extremely weak free exciton second LO-phonon replica as a tracer for the local exciton density. The replica monitors the entire free exciton ensemble and allows us to bypass the immanent interpretation ambiguities of the (FX) zero-phonon line.

Our analysis yields the important result that undistorted diffusion profiles are only observed under strictly resonant optical excitation. Because of the high excitation density at the pump spot, slightly off-resonant optical excitation already causes a localized hot spot in the carrier system, which results in severe distortions of the free exciton diffusion profiles. Such local heating is inherent to virtually all spatially resolved spectroscopy techniques involving focused laser excitation and low sample temperatures. Resonant optical excitation is thus crucial for the reliable determination of photocarrier diffusion coefficients from SRPL spectroscopy, a fact which has not been considered in most previous studies reported in the literature.

Using resonant optical excitation, we have investigated the transformation of the undistorted stationary exciton diffusion profiles in etched GaAs wire structures. We have observed a dimensional crossover when the wire width falls below the exciton diffusion length. In the limiting cases of extremely wide (narrow) wires, the experimental exciton diffusion profiles are expectedly reproduced by the analytical solutions of the two-dimensional (one-dimensional) photocarrier diffusion equation. The observed drop of the diffusion length in the narrow structures has been shown to originate from a collapse of the exciton lifetime, which is caused by parasitic surface recombination of free excitons diffusing to the etched wire sidewalls.

Chapter 8

Bound exciton ring formation

Photocarrier excitation and excess energy relaxation, exciton formation, the related exciton electron-hole plasma (EHP) interconversion, and radiative recombination are cornerstones of semiconductor optical spectroscopy that have been investigated intensively for decades [85]. We have presented our time-domain studies on a subset of these subjects, i.e., the interplay of exciton cooling and radiative recombination, in part II of this thesis.

A particular wealth of interesting new phenomena arises when optical excitation by a focused laser is combined with spatially resolved photoluminescence (SRPL) detection to obtain insight into photocarrier transport processes. The intricate interplay of the above processes and, additionally, the spatial diffusion of the different carrier species renders the experimentally observed luminescence patterns often nontrivial. An example of such nontrivial SRPL patterns that currently attract particularly strong interest is luminescence rings from indirect excitons in coupled quantum wells (CQWs), which are studied intensively in the search for excitonic Bose-Einstein condensation (BEC).

The first observation of such macroscopic concentric PL rings from indirect excitons in electrically gated CQWs [13, 14] has initiated a series of insightful SRPL studies on these structures. Typically, two concentric PL rings emerge around a tightly focused laser excitation spot. While the periodic fragmentation of the outer ring seen at low lattice temperatures is speculated to hint towards a macroscopically ordered phase of the excitons [14, 18, 156], the very fact of inner and outer ring formation has found simpler explanations. The outer ring was shown to originate from a spatial separation of the electron and hole plasmas in their respective quantum well planes [18, 19]. The inner halo results from a temperature gradient within the exciton gas [14, 21]. Surprisingly, for SRPL measurements on bulk semiconductors, excitonic ring formation due to a localized overheating of the exciton system with respect to the lattice has not been reported yet.

We show in this chapter that a temperature effect conceptually similar to the inner

ring formation in indirect CQWs emerges in SRPL spectra of ultrapure bulk GaAs. At moderate excitation densities we observe butterfly-shaped luminescence images in the wavelength-radial distance-plane with a pronounced quench of the bound exciton PL intensity at the pump spot. From the characteristic dependence of the SRPL profiles on excitation wavelength, excitation density, and lattice temperature, we conclude that the luminescence quench is due to a localized overheating of the exciton population caused by nonresonant laser excitation.

We present a conceptual model based on a temperature gradient in the exciton system, which quantitatively reproduces the experimental SRPL patterns. The model allows us to trace the influence of excitation excess energy on the spatially dependent exciton energy relaxation and provides access to the exciton temperature profile. Our analysis reveals temperature gradients in the exciton system persisting over distances $\geq 10\,\mu\text{m}$, which exceed the size of the pump spot by an order of magnitude.

8.1 Dependence of the ring formation on optical excitation parameters

All data presented in this chapter are obtained on a $70\,\mu\text{m}$ thick epilayer of unintentionally *n*-doped GaAs (sample A). The photoluminescence spectrum of the investigated sample and the assignment of free and bound exciton transitions have previously been discussed in section 4.1 (cf. Fig. 16). In this chapter, we are mainly concerned with excitons localized at neutral and ionized shallow donors, i.e., the (D^0,X) and (D^+,X) transitions.

We show in Fig. 32 a compilation of spatially resolved photoluminescence images obtained under focused laser excitation at different excitation conditions. Horizontal line cuts through the color-coded SRPL images yield PL spectra at a fixed distance from the pump spot. Likewise, vertical line cuts reveal spatial PL profiles at a given detection wavelength, i.e., on a particular PL transition.

First of all, we note that the spatial extent of the PL signal exceeds the size of the laser excitation spot by an order of magnitude. In the previous chapter, we have investigated the diffusion of free excitons in another high-purity GaAs sample (sample B) and found an exceptionally high exciton diffusivity of $D \approx 370\,\text{cm}^2\,\text{s}^{-1}$. The transport of excitons far from the excitation spot seen in Fig. 32 indicates a comparably high exciton diffusivity in sample A.

The shape of the SRPL images shows a delicate dependence on excitation wavelength and pump power. Figures 32 (a) - 32 (c) demonstrate the transformation of the PL images as a function of the pump power P_{exc} at a fixed excitation wavelength of $\lambda_{\text{exc}} = 7850\,\text{Å}$. At low excitation density, the spatial PL profiles are bell-shaped on all free and bound exciton transitions. Upon increasing P_{exc}, the PL profiles flatten. At large excitation densities, a characteristic butterfly-shape of the SRPL images appears

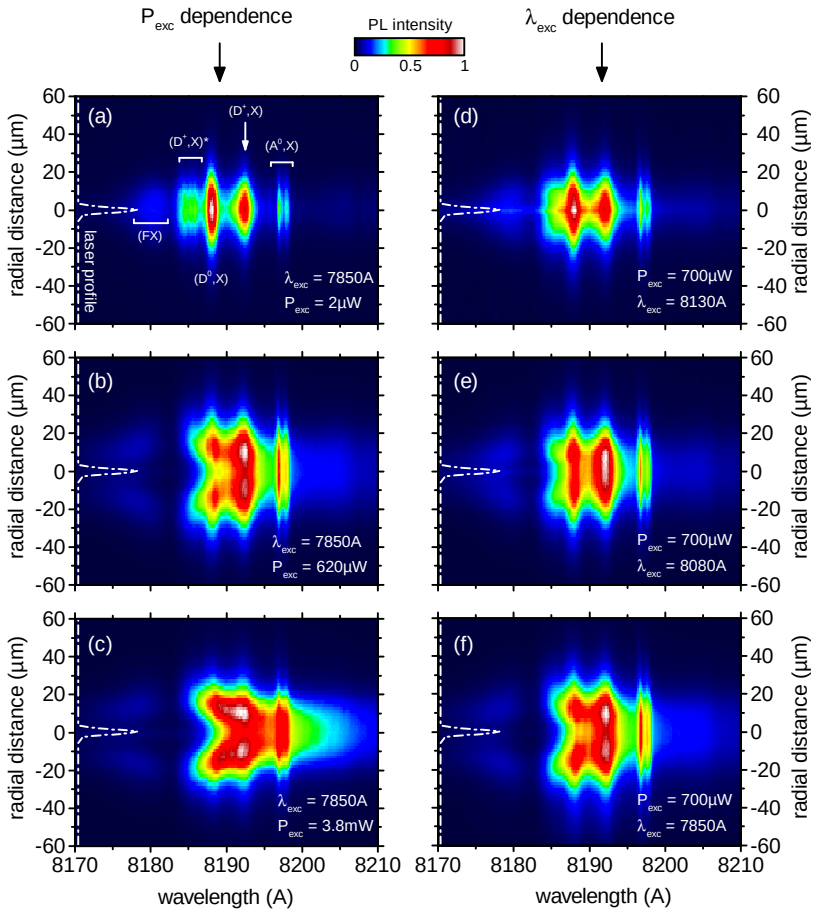

Figure 32: Representative SRPL images obtained on sample A at different excitation conditions. Dashed white lines indicate the spatial extent of the laser excitation source. (a-c) At fixed excitation wavelength $\lambda_{\mathrm{exc}} = 7850\,\text{Å}$, the SRPL images are bell-shaped at low excitation power. Upon increasing P_{exc}, the characteristic butterfly-shaped images appear in the wavelength-radial distance plane, which exhibit a pronounced quench of the bound exciton PL intensity at the excitation center. (d-f) Transformation of the SRPL images as a function of excitation wavelength at fixed excitation power $P_{\mathrm{exc}} = 700\,\mu\text{W}$. No PL quench is observed at near-resonant optical excitation. Butterfly-shaped SRPL images only appear when λ_{exc} is tuned towards shorter wavelengths, i.e., higher excess energies.

in the wavelength-radial distance plane with a pronounced quench of the PL intensity around the excitation center.

At a fixed excitation power, a similar transformation of the SRPL images is observed as a function of the excitation wavelength [Figs. 32 (d) - 32 (f)]. Near-band gap optical excitation ($\lambda_{\mathrm{exc}} = 8130\,\text{Å}$) results in bell-shaped spatial PL profiles. As the excitation wavelength is tuned to larger excess energies (i.e., shorter excitation wavelengths), a dimple appears at the photoexcitation spot, which progressively develops into a pronounced quench of the PL emission intensity at the excitation center.

Noteworthy, the luminescence quench at the pump spot disappears at elevated sample temperatures $T_L \gtrsim 12\,\mathrm{K}$ (not shown here).

The distinctive excitation wavelength dependence of the SRPL images unambiguously rules out lattice heating and exciton screening as possible explanations for the local luminescence quench. Both mechanisms should be independent of the excitation excess energy. Instead, the dependence on pump power, excitation wavelength, and lattice temperature is characteristic of heating effects in the photocarrier system (cf. our discussion in section 2.5.3). We, therefore, conclude that the PL quench at the excitation center is due to an overheating of the exciton ensemble caused by nonresonant optical excitation.

8.2 Model description of the PL quench

We now present a conceptual model which reproduces all features of the SRPL images for the whole set of excitation wavelengths and optical pump powers. Moreover, the model provides access to the spatially resolved excess energy relaxation of excitons in bulk GaAs and allows for the quantitative determination of the peak exciton temperature $T_X(r=0)$ at the center of optical excitation.

Our model assumes the following physical picture: hot excitons are locally generated by the focused laser spot. The photoexcited excitons diffuse away from the excitation volume, meanwhile relaxing their excess energy by emission of phonons and scattering with lower energy excitons and charge carriers [85]. A steady-state situation builds up with a radially symmetric exciton density profile $n_X(r)$. The incomplete excess energy relaxation of the optically excited excitons results in a radially symmetric spatial temperature profile $T_X(r)$ in the exciton cloud.

We describe the emitted PL intensity at each distance r from the excitation spot by the product:

$$I(r) \propto n_X(r) \times \xi[T_X(r)] \tag{8.1}$$

with the local free exciton density $n_X(r)$ and a temperature dependent occupation factor $\xi[T_X(r)]$. The latter depends on the local exciton temperature $T_X(r)$ and is specific to each bound exciton recombination path. All three model components $n_X(r)$, $T_X(r)$, and the occupation factors ξ are summarized and illustrated in Fig. 33.

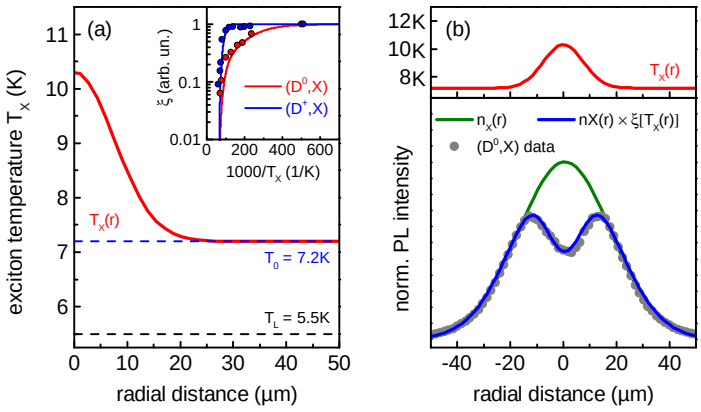

Figure 33: Summary of the model inputs. (a) Model assumption for a localized overheating of the exciton ensemble near the photoexcitation spot. Deviation of the base temperature T_0 from the lattice temperature T_L is a result of incomplete excess energy relaxation and recombination heating. The inset shows data points from Ref. [115] together with Arrhenius-type fits assuming two activation energies of 7 and 1 meV. (b) Exemplary illustration of the analysis procedure: The exciton density profile $n_X(r)$ is adjusted to the outer wings of the measured (D^0,X) PL profiles, assuming that the bound exciton PL intensity monitors the exciton density $n_X(r)$ outside the overheating region. Fitting $\xi\,[T_X(r)] \times n_X(r)$ to the data yields estimates for the width and the amplitude of the pump-induced overheating in the carrier system. A distinct PL quench only emerges when $n_X(r)$ is broader than $T_X(r)$.

Free exciton density profile The diffusion of photoexcited free excitons away from the excitation spot results in a radially symmetric free exciton density profile $n_X(r)$. The profile $n_X(r)$ is in principle given by the solution to the stationary diffusion equation [142]

$$\nabla_r \cdot [D\,\nabla_r\, n_X(r)] - \frac{n_X(r)}{\tau} + g(r) = 0 \tag{8.2}$$

where D is the exciton diffusion coefficient, τ is the free exciton ensemble lifetime and $g(r)$ is the exciton generation rate due to the focused laser spot. There is, however, no analytical solution to eq. (8.2) for the given sample geometry, i.e., a three-dimensional half space. Moreover, a temperature gradient in the exciton system caused by non-resonant optical excitation renders the diffusion coefficient $D \to D[T_X(r)]$ spatially dependent, which impedes a robust prediction of the eventual exciton density profile $n_X(r)$ (cf. our discussion in section 7.3).

As a first approximation to $n_X(r)$ in our model, we assume a Gaussian shaped exciton diffusion profile.[25] Recalling that only free excitons with wave vectors $K \approx 0$

[25] Inspection of Fig. 29 demonstrates that a Gaussian profile is actually a reasonable approximation for $n_X(r)$ in the case of a moderate overheating $\lesssim 13\,\mathrm{K}$ in the exciton system. At larger peak photocarrier temperatures $\gtrsim 15\,\mathrm{K}$, thermal breakup of excitons into unbound electron-hole pairs gives rise to the *free*

recombine radiatively [52, 54, 55], the spatially resolved (FX) intensity may not be taken as a direct measure for $n_X(r)$. We rather estimate the spatial extent of the exciton density profile $n_X(r)$ by the following procedure [cf. Fig. 33 (b)]. Gaussian envelopes are fitted to the outer wings of the measured (D^0,X) luminescence profiles, assuming that the bound exciton PL intensity is proportional to n_X outside the overheating region.

We note that this approach is only valid if the donor density n_D exceeds the peak free exciton density $n_X(r=0)$. In fact, our data unambiguously demonstrates that the relation $n_D \geq n_X(r=0)$ holds. As we tune the excitation wavelength towards the GaAs band gap, the PL quench at the excitation center disappears and we observe bell-shaped (D^0,X) PL profiles at all excitation densities. Even at the highest pump power, no flattening of the (D^0,X) profiles is seen. This rules out any artificial distortion of the approximated $n_X(r)$ profiles due to a local saturation of the residual donors.

Occupation factor ξ We now consider the occupation factor $\xi\,[T_X(r)]$, which is a characteristic property of each bound exciton complex. For the analysis presented in this chapter, we restrict ourselves to the recombination of excitons localized at neutral and ionized donor sites for which reliable information on $\xi(T)$ is available in the literature. The emission intensities of the (D^0,X) and (D^+,X) lines are studied in detail in Ref. [115] as a function of the lattice temperature T_L. The authors find a pronounced quenching of the PL intensity for elevated sample temperatures with two characteristic dissociation energies of 7 meV and 1 meV. Data points from Ref. [115] are shown in the inset of Fig. 33 (a) as red and blue markers. We interpret these PL intensity quenches as temperature dependent localization probabilities of free excitons at the respective donor sites. We conclude that the temperature relevant to this process is, therefore, not that of the lattice, but the exciton temperature T_X. We take the empirical expressions for the quenching behavior with the activation energies provided in Ref. [115] as an approximation for the occupation factors $\xi\,[T_X(r)]$ in our model. The fitting curves are shown as red and blue lines in the inset of Fig. 33 (a).

Exciton temperature profile We next consider the exciton temperature profile $T_X(r)$. In principle, T_X can be obtained from a Maxwellian line shape analysis of the second LO-phonon replica of the free exciton transition [7, 8] (section 2.3). However, the extremely weak emission intensity of the $(FX)-2\hbar\Omega_{\mathrm{LO}}$ replica in the here investigated sample does not allow for a spatially resolved line shape analysis of that transition. As a first approximation for $T_X(r)$, we assume a Gaussian shaped overheating of the

exciton ring formation effect with a pronounced quench of the exciton density in the hot spot region (chapter 9). The results of our conceptual model presented in Fig. 35 will show that the peak exciton temperatures in sample A are indeed $\lesssim 12\,\mathrm{K}$, which *a posteriori* justifies our assumption of a Gaussian exciton density profile.

exciton ensemble peaked at the center of optical excitation.[26] The width and peak amplitude of $T_X(r)$ are determined by fitting our model to the experimental PL profiles as discussed in the following section 8.3.

The base exciton temperature T_0 far away from the excitation spot is not set to the lattice temperature T_L as one might expect at first, but to the respective value obtained from a Maxwellian line shape analysis of the $(FX)-2\hbar\Omega_{\mathrm{LO}}$ replica measured under defocused illumination in the low-excitation limit [cf. Fig. 33 (a)]. The deviation of T_0 from T_L occurs because nonresonantly excited excitons cannot fully relax their excess energy and thermalize with the crystal lattice on the time scale of their radiative lifetime. Furthermore, the recombination heating effect discussed in section 5.3 also prevents full equilibration of the exciton ensemble with the crystal lattice [139, 140]. For our model description, the base temperature T_0 far from the center of excitation is individually determined for each excitation wavelength λ_{exc}.

8.3 Comparison with experiment

Having discussed the meaning and approximations of all model components, we now turn to the determination of the two remaining free parameters, i.e., the width and the amplitude of the exciton temperature profile $T_X(r)$.

We first consider the width of the $T_X(r)$ profile. From a fit of our model [eq. (8.1)] to the measured (D^0,X) profile at 7730 Å excitation wavelength, we obtain a peak exciton temperature of 10.4 K at the pump spot and a $(1/e)$ full width of the Gaussian $T_X(r)$ profile of 21 µm. Only the amplitude of the overheating (and the base temperature T_0) should depend on λ_{exc}, but not the width of the temperature profile. We, therefore, keep the width of the $T_X(r)$ profile fixed at 21 µm for all other excitation wavelengths. Since T_0 is individually determined for each λ_{exc} as described above, the overheating amplitude remains the *only* variable model parameter.

A comparison of our model description with the experimental PL profiles detected on the (D^0,X) and (D^+,X) transitions is displayed in Fig. 34. Our model reproduces all details of the (D^0,X) PL profiles for the whole set of excitation wavelengths [Fig. 34 (a)] and for all pump powers [Fig. 34 (c)] *by only adjusting the overheating amplitude*. Moreover, with the expression for the (D^+,X) occupation factor from the literature and the exact same temperature profile $T_X(r)$ as for the model description of the (D^0,X) line, we also find very good agreement of our model prediction with the measured (D^+,X) profiles for the whole set of excitation wavelengths [Fig. 34 (b)].

We emphasize again that once $T_X(r)$ is fixed from the analysis of the (D^0,X) profiles, no free parameter is left to adjust the (D^+,X) model prediction to the experimental

[26] We note that the shape of the experimental $T_X(r)$ profile in sample B, which in contrast to the here investigated sample A allows for a spatially resolved line shape analysis of the $(FX)-2\hbar\Omega_{\mathrm{LO}}$ replica, is indeed well described by a Gaussian overheating (cf. Figs. 29 and 39).

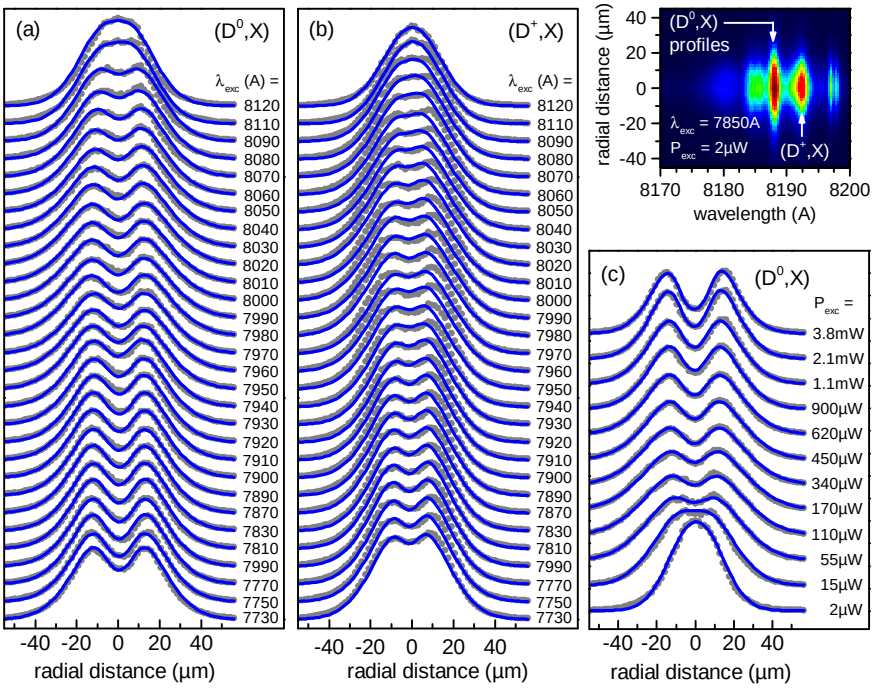

Figure 34: (a,b) Spatially resolved PL profiles of excitons recombining at neutral (D^0,X) and ionized donor sites (D^+,X) for different excitation wavelengths at fixed $P_{\rm exc} = 700\,\mu$W. (c) Transformation of the (D^0,X) SRPL profiles as a function of pump power at fixed $\lambda_{\rm exc} = 7850\,$Å. Our model (solid blue lines) reproduces all details of the experimental data and allows to determine the exciton temperature at the excitation center from the depth of the PL quench. Extracted values for T_X at the center of excitation are displayed in Fig. 35 as a function of excitation wavelength and optical pump power.

data. We regard the very good agreement for the whole set of excitation wavelengths as strong evidence that our model captures the essential physics underlying the bound exciton ring formation.

The agreement of our model prediction for the (D^+,X) SRPL profiles with experiment furthermore confirms our previous interpretation that the main contribution to the 8192 Å line in the photoluminescence spectrum of sample A [Fig. 16 (a)] is due to the recombination of excitons localized at ionized donor sites.

8.4 Excess energy relaxation of photoexcited excitons

The results of our model analysis are summarized in Fig. 35. Here we show the peak exciton temperature $T_X(r=0)$ (i.e., the only variable model parameter) obtained from the fitting routine discussed in the previous section. Figure 35 (a) demonstrates

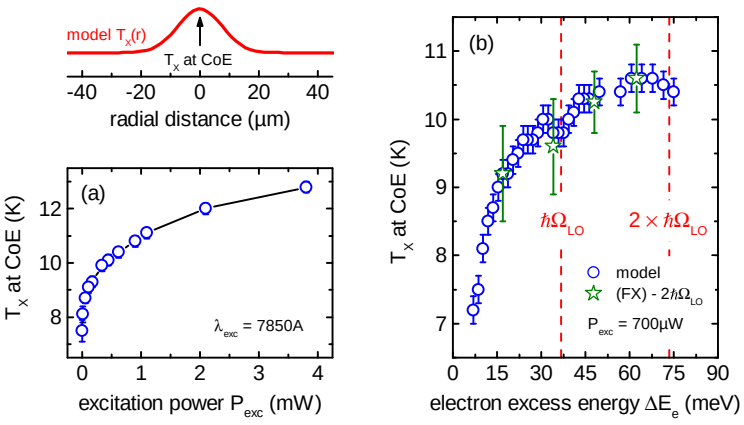

Figure 35: Exciton temperature $T_X(r=0)$ at the center of excitation (CoE) obtained from our model analysis as a function of (a) pump power and (b) electron excess energy. The sublinear progression of T_X as a function of the excitation density and its distinct excess energy dependence are characteristic of heating effects in the photocarrier system. The dip in the $T_X(\Delta E_e)$ curve at 36.8 meV indicates that integral multiples of $\hbar\Omega_{\mathrm{LO}}$ excess energy are efficiently relaxed to the crystal lattice by rapid LO phonon emission. Green markers indicate T_X values obtained from an independent line shape analysis of the $(FX)-2\hbar\Omega_{\mathrm{LO}}$ replica.

a sublinear increase of the peak exciton temperature as a function of the excitation density. This qualitative behavior is characteristic of photocarrier heating effects [108] (cf. our discussion in section 2.5.3) and corroborates our interpretation that the PL quench is due to a localized overheating in the exciton ensemble.

The even more striking evidence for the conceptual correctness of our analysis, however, is the dependence of $T_X(r=0)$ on the excitation wavelength. We display in Fig. 35 (b) the peak exciton temperature as a function of the electron excess energy [105]

$$\Delta E_e = (E_{\mathrm{Ph}} - E_g) \times (1 + m_e/m_{hh})^{-1} \tag{8.3}$$

which shows a very characteristic behavior. T_X increases for decreasing excitation wavelengths λ_{exc}, i.e., increasing photon energies E_{Ph}. The effective temperature of the carrier ensemble increases as more excess energy ΔE_e per photoexcited electron is deposited in the system. A deviation from this monotonic trend occurs when the excess energy coincides with the GaAs LO phonon energy $\hbar\Omega_{\mathrm{LO}} = 36.8\,\mathrm{meV}$ [37]. The dip in the $T_X(\Delta E_e)$ curve at 36.8 meV demonstrates that integral multiples of $\hbar\Omega_{\mathrm{LO}}$ electron excess energy are efficiently relaxed to the crystal lattice by rapid LO phonon emission. The LO phonon cascade emission proceeds on a faster time scale than the subsequent exciton formation and hence manifests at 36.8 meV *electron* excess energy. The replication of the dip at $\Delta E_e = 2 \times \hbar\Omega_{\mathrm{LO}}$ is not fully resolved because of the limited tuning range of our pump laser. We note, however, that the signature of

the LO phonon cascade is most characteristic of heating effects in the photocarrier system [105]. We thus regard the observed $T_X(\Delta E_e)$ progression in Fig. 35 (b) as strong evidence that a localized overheating of the exciton system is responsible for the PL quench at the pump spot and that our model successfully captures the underlying physics of the bound exciton ring formation.

We previously noted that the extremely weak emission intensity of the free exciton second LO-phonon replica is a major obstacle for a spatially resolved line shape analysis in this particular sample, rendering a direct determination of the $T_X(r)$ profile unfeasible. Only at the center of optical excitation, sufficient PL intensity is detected, such that we can here perform the Maxwellian line shape analysis of the $(FX)-2\hbar\Omega_{\mathrm{LO}}$ transition to obtain $T_X(r=0)$. We show in Fig. 35 (b) by green markers the independently determined values of the peak exciton temperature at representative excitation excess energies.[27] Despite the relatively large error bars, the exciton temperatures obtained from this independent line shape analysis of the $(FX)-2\hbar\Omega_{\mathrm{LO}}$ replica coincide *quantitatively* with the peak exciton temperatures $T_X(r=0)$ of our model analysis.

In addition to probing the exciton temperature at the excitation center, our model also reveals the length scale of excess energy relaxation of optically excited excitons in high-purity bulk GaAs. We find that the slow time scale for the residual excess energy relaxation by acoustic phonon emission [54] results in the buildup of significant exciton temperature gradients, which persist over macroscopic length scales. From the width of the $T_X(r)$ profile, our model analysis demonstrates that the local overheating of the excitons persists over $\geq 10\,\mu\mathrm{m}$, which exceeds the spatial extent of the pump spot by an order of magnitude. Moreover, even far from the excitation spot, full thermalization with the crystal lattice is not reached due to the competing time scales of energy relaxation and radiative recombination and because of the recombination heating effect.

8.5 Concluding remarks

We conclude by noting that heating effects due to insufficient excess energy relaxation of optically excited excitons are inevitable in all low-temperature experiments involving non-resonant optical excitation. However, the clear direct manifestation of the exciton overheating as butterfly-shaped SRPL images with a bound exciton luminescence quench at the pump spot is only observed in nearly defect-free bulk samples that exhibit high carrier mobilities. Only then does the exceptionally long diffusion length

[27] We note that in sample A, the second LO-phonon replica is not perfectly isolated in the PL spectrum. Nearby defect-related transitions [i.e., the one LO-phonon replicas of the spectrally nearby $(e,A^0)_C$ and $(D^0,A^0)_C$ lines] cause a broad spurious PL background which cannot be exactly quantified. The assumption which we make for this background introduces a significant uncertainty in the determined temperature. Noteworthy, this spurious PL background is less pronounced under defocused weak optical excitation. The previous determination of the base temperature T_0 is, therefore, significantly more precise.

$L = \sqrt{D\tau}$ (cf. section 7.2) lead to $n_X(r)$ profiles which are wider than the $T_X(r)$ distribution. In the framework of the presented model, this condition is required for the bound exciton ring formation.

We have verified the applicability of our model to other high-purity GaAs samples. We found qualitatively similar results for unintentionally p-doped reference samples of LPE grown bulk GaAs and ultrapure molecular beam epitaxy (MBE) grown GaAs epilayers. In some samples, even larger peak temperatures up to 20 K were observed. Such significant overheating amplitudes compared with the relatively low peak exciton temperatures in the here investigated sample potentially cause a localized quench of the exciton density $n_X(r)$ itself.

This scenario mandates independent treatment since our model description of the bound exciton ring formation relies on the assumption of a Gaussian exciton density profile $n_X(r)$. The *free exciton ring formation* is, therefore, individually addressed in the following chapter.

Chapter 9

Free exciton ring formation

In the previous chapter, we have investigated the bound exciton ring formation in a high-purity bulk GaAs sample. This effect manifests in spatially resolved photoluminescence (SRPL) images obtained under focused laser excitation as a quench of the bound exciton PL intensity around the pump spot. We have shown that this ring formation results from a local hot spot in the exciton system caused by nonresonant optical excitation, which prevents the binding of free excitons to residual impurities. Noteworthy, a Gaussian-shaped exciton density profile was reasonably assumed because of the relatively small peak exciton temperatures in the investigated sample (sample A).

In the present chapter, we report on the observation of macroscopic *free exciton photoluminescence rings* that occur in the SRPL images obtained on a nearly defect-free GaAs epilayer (sample B) at low lattice temperatures. Such macroscopic PL rings, which have previously been observed in SRPL experiments on electrically gated coupled quantum well structures [13, 14], have attracted particular research interest during the last decade. The nontrivial SRPL images were initially speculated to hint towards a macroscopically ordered phase of the excitons. Although the very fact of concentric ring formation was shown to result from a pump-induced temperature gradient and a spatial in-plane separation of the electron and hole plasmas [18, 19], the periodic fragmentation of the outer ring structure [18, 30, 156] remains a subject of unbroken research interest.

Conceptually similar to the bound exciton ring formation discussed in the previous chapter, the free exciton ring formation is also caused by pump-induced local heating in the photocarrier system. However, the exciton density itself experiences a pronounced quench in the hot spot region. The free exciton rings are a direct manifestation of local shifts in the thermodynamic equilibrium between Coulomb-bound free excitons and the uncorrelated electron-hole plasma (EHP). Local heating by nonresonant optical excitation quenches the exciton density close to the focused laser spot, where consequently the uncorrelated EHP is thermodynamically favored. Interestingly, an increase in excitation density, which further raises the peak carrier temperature, nevertheless

stabilizes the excitons in the hot spot region.

We quantitatively model the measured SRPL profiles using the Saha equation, which allows us to calculate the local population balance between free excitons and the uncorrelated EHP from the total photocarrier pair density and the exciton temperature profile. The latter is directly obtained from a spatially resolved line shape analysis of the free exciton second LO-phonon replica, which was not available in previous related works on coupled quantum wells.

The free exciton ring formation provides particularly instructive insight into the spatially dependent thermodynamics of the partially ionized exciton gas in a bulk semiconductor. Our analysis thereby naturally extends previous works [133, 138] investigating the thermodynamics of EHP-to-free exciton interconversion in the time domain (see also our discussion in chapter 5).

9.1 Ring formation under continuous-wave optical excitation

Figure 36 provides an illustration of the free exciton ring formation effect. The excitation laser beam is tightly focused on the sample surface, a magnified image of which is projected on the sensor of a CMOS camera (cf. Fig. 12). Color indicates the spatial distribution of the free exciton luminescence, which is obtained by inserting a 8130 Å dielectric long pass filter to block the laser light and to select only the (FX) luminescence.[28] Because of the large exciton diffusion coefficient in the investigated sample (cf. section 7.3), free exciton luminescence is detected at large distances ($\gtrsim 40\,\mu$m) from the excitation spot. More importantly, a pronounced quench of the exciton density at the excitation center causes a macroscopic concentric (FX) PL ring.

In a typical SRPL experiment, nonresonant optical excitation creates an ensemble of initially hot charge carriers and excitons, whose excess energy relaxation proceeds by emission of optical and acoustic phonons [6, 54, 99]. The limited cooling efficiency by acoustic phonon coupling and the additional recombination heating effect [139, 140] typically impede full thermalization of the photocarrier population with the crystal lattice. Under focused laser excitation, the incomplete excess energy dissipation then causes the buildup of temperature gradients in the photocarrier system, which potentially persist over macroscopic distances [104, 141] (cf. section 8.4). We show in the following that the free exciton ring formation effect results from such a localized overheating of the photocarrier system at the pump spot.

To support our interpretation that local heating is the mechanism underlying the free

[28] To be precise, this method detects the whole luminescence spectrum including bound exciton and defect-related transitions. Because of the dominance of the (FX) line in the low-temperature PL spectrum of sample B (cf. Fig. 17), the spectrally integrated PL intensity monitors in good approximation the local free exciton luminescence intensity.

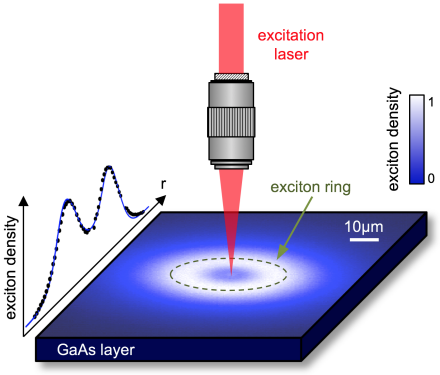

Figure 36: Free exciton ring formation under continuous-wave optical excitation. A magnified image of the sample surface is projected on the CMOS camera chip (cf. Fig. 12) to visualize the ring formation effect in real-space. Free exciton luminescence is detected by inserting a suitable long pass filter. The ring formation manifests as a pronounced quench of the (FX) photoluminescence intensity around the pump spot. The lattice temperature is $T_L = 5\,\mathrm{K}$, optical excitation parameters are $P_{\mathrm{exc}} = 20\,\mu\mathrm{W}$ and $\lambda_{\mathrm{exc}} = 8050\,\text{Å}$.

exciton ring formation, we first discuss the qualitative dependence of the PL quench on various experimental parameters. We show in Fig. 37 a compilation of SRPL images obtained under focused laser excitation for representative sample temperatures T_L, excitation wavelengths λ_{exc}, and pump powers P_{exc}. Ring formation is only observed under such excitation conditions that favor the buildup of a spatial temperature gradient in the sample:

1. The ring formation exhibits a distinct dependence on the excitation wavelength λ_{exc} (first column of SRPL images in Fig. 37): the peak-to-valley ratio of the PL quench at the excitation center increases for increasing photon energies (decreasing λ_{exc}). Under near-resonant optical excitation ($\lambda_{\mathrm{exc}} = 8130\,\text{Å}$), i.e., when photocarriers are excited with only small amounts of excess energy, the ring formation effect disappears.

2. The excitation density dependence of the ring formation effect is reported in the second column in Fig. 37. At fixed nonresonant $\lambda_{\mathrm{exc}} = 8050\,\text{Å}$ and moderate pump powers, the PL quench increases monotonically with P_{exc} and disappears in the low-excitation limit.[29]

3. Furthermore, the ring formation is most pronounced at low sample temperatures. For $T_L \gtrsim 25\,\mathrm{K}$, the cooling rate of the initially hot photocarrier ensemble increases drastically due to the availability of rapid LO phonon emission as an

[29] The reverse trend observed in the high-excitation limit, i.e., the stabilization of the excitons with increasing P_{exc} [Figs. 39 (d) - 39 (f)], will be discussed in section 9.3.

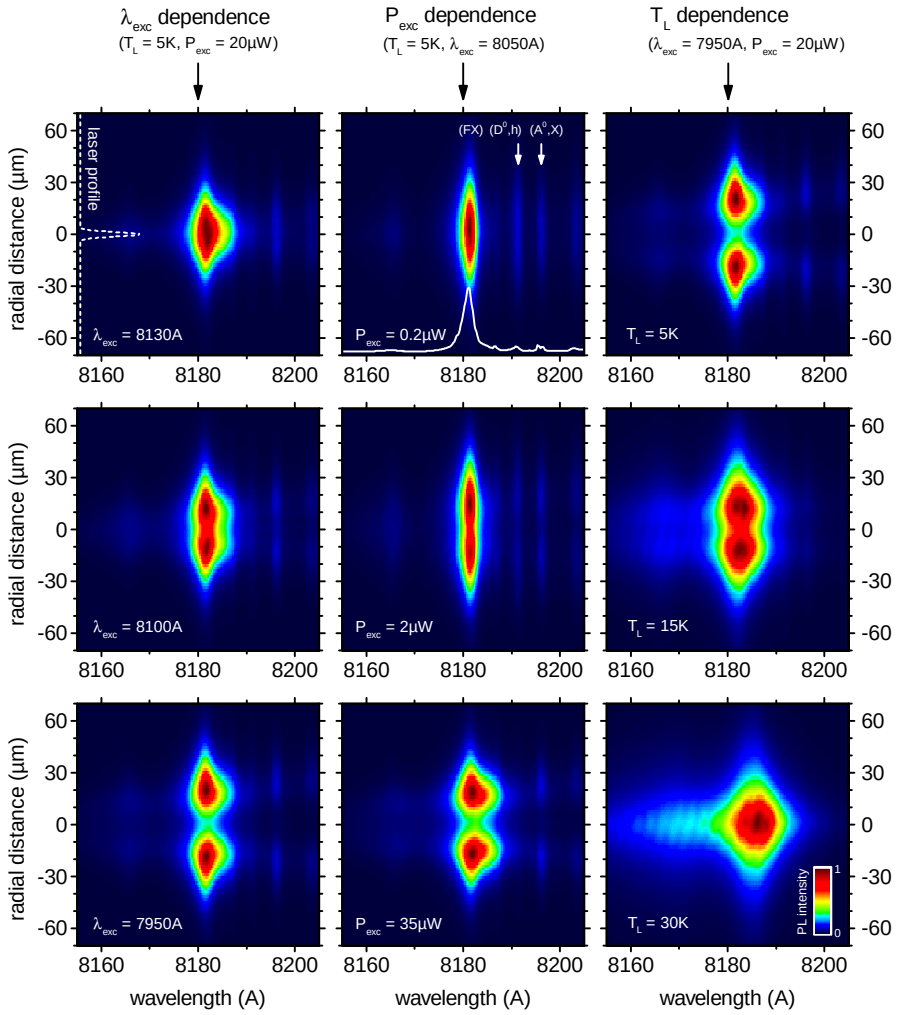

Figure 37: Compilation of SRPL images revealing the dependence of the free exciton ring formation on various experimental parameters. Ring formation only occurs for such excitation conditions that favor the buildup of a spatial temperature gradient in the photocarrier system, i.e., low lattice temperatures, high excitation densities, and nonresonant optical excitation. In each column of SRPL images, only one parameter (indicated by the white text label) is varied while the other two parameters are kept fixed. Left column: Ring formation is absent at near-resonant optical excitation. The depth of the PL quench at the excitation center increases with increasing excitation excess energies (decreasing excitation wavelength λ_{exc}). Middle column: Ring formation is more pronounced at higher excitation densities. Right column: Sample temperature dependence of the SRPL images. At $T_L \gtrsim 30\,\mathrm{K}$, the temperature gradient in the exciton system vanishes and hence no ring formation is observed. The spatial extent of the excitation spot is the same for all measurements and is exemplarily indicated in the first panel by the dashed profile. We also show a representative low-power PL spectrum of the high-purity GaAs epilayer. Text labels indicate the usual assignment of free and bound exciton transitions [34].

efficient channel of excess energy dissipation [6, 99] (Fig. 10). Irrespective of excitation wavelength and pump power, the carrier system is in thermal equilibrium with the crystal lattice at these sample temperatures and consistently no ring formation is observed at $T_L = 30\,\mathrm{K}$.

The unique dependence on excitation power, excitation wavelength, and lattice temperature is characteristic of heating effects in the photocarrier system [6, 85, 108] (cf. our discussion in section 2.5.3). We, therefore, conclude that the free exciton ring formation is caused by local heating of the exciton population in the vicinity of the laser excitation spot.

We have previously used the Saha equation to analyze the time-resolved buildup of a free exciton population in terms of the electron-hole plasma-to-free exciton interconversion (chapter 5). It is also the Saha equation that governs the spatially dependent population balance between free excitons and the uncorrelated EHP and which translates the exciton temperature gradient into a localized quench of the exciton density in the hot spot region. We present in the following section a model that quantitatively reproduces the dependence of the spatial $n_X(r)$ profile on the discussed excitation parameters.

9.2 Model description

We first recall the two general trends that characterize the thermodynamics of the partially ionized exciton gas in a bulk semiconductor [section 2.4, cf. Fig. 40 (b)]. Thermal breakup of Coulomb-bound excitons at increased temperatures T_X shifts the population balance towards the uncorrelated EHP. At fixed T_X, an increase of the total photocarrier pair density n_0, however, leads to a relative increase of the free exciton population. The spatially dependent thermodynamic population balance between free excitons and the EHP is thus not only influenced by the exciton temperature, but also by the photocarrier pair density profile. Both $T_X(r)$ and $n_0(r)$ have to be determined individually as the input parameters for our model description. The Saha equation then provides the link between $T_X(r)$ and $n_0(r)$, allowing us to compute the local free exciton density $n_X(r)$.

Our model description based on the spatially varying ionization degree of the exciton gas assumes the following physical picture. Under nonresonant focused laser excitation, lateral photocarrier diffusion[30] leads to the formation of a radially symmetric photocarrier pair density profile $n_0(r)$ and to the buildup of a spatial temperature gradient $T_X(r)$. At each distance r from the excitation spot, the local free exciton

[30] Because of the large exciton diffusion coefficient $D \approx 370\,\mathrm{cm}^2\,\mathrm{s}^{-1}$ in our nearly defect-free GaAs sample, the characteristic diffusion length $\sqrt{D\tau}$ significantly exceeds the 1.5 µm thickness of the GaAs epilayer (cf. section 7.3). The photocarrier density and temperature profiles are, therefore, homogeneous along the sample normal, such that diffusion perpendicular to the sample surface can be neglected.

density $n_X(r)$ is given by the product

$$n_X(r) = n_0(r) \times f_X\left[n_0(r), T_X(r)\right] \tag{9.1}$$

where $f_X(n_0, T_X) = n_X/n_0$ is the fraction of free excitons in a photocarrier population of total pair density n_0 given by the Saha equation [eq. (2.17)]. In a ring formation scenario, the missing free excitons at the excitation center are converted into unbound charge carriers by the localized overheating.

Exciton temperature profile We first consider the temperature profile $T_X(r)$. The nontrivial line shape of the free exciton PL transition in a bulk semiconductor [56, 58] impedes the direct determination of the exciton temperature T_X from the free exciton zero-phonon line (FX). The low defect concentration in our sample, however, allows for the detection of the extremely weak second LO-phonon replica of the free exciton transition $(FX) - 2\hbar\Omega_{\mathrm{LO}}$, which reflects the density of occupied states among the thermalized free exciton ensemble [7, 8] (section 2.3). We, therefore, directly obtain the exciton temperature profile $T_X(r)$ from a spatially resolved Maxwellian line shape analysis of the $(FX) - 2\hbar\Omega_{\mathrm{LO}}$ transition.

A representative $T_X(r)$ profile at $P_{\mathrm{exc}} = 30\,\mu\mathrm{W}$ is depicted in Fig. 38 (a). We expectedly observe significant local heating in the exciton system, peaked at the center of optical excitation. Moreover, we find that hot excitons are present for distances which significantly exceed the spatial extent of the pump spot, indicating that heat transport takes place in the carrier system. Even far away from the laser spot ($|r| \gtrsim 40\,\mu\mathrm{m}$) the excitons have not thermalized with the crystal lattice. The increased base temperature of the $T_X(r)$ profiles with respect to T_L is a consequence of the competing time scales of excess energy dissipation and the exciton lifetime and of the recombination heating effect [139, 140] (cf. chapter 8). For all excitation densities P_{exc}, the experimental exciton temperature profile is well described by a Gaussian-shaped overheating.

Pair density profile Because of K vector conservation, only a subset of the entire free exciton population near the Brillouin zone center at $K \approx 0$ can recombine radiatively and contribute to the intensity of the free exciton zero-phonon line [52, 54, 55] (cf. our discussion in section 2.3 and chapter 6). The (FX) SRPL profile is, therefore, not a direct measure for the local free exciton density in the crystal. However, the K vector selection rule that applies to the zero-phonon line is fully relaxed for the radiative recombination of free excitons under simultaneous emission of two LO phonons [7, 8]. Undistorted $n_X(r)$ profiles are hence obtained from the spectrally integrated SRPL intensities of the $(FX) - 2\hbar\Omega_{\mathrm{LO}}$ replica.[31]

[31] For each distance r we determine the intensity of the second LO-phonon replica of the free exciton transition by spectrally integrating the area below the fit curve resulting from the Maxwellian line shape analysis of the local $(FX) - 2\hbar\Omega_{\mathrm{LO}}$ luminescence spectrum.

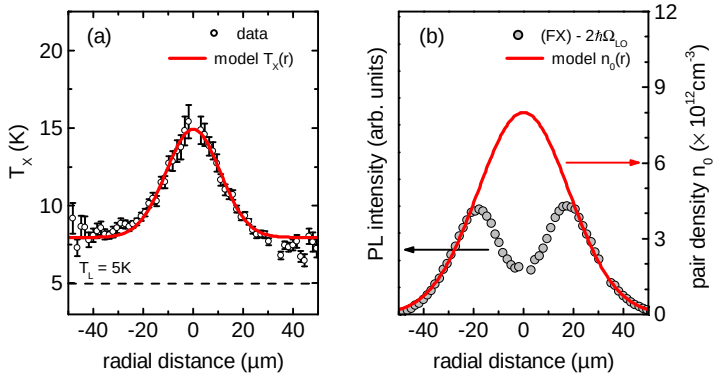

Figure 38: Building blocks of the free exciton ring formation model. (a) The experimental exciton temperature profile is obtained from a spatially resolved Maxwellian line shape analysis of the $(FX)-2\hbar\Omega_{\mathrm{LO}}$ replica. The red curve indicates a Gaussian fit to the data, which serves as the model $T_X(r)$ profile. (b) The integrated photoluminescence intensity of the second LO-phonon replica traces the free exciton density $n_X(r)$, which is nearly $\propto n_0(r)$ outside the overheating region. We obtain our model assumption for $n_0(r)$ from a Gaussian fit to the wings of the experimental $(FX)-2\hbar\Omega_{\mathrm{LO}}$ profile.

We assume in our model a Gaussian profile with 55 µm $(1/e)$ full width as a first approximation for the combined total carrier density diffusion profile $n_0(r)$ [Fig. 38 (b)]. This Gaussian is adjusted to the wings $|r| \gtrsim 25\,\mu\mathrm{m}$ of the $(FX)-2\hbar\Omega_{\mathrm{LO}}$ SRPL profile where the base exciton temperature is reached and where consequently the undistorted $n_0(r)$ is observed. The width of the diffusion profile is assumed to not depend on pump power. The total photocarrier density $n_0(r=0)$ at the center of optical excitation then remains the only variable model parameter.

9.3 Comparison with experiment

A comparison of our model results with experimental exciton density profiles for a range of representative excitation powers P_{exc} is reported in Fig. 39. Excellent agreement of the calculated free exciton density profile $n_X(r)$ with the $(FX)-2\hbar\Omega_{\mathrm{LO}}$ SRPL data is obtained for all excitation densities *by only adjusting the peak photocarrier density* $n_0(r=0)$. This peak density scales linearly with the optical excitation power P_{exc} [Fig. 40 (a)], which we regard as strong evidence that our model captures the essential physics underlying the (FX) ring formation effect.[32]

[32] We note that the degeneracy factors of the involved photocarrier species (electrons, holes, and free excitons) are not precisely known, which aggravates a quantitative comparison of the model $n_0(r=0)$ with the estimated photocarrier densities by considering the exciton lifetime and the diffusion volume. Since the degeneracy factors only rescale $n_0(r=0)$, but do not depend on the excitation parameters, we investigate the more meaningful scaling behavior of the model peak density with the experimental excitation power (cf. section 5.4). A rough estimate, however, suggests a combined degeneracy factor of

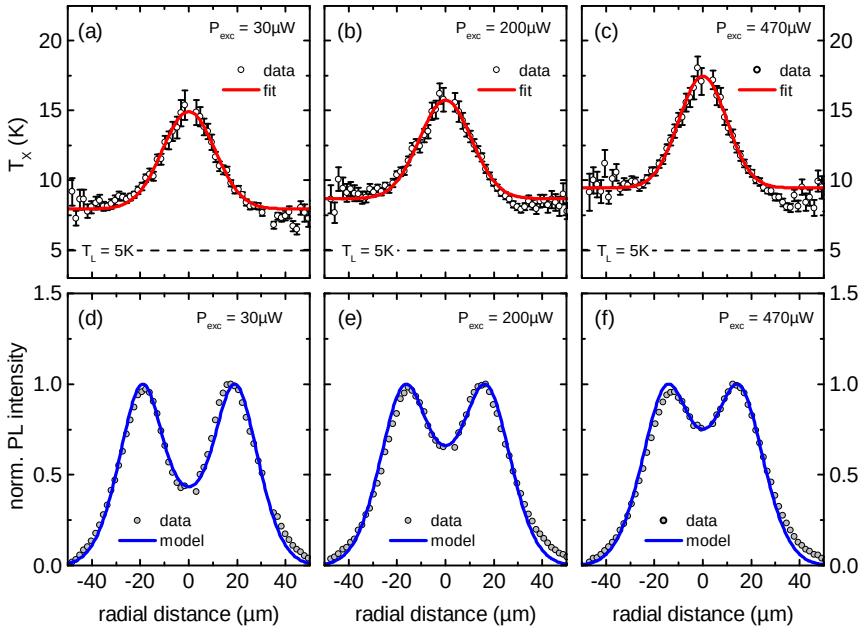

Figure 39: Model description of the free exciton ring formation effect. All measurements are performed at $\lambda_{\mathrm{exc}} = 8050\,\mathrm{\AA}$. (a-c) Exciton temperature profiles obtained from spatially resolved Maxwellian line shape analyses of the $(FX) - 2\hbar\Omega_{\mathrm{LO}}$ transition. The $T_X(r)$ profiles are well described by a Gaussian overheating. (d-f) Data points show the spectrally integrated PL intensity of the second LO-phonon replica, solid blue lines are our model results for the local free exciton density $n_X(r)$. Excellent agreement is obtained by only adjusting the peak photocarrier density $n_0(r=0)$. The stabilization of the exciton at the hot spot for increasing excitation powers (and thus monotonically increasing T_X) is characteristic of the ionization equilibrium between free excitons and unbound electron-hole pairs described by the Saha equation [cf. Fig. 40 (b)].

Our model furthermore provides a very natural explanation for an initially counterintuitive trend observed in the experiment. In the range $0.2\,\mu\mathrm{W} < P_{\mathrm{exc}} < 30\,\mu\mathrm{W}$, the peak-to-valley ratio of the PL quench increases for increasing excitation powers (Fig. 37). This trend is reversed for relatively high excitation powers $P_{\mathrm{exc}} \gtrsim 30\,\mu\mathrm{W}$, although the peak amplitude of the $T_X(r)$ profile increases monotonically with P_{exc} [Figs. 39 (a) - 39 (c)]. The stabilizing effect of an increased total photocarrier density n_0, however, overcompensates further thermal breakup of free excitons at the pump spot and leads to a less pronounced local quench of the free exciton density $n_X(r=0)$ in the high-excitation limit. The trajectories of the SRPL profiles at the respective excitation powers are plotted in Fig. 40 (b) in the Saha phase diagram to visualize that effect.

$g^* \approx 8$, which is in good agreement with our independent estimate for g^* obtained from the time-resolved study of the free exciton photoluminescence rise (chapter 5).

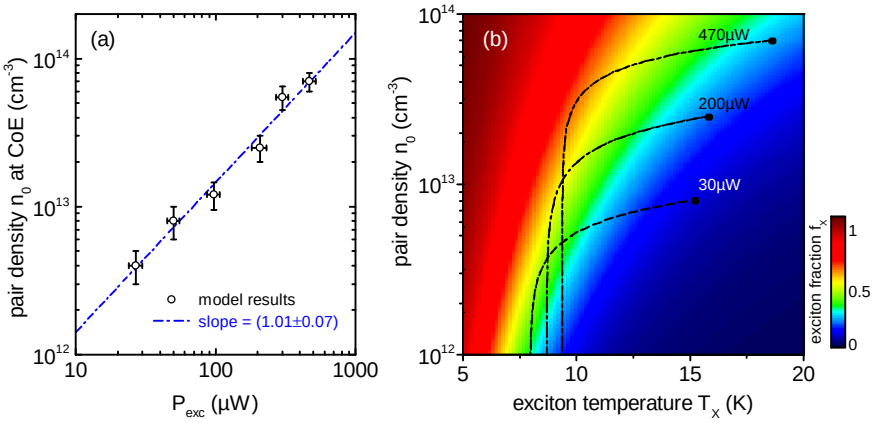

Figure 40: (a) The peak photocarrier pair density $n_0(r=0)$ at the center of excitation (CoE) obtained from our model analysis scales linearly with the optical excitation power P_{exc}. (b) Dashed lines are the trajectories of the model SRPL profiles depicted in Fig. 39. Black circles indicate the center of excitation ($r=0$). The Saha equation provides a natural explanation for the less pronounced quench of the exciton density $n_X(r=0)$ in the high-excitation limit.

9.4 Ring formation under pulsed optical excitation

The free exciton ring formation also occurs prominently in the spatiotemporal expansion of a locally excited photocarrier packet. The excitation power and lattice temperature dependence of the time and spatially resolved PL response to a tightly focused ps laser pulse thereby synopsizes very instructively our understanding of the free exciton luminescence kinetics developed in this thesis.

The time evolution of the SRPL profiles following pulsed excitation is summarized in Fig. 41. As described in section 3.3, the spectrally sliced output of the pulsed "white light" laser source is focused on the sample surface to locally excite a hot photocarrier packet at $t=0$. As time elapses, lateral diffusion causes the spatial expansion of the photocarrier cloud. Simultaneously, the concurrent cooling and dilution of the photocarrier ensemble (by spatial expansion and radiative decay) crucially influence the local thermodynamic equilibrium between free excitons and the uncorrelated electron-hole plasma.

At a moderate excitation power of $P_{\mathrm{exc}}=3\,\mu\mathrm{W}$ [Fig. 41 (a)], we observe a relatively slow (FX) PL onset. The free exciton population maximum is only reached after a significant delay of $\approx 3\,\mathrm{ns}$ with respect to the excitation pulse. Moreover, the free exciton ring formation is clearly seen as a pronounced quench of the (FX) PL intensity in the vicinity of the pump spot. Both effects, i.e., the slow PL rise time and the ring formation, are consistently explained by the time and spatially dependent thermodynamic equilibrium between free excitons and the uncorrelated EHP. As

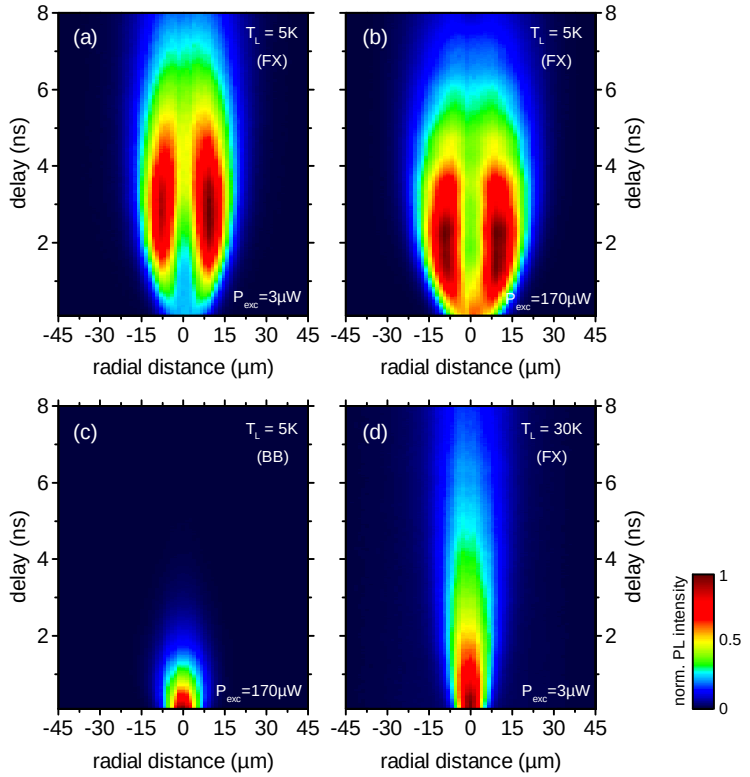

Figure 41: (a,b) Free exciton ring formation under pulsed optical excitation. At high excitation densities, the exciton population peaks at shorter delays, which is consistent with our results and discussion presented in chapter 5. Analogous to continuous wave-optical excitation, local heating causes a quench of the free exciton density at the excitation center, revealing as a macroscopic (FX) PL ring. (c) As expected, the electron-hole plasma does not experience the ring formation effect. (d) At high lattice temperatures, i.e., when the overheating of the photocarrier population ceases, the excitonic ring formation expectedly disappears.

discussed in chapter 5, the transient cooling of the initially hot photocarrier cloud causes the delayed buildup of a free exciton population. At short delays, heating due to nonresonant optical excitation suppresses the formation of free excitons. In this time window, the EHP is thermodynamically favored. Only after sufficient cooling of the entire carrier ensemble, the population balance described by the Saha equation shifts towards the free exciton state. Moreover, the exciton temperature governing the balance between free excitons and the EHP exhibits a strong spatial dependence. Pump-induced heating is most pronounced at the center of optical excitation, which causes the thermal breakup of free excitons in the hot spot region and thus accounts for the ring formation effect.

Figure 41 (b) shows the same measurement performed at a higher excitation power

of $P_{\mathrm{exc}} = 170\,\mu\mathrm{W}$. In superb agreement with our results presented in chapter 5, the arrival of the (FX) PL maximum shifts to shorter delays. Despite the pronounced overheating at early times, an increase of the total pair density $n_0(t=0)$ stabilizes the exciton state and causes the earlier arrival of the free exciton population maximum. The spatial exciton temperature gradient nevertheless manifests as a local quench of the (FX) intensity at the pump spot.

Finally, we perform two measurements that serve as a consistency check for our interpretation of the spatiotemporal kinetics of the free exciton photoluminescence process. Figure 41 (c) depicts the time and spatially resolved PL profiles detected on the direct band-to-band transition (i.e., the uncorrelated electron-hole plasma). In the framework of our model, the free exciton ring formation effect is caused by a spatial exciton temperature gradient, which locally converts free excitons into unbound electron-hole pairs. We, therefore, expect no ring formation of the EHP, which is in perfect agreement with experiment.

We show in Fig. 41 (d) the time evolution of the spatially resolved free exciton PL profiles at $T_L = 30\,\mathrm{K}$. Because of the availability of fast LO phonon emission as an efficient channel for excess energy dissipation at such elevated lattice temperatures (section 2.5.2), the exciton temperature gradient is expected to cease. As seen in Fig. 41 (d), the free exciton ring formation then consistently disappears.

9.5 Summary and conclusion

To summarize, we have observed the formation of macroscopic free exciton photoluminescence rings around a focused laser excitation spot in a high-purity GaAs sample. The dependence of the distinctly shaped SRPL patterns on various experimental parameters provides a particularly instructive visualization of the spatially resolved thermodynamic population balance between free excitons and the uncorrelated EHP described by the Saha equation. Local heating in the carrier system due to off-resonant optical excitation causes the breakup of free excitons into unbound charge carriers. This thermal breakup is potentially countered at high excitation powers by a photocarrier density-induced stabilization of the free exciton state. Our results demonstrate the importance of considering the precise exciton temperature gradients and photocarrier density profiles for a quantitative understanding of excitonic ring formation effects, which were not available in previous related works on electrically biased coupled quantum wells.

The heavy distortions of experimental diffusion profiles due to pump-induced temperature gradients in the carrier system are not limited to continuous-wave (cw) SRPL spectroscopy. One widely employed technique for the determination of charge carrier and exciton diffusion coefficients is photoluminescence spectroscopy with simultaneous time and spatial resolution. Diffusion coefficients are then obtained from the diffusive expansion rate of a Gaussian photocarrier packet [157]. However,

our analysis demonstrates that the momentary diffusion profiles are equally distorted by a pump-induced hot spot. Only in the absence of temperature gradients in the carrier system does an initially Gaussian photocarrier packet remain Gaussian at all times. Analogous to cw SRPL spectroscopy (cf. chapter 7), correct determination of low-temperature photocarrier diffusion coefficients from time and spatially resolved photoluminescence spectroscopy requires strictly resonant optical excitation, a fact which has not been considered in most available SRPL studies.

Chapter 10

Summary

In the present thesis we have investigated the impact of hot exciton effects on the low-temperature time and spatially resolved photoluminescence (PL) response of free excitons in high-purity gallium arsenide (GaAs). The work at hand extends available studies of hot carrier effects, which in bulk GaAs have up to now focused on hot electron populations. In crucial distinction from previous work, we have extensively studied the free exciton second LO-phonon replica. The benefit of this approach is twofold. First, the two LO phonon-assisted radiative recombination allows to circumvent the inherent interpretation ambiguities of the previously investigated free exciton zero-phonon line. Second, the recombination line shape of the second LO-phonon replica provides direct experimental access to the exciton temperature, thereby enabling the *quantitative* assessment of hot exciton effects.

In the first part of the thesis, we have addressed the influence of transient cooling on the time evolution of an initially hot photocarrier ensemble. To this end, we have investigated time-resolved photoluminescence (TRPL) signals detected on the free exciton second LO-phonon replica. Settling a long-standing question, we have shown by comparison with TRPL transients of the free exciton zero-phonon line that the slow free exciton photoluminescence rise following pulsed optical excitation is dominated by the slow buildup of a free exciton population and not by the relaxation of large K vector excitons to the Brillouin zone center. To establish a quantitative picture of the delayed photoluminescence onset, we have determined the cooling dynamics of the initially hot photocarrier cloud from a time-resolved line shape analysis of the second LO-phonon replica. We have demonstrated that the Saha equation, which fundamentally describes the thermodynamic population balance between free excitons and the uncorrelated electron-hole plasma, directly translates the experimentally derived cooling curves into the time-dependent conversion of unbound electron-hole pairs into free excitons.

In the second part of the thesis, we have established the impact of hot exciton effects on low-temperature spatially resolved photoluminescence (SRPL) studies. Such experiments are widely used to investigate charge carrier and free exciton diffusion

in semiconductors and semiconductor nanostructures. By SRPL spectroscopy of the second LO-phonon replica, we have shown that above-band gap focused laser excitation inevitably causes local heating in the carrier system which crucially affects the diffusive expansion of a locally excited exciton packet. Undistorted free exciton diffusion profiles, which are correctly described by the commonly used formulation of the photocarrier diffusion equation, are only observed in the absence of spatial temperature gradients. At low sample temperatures, the reliable determination of free exciton diffusion coefficients from both continuous-wave and time-resolved SRPL spectroscopy requires strictly resonant optical excitation.

Using resonant laser excitation, we have observed the dimensional crossover of free exciton diffusion in etched wire structures of a thin, effectively two-dimensional GaAs epilayer. When the lateral wire width falls below the diffusion length, the sample geometry becomes effectively one-dimensional. The exciton diffusion profile along the wire stripe is then consistently reproduced by the steady-state solution to the one-dimensional diffusion equation.

Finally, we have demonstrated the formation of macroscopic free and bound exciton photoluminescence rings in bulk GaAs around a focused laser excitation spot. Both ring formation effects are due to pump-induced local heating in the exciton system. For a quantitative assessment of the mechanism underlying the free exciton ring formation, we have directly determined the exciton temperature gradient from a spatially resolved line shape analysis of the free exciton second LO-phonon replica. We have demonstrated that a pump-induced hot spot locally modifies the thermodynamic population balance between free excitons and unbound electron-hole pairs described by the Saha equation, which naturally explains the emergence of macroscopic free exciton ring structures.

In summary, we have demonstrated that quantitative consideration of hot exciton effects provides a coherent picture both of the time-domain free exciton luminescence kinetics and of the distinct spatially resolved photoluminescence patterns developing under the influence of spatial photocarrier diffusion.

Bibliography

[1] J. Frenkel. *On the Transformation of light into Heat in Solids. I.* Physical Review **37**, 17 (1931).

[2] G. Wannier. *The Structure of Electronic Excitation Levels in Insulating Crystals*. Physical Review **52**, 191 (1937).

[3] M. Hayashi and K. Katsuki. *Absorption Spectrum of Cuprous Oxide*. Journal of the Physical Society of Japan **5**, 380B (1950).

[4] E. F. Gross and N. A. Karryew. Doklady Akademii Nauk S.S.S.R. **84**, 261 (1952).

[5] J. J. Balmer. *Notiz über die Spectrallinien des Wasserstoffs*. Annalen der Physik **261**, 80 (1885).

[6] S. A. Lyon. *Spectroscopy of hot carriers in semiconductors*. Journal of Luminescence **35**, 121 (1986).

[7] E. Gross, S. Permogorov, and B. Razbirin. *Free exciton motion in crystals and exciton-phonon interaction*. Journal of Physics and Chemistry of Solids **27**, 1647 (1966).

[8] B. Segall and G. D. Mahan. *Phonon-Assisted Recombination of Free Excitons in Compound Semiconductors*. Physical Review **171**, 935 (1968).

[9] M. N. Saha. *LIII. Ionization in the solar chromosphere*. Philosophical Magazine Series 6 **40**, 472 (1920).

[10] W. D. Kraeft, K. Kilimann, and D. Kremp. *Quantum statistics of an electron–hole plasma*. physica status solidi (b) **72**, 461 (1975).

[11] M. Kira, F. Jahnke, and S. Koch. *Microscopic Theory of Excitonic Signatures in Semiconductor Photoluminescence*. Physical Review Letters **81**, 3263 (1998).

[12] S. W. Koch, M. Kira, G. Khitrova, and H. M. Gibbs. *Semiconductor excitons in new light*. Nature Materials **5**, 523 (2006).

[13] D. Snoke, S. Denev, Y. Liu, L. Pfeiffer, and K. West. *Long-range transport in excitonic dark states in coupled quantum wells*. Nature **418**, 754 (2002).

[14] L. V. Butov, A. C. Gossard, and D. S. Chemla. *Macroscopically ordered state in an exciton system*. Nature **418**, 751 (2002).

[15] J. M. Blatt, K. W. Böer, and W. Brandt. *Bose-Einstein Condensation of Excitons*. Physical Review **126**, 1691 (1962).

[16] L. V. Keldysh and A. N. Kozlov. *Collective properties of excitons in semiconductors*. Sov. Phys. JETP **27**, 521 (1968).

[17] D. Snoke. *Spontaneous Bose Coherence of Excitons and Polaritons*. Science **298**, 1368 (2002).

[18] L. Butov, L. Levitov, A. Mintsev, B. Simons, A. Gossard, and D. Chemla. *Formation Mechanism and Low-Temperature Instability of Exciton Rings*. Physical Review Letters **92**, 117404 (2004).

[19] R. Rapaport, G. Chen, D. Snoke, S. Simon, L. Pfeiffer, K. West, Y. Liu, and S. Denev. *Charge Separation of Dense Two-Dimensional Electron-Hole Gases: Mechanism for Exciton Ring Pattern Formation*. Physical Review Letters **92**, 117405 (2004).

[20] G. Chen, R. Rapaport, S. H. Simon, L. Pfeiffer, and K. West. *Dynamics of the in-plane charge separation front in a two-dimensional electron-hole gas*. Physical Review B **71**, 041301 (2005).

[21] A. L. Ivanov, L. E. Smallwood, A. T. Hammack, S. Yang, L. V. Butov, and A. C. Gossard. *Origin of the inner ring in photoluminescence patterns of quantum well excitons*. Europhysics Letters **73**, 920 (2006).

[22] A. T. Hammack, M. Griswold, L. V. Butov, L. E. Smallwood, A. L. Ivanov, and A. C. Gossard. *Trapping of Cold Excitons in Quantum Well Structures with Laser Light*. Physical Review Letters **96**, 227402 (2006).

[23] S. Yang, A. T. Hammack, M. M. Fogler, L. V. Butov, and A. C. Gossard. *Coherence Length of Cold Exciton Gases in Coupled Quantum Wells*. Physical Review Letters **97**, 187402 (2006).

[24] S. Yang, A. V. Mintsev, A. T. Hammack, L. V. Butov, and A. C. Gossard. *Repulsive interaction in the macroscopically ordered exciton state in GaAs/$Al_xGa_{1-x}As$ coupled quantum well structures*. Physical Review B **75**, 033311 (2007).

[25] A. T. Hammack, L. V. Butov, L. Mouchliadis, A. L. Ivanov, and A. C. Gossard. *Kinetics of indirect excitons in an optically induced trap in GaAs quantum wells*. Physical Review B **76**, 193308 (2007).

[26] M. Stern, V. Garmider, E. Segre, M. Rappaport, V. Umansky, Y. Levinson, and I. Bar-Joseph. *Photoluminescence Ring Formation in Coupled Quantum Wells: Excitonic Versus Ambipolar Diffusion*. Physical Review Letters **101**, 257402 (2008).

[27] A. T. Hammack, L. V. Butov, J. Wilkes, L. Mouchliadis, E. A. Muljarov, A. L. Ivanov, and A. C. Gossard. *Kinetics of the inner ring in the exciton emission pattern in coupled GaAs quantum wells*. Physical Review B **80**, 155331 (2009).

[28] S. Yang, L. V. Butov, L. S. Levitov, B. D. Simons, and A. C. Gossard. *Exciton front propagation in photoexcited GaAs quantum wells*. Physical Review B **81**, 115320 (2010).

[29] B. Fluegel, K. Alberi, L. Bhusal, A. Mascarenhas, D. W. Snoke, G. Karunasiri, L. N. Pfeiffer, and K. West. *Exciton pattern generation in GaAs/$Al_xGa_{1-x}As$ multiple quantum wells*. Physical Review B **83**, 195320 (2011).

[30] A. A. High, J. R. Leonard, A. T. Hammack, M. M. Fogler, L. V. Butov, A. V. Kavokin, K. L. Campman, and A. C. Gossard. *Spontaneous coherence in a cold exciton gas*. Nature **483**, 584 (2012).

[31] Y. Y. Kuznetsova, J. R. Leonard, L. V. Butov, J. Wilkes, E. A. Muljarov, K. L. Campman, and A. C. Gossard. *Excitation energy dependence of the exciton inner ring*. Physical Review B **85**, 165452 (2012).

[32] M. Alloing, A. Lemaître, E. Galopin, and F. Dubin. *Nonlinear dynamics and inner-ring photoluminescence pattern of indirect excitons*. Physical Review B **85**, 245106 (2012).

[33] M. Remeika, A. T. Hammack, S. V. Poltavtsev, L. V. Butov, J. Wilkes, A. L. Ivanov, K. L. Campman, M. Hanson, and A. C. Gossard. *Pattern formation in the exciton inner ring*. Physical Review B **88**, 125307 (2013).

[34] M. R. Brozel and G. E. Stillman. *Properties of Gallium Arsenide* (INSPEC, London, 1996).

[35] I. Vurgaftman, J. R. Meyer, and R.-M. L. R. *Band parameters for III–V compound semiconductors and their alloys*. Journal of Applied Physics **89**, 5815 (2001).

[36] C. Kittel. *Introduction to Solid State Physics* (Wiley, Hoboken, 2004).

[37] J. S. Blakemore. *Semiconducting and other major properties of gallium arsenide*. Journal of Applied Physics **53**, R123 (1982).

[38] P. Yu and M. Cardona. *Fundamentals of Semiconductors. Physics and Materials Properties* (Springer, Berlin, 2010).

[39] D. Aspnes. *GaAs lower conduction-band minima: Ordering and properties*. Physical Review B **14**, 5331 (1976).

[40] W. Nakwaski. *Effective masses of electrons and heavy holes in GaAs, InAs, A1As and their ternary compounds*. Physica B: Condensed Matter **210**, 1 (1995).

[41] J. Luttinger. *Quantum Theory of Cyclotron Resonance in Semiconductors: General Theory*. Physical Review **102**, 1030 (1956).

[42] D. L. Dexter and R. S. Knox. *Excitons* (Interscience Publishers, New York, 1965).

[43] A. M. Fox. *Optical Properties of Solids* (Oxford University Press, Oxford, 2001).

[44] R. S. Knox. *Solid state physics. Supplement 5: Theory of excitons* (Academic Press, New York, 1963).

[45] K. Cho. *Unified theory of symmetry-breaking effects on excitons in cubic and wurtzite structures*. Physical Review B **14**, 4463 (1976).

[46] B. H. Bransden and C. J. Joachain. *Physics of Atoms and Molecules* (Prentice Hall, Harlow, 2003).

[47] I. Pelant and J. Valenta. *Luminescence Spectroscopy of Semiconductors* (Oxford University Press, Oxford, 2012).

[48] L. I. Schiff. *Quantum mechanics* (McGraw-Hill, New York, 1968).

[49] J. J. Sakurai and S. F. Tuan. *Modern Quantum Mechanics* (Addison-Wesley Longman, Reading, 2014).

[50] D. Sell. *Resolved Free-Exciton Transitions in the Optical-Absorption Spectrum of GaAs*. Physical Review B **6**, 3750 (1972).

[51] C. J. Hwang. *Lifetimes of free and bound excitons in high-purity GaAs*. Physical Review B **8**, 646 (1973).

[52] G. W. 't Hooft, W. A. J. A. van der Poel, L. W. Molenkamp, and C. T. Foxon. *Giant oscillator strength of free excitons in GaAs*. Physical Review B **35**, 8281 (1987).

[53] E. F. Gross, S. A. Permogorov, and B. S. Razbirin. *Annihilation of excitons and exciton-phonon interaction*. Physics-Uspekhi **14**, 104 (1971).

[54] S. Permogorov. *Hot excitons in semiconductors*. physica status solidi (b) **68**, 9 (1975).

[55] J. Feldmann, G. Peter, E. Göbel, P. Dawson, K. Moore, C. Foxon, and R. J. Elliott. *Linewidth dependence of radiative exciton lifetimes in quantum wells*. Physical Review Letters **59**, 2337 (1987).

[56] J. Hopfield. *Theory of the Contribution of Excitons to the Complex Dielectric Constant of Crystals*. Physical Review **112**, 1555 (1958).

[57] D. D. Sell, S. E. Stokowski, R. Dingle, and J. V. DiLorenzo. *Polariton reflectance and photoluminescence in high-purity GaAs*. Physical Review B **7**, 4568 (1973).

[58] E. Koteles, J. Lee, J. Salerno, and M. Vassell. *Elastic Scattering of Exciton Polaritons by Neutral Impurities*. Physical Review Letters **55**, 867 (1985).

[59] J. Lee, E. S. Koteles, M. O. Vassell, and J. P. Salerno. *Influence of elastic scattering from neutral impurities on the exciton-polariton photoluminescence lineshape in GaAs*. Journal of Luminescence **34**, 63 (1985).

[60] L. Schultheis, J. Kuhl, A. Honold, and C. Tu. *Picosecond Phase Coherence and Orientational Relaxation of Excitons in GaAs*. Physical Review Letters **57**, 1797 (1986).

[61] M. Cardona and G. Güntherodt. *Light Scattering in Solids III. Recent Results* (Springer-Verlag, Berlin, 1982).

[62] E. F. Gross and F. I. Kreingol'd. *Exciton Luminescence in Cu_2O Crystals*. Jetp Letters-Ussr **7**, 218 (1968).

[63] R. M. Habiger and A. Compaan. *Photoluminescence at high exciton densities in cuprous oxide*. Solid State Communications **18**, 1531 (1976).

[64] A. A. O'Connel-Bronin and V. G. Plekhanov. *Resonant Raman scattering in crystals with self-trapping excitons*. physica status solidi (b) **95**, 75 (1979).

[65] R. Weiher and W. Tait. *Contribution of Excitons to the Edge Luminescence in Zinc Oxide*. Physical Review **166**, 791 (1968).

[66] R. Dingle, D. Sell, S. Stokowski, and M. Ilegems. *Absorption, Reflectance, and Luminescence of GaN Epitaxial Layers*. Physical Review B **4**, 1211 (1971).

[67] D. Kovalev, B. Averboukh, D. Volm, B. K. Meyer, H. Amano, and I. Akasaki. *Free exciton emission in GaN*. Physical Review B **54**, 2518 (1996).

[68] B. Monemar, I. A. Buyanova, J. P. Bergman, H. Amano, and I. Akasaki. *Electronic structure and temperature dependence of excitons in GaN*. Materials Science and Engineering B-Solid State Materials for Advanced Technology **43**, 172 (1997).

[69] F. Binet, J. Duboz, J. Off, and F. Scholz. *High-excitation photoluminescence in GaN: Hot-carrier effects and the Mott transition*. Physical Review B **60**, 4715 (1999).

[70] D. Hägele, R. Zimmermann, M. Oestreich, M. Hofmann, W. Rühle, B. Meyer, H. Amano, and I. Akasaki. *Cooling dynamics of excitons in GaN*. Physical Review B **59**, R7797 (1999).

[71] D. Reynolds, D. Look, D. Talwar, G. McCoy, and K. Evans. *Demonstration of semiconductor characterization by phonon sidebands in photoluminescence*. Physical Review B **51**, 2572 (1995).

[72] D. C. Reynolds, D. C. Look, R. Kaspi, and D. N. Talwar. *Phonon replicas in the photoluminescence emission of $Al_xGa_{1-x}As$ alloys*. Applied Physics Letters **66**, 3447 (1995).

[73] J. Aaviksoo, I. Reimand, V. V. Rossin, and V. V. Travnikov. *Kinetics of free-exciton luminescence in GaAs*. Physical Review B **45**, 1473 (1992).

[74] D. Strauch and B. Dorner. *Phonon dispersion in GaAs*. Journal of Physics: Condensed Matter **2**, 1457 (1999).

[75] D. Snoke, W. Rühle, Y. C. Lu, and E. Bauser. *Nonthermalized distribution of electrons on picosecond time scale in GaAs*. Physical Review Letters **68**, 990 (1992).

[76] R. Gilmore. *Saha's Equation and the Partition Function*. URL http://www.physics.drexel.edu/~bob/PHYS317_08/saha.pdf.

[77] B. Diu, C. Guthmann, D. Lederer, and B. Roulet. *Grundlagen der Statistischen Physik* (De Gruyter, Berlin,1994).

[78] G. Bastard. *Wave mechanics applied to semiconductor heterostructures* (Halsted Press, New York, 1988).

[79] D. Semkat, F. Richter, D. Kremp, G. Manzke, W. D. Kraeft, and K. Henneberger. *Ionization equilibrium in an excited semiconductor: Mott transition versus Bose-Einstein condensation*. Physical Review B **80**, 155201 (2009).

[80] S. N. F. Mott. *Metal-insulator transitions* (Taylor & Francis, London, 1974).

[81] G. Manzke, D. Semkat, and H. Stolz. *Mott transition of excitons in GaAs-GaAlAs quantum wells*. New Journal of Physics **14**, 095002 (2012).

[82] H. Haug and S. Schmitt-Rink. *Electron Theory of the Optical-Properties of Laser-Excited Semiconductors*. Progress in Quantum Electronics **9**, 3 (1984).

[83] A. Amo, M. D. Martin, L. Viña, A. I. Toropov, and K. S. Zhuravlev. *Interplay of exciton and electron-hole plasma recombination on the photoluminescence dynamics in bulk GaAs*. Physical Review B **73**, 035205 (2006).

[84] E. M. Conwell. *High Field Transport in Semiconductors* (Academic Press, New York, 1967).

[85] J. Shah. *Ultrafast Spectroscopy of Semiconductors and Semiconductor Nanostructures* (Springer, Berlin, 1999).

[86] B. R. Nag. *Theory of electrical transport in semiconductors* (Pergamon Press, Oxford, 1972).

[87] B. R. Nag. *Electron Transport in Compound Semiconductors* (Springer, Berlin, 1980).

[88] J. Shah and R. Leite. *Radiative Recombination from Photoexcited Hot Carriers in GaAs*. Physical Review Letters **22**, 1304 (1969).

[89] L. Schultheis, J. Kuhl, A. Honold, and C. W. Tu. *Ultrafast Phase Relaxation of Excitons via Exciton-Exciton and Exciton-Electron Collisions*. Physical Review Letters **57**, 1635 (1986).

[90] L. Schultheis, A. Honold, J. Kuhl, K. Köhler, and C. Tu. *Optical dephasing of homogeneously broadened two-dimensional exciton transitions in GaAs quantum wells*. Physical Review B **34**, 9027 (1986).

[91] E. Göbel, K. Leo, T. Damen, J. Shah, S. Schmitt-Rink, W. Schäfer, J. Müller, and K. Köhler. *Quantum beats of excitons in quantum wells*. Physical Review Letters **64**, 1801 (1990).

[92] D. Fröhlich, A. Nöthe, and K. Reimann. *Observation of the Resonant Optical Stark Effect in a Semiconductor*. Physical Review Letters **55**, 1335 (1985).

[93] A. Mysyrowicz, D. Hulin, A. Antonetti, A. Migus, W. Masselink, and H. Morkoç. *"Dressed Excitons" in a Multiple-Quantum-Well Structure: Evidence for an Optical Stark Effect with Femtosecond Response Time*. Physical Review Letters **56**, 2748 (1986).

[94] J. Feldmann, K. Leo, J. Shah, D. Miller, J. Cunningham, T. Meier, G. von Plessen, A. Schulze, P. Thomas, and S. Schmitt-Rink. *Optical investigation of Bloch oscillations in a semiconductor superlattice*. Physical Review B **46**, 7252 (1992).

[95] J. Collet and T. Amand. *Model calculation of the laser-semiconductor interaction in subpicosecond regime*. Journal of Physics and Chemistry of Solids **47**, 153 (1986).

[96] J. Oudar, D. Hulin, A. Migus, A. Antonetti, and F. Alexandre. *Subpicosecond Spectral Hole Burning Due to Nonthermalized Photoexcited Carriers in GaAs*. Physical Review Letters **55**, 2074 (1985).

[97] C. Tang and D. Erskine. *Femtosecond Relaxation of Photoexcited Nonequilibrium Carriers in $Al_xGa_{1-x}As$*. Physical Review Letters **51**, 840 (1983).

[98] T. Elsaesser, J. Shah, L. Rota, and P. Lugli. *Initial thermalization of photoexcited carriers in GaAs studied by femtosecond luminescence spectroscopy*. Physical Review Letters **66**, 1757 (1991).

[99] R. Ulbrich. *Energy relaxation of photoexcited hot electrons in GaAs*. Physical Review B **8**, 5719 (1973).

[100] R. F. Leheny, J. Shah, R. L. Fork, C. V. Shank, and A. Migus. *Dynamics of hot carrier cooling in photo-excited GaAs*. Solid State Communications **31**, 809 (1979).

[101] D. Von der Linde and R. Lambrich. *Direct measurement of hot-electron relaxation by picosecond spectroscopy*. Physical Review Letters **42**, 1090 (1979).

[102] H. Münzel, D. Bimberg, and A. Steckenborn. *Direct evidence for screening of carrier – acoustic phonon interaction at low to medium carrier densities in GaAs*. Physica B+C **117-118**, 214 (1983).

[103] D. M. Eagles. *Optical absorption and recombination radiation in semiconductors due to transitions between hydrogen-like acceptor impurity levels and the conduction band*. Journal of Physics and Chemistry of Solids **16**, 76 (1960).

[104] T. Kiessling, J. H. Quast, A. Kreisel, T. Henn, W. Ossau, and L. W. Molenkamp. *Spatially resolved photocarrier energy relaxation in low-doped bulk GaAs*. Physical Review B **86**, 161201 (2012).

[105] C. Weisbuch. *Photocarrier thermalization by laser excitation spectroscopy*. Solid-State Electronics **21**, 179 (1978).

[106] J. Shah, C. Lin, R. F. Leheny, and A. E. DiGiovanni. *Pump wavelength dependence of hot electron temperature in GaAs*. Solid State Communications **18**, 487 (1976).

[107] E. Göbel and O. Hildebrand. *Thermalization of the Electron-Hole Plasma in GaAs.* physica status solidi (b) **88**, 645 (1978).

[108] J. Shah. *Hot electrons and phonons under high intensity photoexcitation of semiconductors*. Solid-State Electronics **21**, 43 (1978).

[109] W. Becker. *Advanced Time-Correlated Single Photon Counting Techniques* (Springer, Berlin, 2005).

[110] T. Henn, T. Kiessling, W. Ossau, L. W. Molenkamp, K. Biermann, and P. V. Santos. *Ultrafast supercontinuum fiber-laser based pump-probe scanning magneto-optical Kerr effect microscope for the investigation of electron spin dynamics in semiconductors at cryogenic temperatures with picosecond time and micrometer spatial resolution*. Review of Scientific Instruments **84**, 123903 (2013).

[111] JENOPTIK Optical Systems GmbH. *Integrated-optical modulators. Technical information and instructions for use*. URL http://www.jenoptik.com/cms/jenoptik.nsf/res/Modulatorfibel_en.pdf/$file/Modulatorfibel_en.pdf.

[112] H. J. Queisser and K. Stierstadt. *Persönliches: Nachruf auf Elisabeth Bauser*. Physikalische Blätter **53**, 49 (1997).

[113] A. M. White, P. J. Dean, and B. Day. *On the origin of bound exciton lines in indium phosphide and gallium arsenide*. Journal of Physics C: Solid State Physics **7**, 1400 (1974).

[114] U. Heim and P. Hiesinger. *Luminescence and Excitation Spectra of Exciton Emission in GaAs*. physica status solidi (b) **66**, 461 (1974).

[115] E. H. Bogardus and H. B. Bebb. *Bound-Exciton, Free-Exciton, Band-Acceptor, Donor-Acceptor, and Auger Recombination in GaAs*. Physical Review **176**, 993 (1968).

[116] R. J. Nelson and R. G. Sobers. *Minority-carrier lifetimes and internal quantum efficiency of surface-free GaAs*. Journal of Applied Physics **49**, 6103 (1978).

[117] H. Künzel and K. Ploog. *The effect of As_2 and As_4 molecular beam species on photoluminescence of molecular beam epitaxially grown GaAs*. Applied Physics Letters **37**, 416 (1980).

[118] J. P. Contour. *An optical characterization of defect levels induced by MBE growth of GaAs*. Journal of Vacuum Science & Technology B: Microelectronics and Nanometer Structures **1**, 811 (1983).

[119] R. Leite, J. Shah, and J. Gordon. *Effect of Electron-Exciton Collisions on the Free-Exciton Linewidth in Epitaxial GaAs*. Physical Review Letters **23**, 1332 (1969).

[120] Y. P. Varshni. *Temperature dependence of the energy gap in semiconductors*. Physica **34**, 149 (1967).

[121] K. P. O'Donnell and X. Chen. *Temperature dependence of semiconductor band gaps*. Applied Physics Letters **58**, 2924 (1991).

[122] J. Szczytko, L. Kappei, J. Berney, and F. Morier-Genoud. *Determination of the exciton formation in quantum wells from time-resolved interband luminescence*. Physical Review Letters **93**, 137401 (2004).

[123] P. E. Selbmann, M. Gulia, F. Rossi, E. Molinari, and P. Lugli. *Coupled free-carrier and exciton relaxation in optically excited semiconductors*. Physical Review B **54**, 4660 (1996).

[124] O. Brandt, J. Ringling, K. H. Ploog, H.-J. Wünsche, and F. Henneberger. *Temperature dependence of the radiative lifetime in GaN*. Physical Review B **58**, R15977 (1998).

[125] A. Amo, M. D. Martin, . Kłopotowski, L. Viña, A. I. Toropov, and K. S. Zhuravlev. *Influence of trapping on the exciton dynamics of $Al_xGa_{1-x}As$ films*. Applied Physics Letters **86**, 111906 (2005).

[126] R. Höger, E. Göbel, J. Kuhl, K. Ploog, and H. J. Quiesser. *Kinetics of free and bound excitons in GaAs/AlGaAs double heterostructures*. Journal of Physics C: Solid State Physics **17**, L905 (1984).

[127] F. Münzhuber, T. Henn, T. Kiessling, W. Ossau, L. W. Molenkamp, B. Gieseking, G. V. Astakhov, and V. Dyakonov. *Exciton decay dynamics controlled by impurity occupation in strongly Mn-doped and partially compensated bulk GaAs*. Physical Review B **90**, 125203 (2014).

[128] J.-i. Kusano, Y. Segawa, Y. Aoyagi, S. Namba, and H. Okamoto. *Extremely slow energy relaxation of a two-dimensional exciton in a GaAs superlattice structure*. Physical Review B **40**, 1685 (1989).

[129] T. Damen, J. Shah, D. Oberli, D. Chemla, J. Cunningham, and J. Kuo. *Dynamics of exciton formation and relaxation in GaAs quantum wells*. Physical Review B **42**, 7434 (1990).

[130] R. Eccleston, R. Strobel, W. W. Rühle, J. Kuhl, B. F. Feuerbacher, and K. Ploog. *Exciton dynamics in a GaAs quantum well*. Physical Review B **44**, 1395 (1991).

[131] P. Roussignol, C. Delalande, A. Vinattieri, L. Carraresi, and M. Colocci. *Dynamics of exciton relaxation in GaAs/$Al_xGa_{1-x}As$ quantum wells*. Physical Review B **45**, 6965 (1992).

[132] T. Amand, B. Dareys, B. Baylac, X. Marie, J. Barrau, M. Brousseau, D. Dunstan, and R. Planel. *Exciton formation and hole-spin relaxation in intrinsic quantum wells*. Physical Review B **50**, 11624 (1994).

[133] H. W. Yoon, D. R. Wake, and J. P. Wolfe. *Effect of exciton-carrier thermodynamics on the GaAs quantum well photoluminescence*. Physical Review B **54**, 2763 (1996).

[134] M. Gulia, F. Rossi, E. Molinari, P. E. Selbmann, and P. Lugli. *Phonon-assisted exciton formation and relaxation in GaAs/$Al_xGa_{1-x}As$ quantum wells*. Physical Review B **55**, R16049 (1997).

[135] M. Gurioli, P. Borri, M. Colocci, M. Gulia, F. Rossi, E. Molinari, P. Selbmann, and P. Lugli. *Exciton formation and relaxation in GaAs epilayers*. Physical Review B **58**, R13403 (1998).

[136] I. Reimand and J. Aaviksoo. *Exciton interaction with hot electrons in GaAs*. Physical Review B **61**, 16653 (2000).

[137] S. Bieker, T. Henn, T. Kiessling, W. Ossau, and L. W. Molenkamp. *Spatially Resolved Thermodynamics of the Partially Ionized Exciton Gas in GaAs*. Physical Review Letters **114**, 227402 (2015).

[138] R. A. Kaindl, D. Hägele, M. A. Carnahan, and D. S. Chemla. *Transient terahertz spectroscopy of excitons and unbound carriers in quasi-two-dimensional electron-hole gases*. Physical Review B **79**, 045320 (2009).

[139] D. Bimberg and J. Mycielski. *Recombination-induced heating of free carriers in a semiconductor*. Physical Review B **31**, 5490 (1985).

[140] A. L. Ivanov. *Thermalization and photoluminescence dynamics of indirect excitons at low bath temperatures*. Journal of Physics: Condensed Matter **16**, S3629 (2004).

[141] S. Bieker, T. Henn, T. Kiessling, W. Ossau, and L. W. Molenkamp. *Excitonic ring formation in ultrapure bulk GaAs*. Physical Review B **90**, 201305(R) (2014).

[142] J. Crank. *The Mathematics of Diffusion* (Clarendon Press, Oxford, 1979).

[143] F. Pulizzi, W. H. A. Thijssen, P. C. M. Christianen, and J. C. Maan. *Diffusion of two dimensional magnetoexcitons*. Physica B: Condensed Matter **298**, 441 (2001).

[144] F. Pulizzi, D. Sanvitto, P. C. M. Christianen, A. J. Shields, S. N. Holmes, M. Y. Simmons, D. A. Ritchie, M. Pepper, and J. C. Maan. *Optical imaging of trion diffusion and drift in GaAs quantum wells*. Physical Review B **68**, 205304 (2003).

[145] D. J. Wolford, G. D. Gilliland, T. F. Kuech, J. A. Bradley, and H. P. Hjalmarson. *Optically determined minority-carrier transport in GaAs/$Al_xGa_{1-x}As$ heterostructures*. Physical Review B **47**, 15601 (1993).

[146] T. Myint-U and L. Debnath. *Linear Partial Differential Equations for Scientists and Engineers* (Birkhäuser, Boston, 2007).

[147] M. Furis, D. L. Smith, S. Kos, E. S. Garlid, K. S. M. Reddy, C. J. Palmstrøm, P. A. Crowell, and S. A. Crooker. *Local Hanle-effect studies of spin drift and diffusion in n:GaAs epilayers and spin-transport devices*. New Journal of Physics **9**, 347 (2007).

[148] C. M. Wolfe. *Electron Mobility in High-Purity GaAs*. Journal of Applied Physics **41**, 3088 (1970).

[149] J. P. Wolfe. *Imaging of excitonic transport in semiconductors*. Journal of Luminescence **53**, 327 (1992).

[150] J. Erland, B. Razbirin, K. H. Pantke, V. Lyssenko, and J. Hvam. *Exciton diffusion in CdSe*. Physical Review B **47**, 3582 (1993).

[151] B. A. Ruzicka, L. K. Werake, H. Samassekou, and H. Zhao. *Ambipolar diffusion of photoexcited carriers in bulk GaAs*. Applied Physics Letters **97**, 262119 (2010).

[152] J. H. Quast, T. Henn, T. Kiessling, W. Ossau, L. W. Molenkamp, D. Reuter, and A. D. Wieck. *Hot carrier effects on lateral electron spin diffusion in n-type GaAs*. Physical Review B **87**, 205203 (2013).

[153] T. Henn, T. Kiessling, W. Ossau, L. W. Molenkamp, D. Reuter, and A. D. Wieck. *Picosecond real-space imaging of electron spin diffusion in GaAs*. Physical Review B **88**, 195202 (2013).

[154] G. Mayer, B. E. Maile, R. Germann, A. Forchel, P. Grambow, and H. P. Meier. *Time-resolved investigations of sidewall recombination in dry-etched GaAs wires*. Applied Physics Letters **56**, 2016 (1990).

[155] R. Spiegel, G. Bacher, K. Herz, M. Illing, T. Kümmell, A. Forchel, B. Jobst, D. Hommel, G. Landwehr, J. Söllner, and M. Heuken. *Excitonic lifetimes in (Zn,Cd)Se/ZnSe and ZnSe/Zn(Se,S) quantum wires*. Physical Review B **53**, R4233 (1996).

[156] S. V. Andreev, A. A. Varlamov, and A. V. Kavokin. *Scale Invariance and Universality in a Cold Gas of Indirect Excitons*. Physical Review Letters **112**, 036401 (2014).

[157] H. Yoon, D. Wake, J. Wolfe, and H. Morkoç. *In-plane transport of photoexcited carriers in GaAs quantum wells*. Physical Review B **46**, 13461 (1992).

Deutsche Zusammenfassung

In der vorliegenden Arbeit wurde der Einfluss von Überheizungseffekten aufgrund nichtresonanter optischer Anregung auf die orts- und zeitaufgelöste Photolumineszenz-Dynamik freier Exzitonen in hochreinem Galliumarsenid (GaAs) untersucht. Die Arbeit baut damit vorhandene Studien von Überheizungseffekten aus, welche sich in Volumen-GaAs vornehmlich auf die Untersuchung heißer Elektronenpopulationen konzentriert haben. In Abgrenzung zu vorherigen Studien erfolgte eine umfängliche Untersuchung der zweiten LO-Phonon Replik des freien Exzitons. Dieser Ansatz bietet zweifachen Nutzen. Zum einen können durch die Betrachtung des strahlenden Zerfalls freier Exzitonen unter gleichzeitiger Emission zweier LO Phononen die inhärenten Mehrdeutigkeiten bei der Interpretation der direkten Lumineszenz freier Exzitonen umgangen werden. Des Weiteren gestattet eine Linienformanalyse der zweiten LO-Phonon Replik die direkte experimentelle Bestimmung der Exzitonentemperatur und schafft damit die Voraussetzung zur *quantitativen* Untersuchung von Überheizungseffekten im Exzitonensystem.

Im ersten Teil der Arbeit wurde der Einfluss des transienten Kühlens auf die Zeitentwicklung eines anfänglich heißen Ladungsträgerensembles untersucht. Durch einen Vergleich des Signalverlaufs der direkten Exzitonenlumineszenz mit der zweiten LO-Phonon Replik konnte zweifelsfrei gezeigt werden, dass der verzögerte Anstieg der Exzitonenlumineszenz durch den relativ langsamen Aufbau einer Exzitonenpopulation dominiert wird und nicht lediglich die Relaxation von Exzitonen mit großen K-Vektoren zum Zentrum der Brillouinzone widerspiegelt. Zum quantitativen Verständnis des verzögerten Lumineszenzanstiegs wurde das Abkühlverhalten des anfänglich heißen Ladungsträgerensembles durch eine zeitaufgelöste Linienformanalyse der zweiten LO-Phonon Replik bestimmt. Es wurde gezeigt, dass die Saha-Gleichung, welche das thermodynamische Populations-Gleichgewicht zwischen freien Exzitonen und dem unkorrelierten Elektron-Loch-Plasma beschreibt, die experimentell bestimmten Kühlkurven direkt in die zeitabhängige Umwandlung von ungebundenen Elektron-Loch-Paaren in freie Exzitonen übersetzt.

Im zweiten Teil der Arbeit wurden die Auswirkungen von Überheizungseffekten im Exzitonensystem auf ortsaufgelöste Photolumineszenzmessungen bei tiefen Gittertemperaturen untersucht. Experimente dieser Art werden häufig zur Bestimmung von

Ladungsträger- und Exzitonen-Diffusionskoeffizienten in Halbleitern und Halbleiter-Nanostrukturen genutzt. Durch die ortsaufgelöste Auswertung der zweiten LO-Phonon Replik konnte gezeigt werden, dass fokussierte nichtresonante Laseranregung unweigerlich zu einer lokalen Überheizung des Ladungsträgersystems führt. Solche optisch induzierten Temperaturgradienten beeinflussen entscheidend die diffusive Ausbreitung eines lokal erzeugten Exzitonen-Pakets. Unverfälschte Diffusionsprofile, die korrekt durch die üblicherweise herangezogene Formulierung der Diffusionsgleichung beschrieben werden, sind ausschließlich bei Nichtanwesenheit von räumlichen Temperaturgradienten beobachtbar. Die verlässliche Bestimmung von Exzitonen-Diffusionskoeffizienten sowohl mittels zeitaufgelöster als auch stationärer ortsaufgelöster Photolumineszenzspektroskopie erfordert daher scharf resonante optische Anregung.

Unter resonanter Laseranregung konnte der Übergang von einem effektiv zweidimensionalen zu einem effektiv eindimensionalen Diffusionsverhalten freier Exzitonen in geätzten GaAs-Strukturen beobachtet werden. Die untersuchten Streifenstrukturen wurden in eine dünne, effektiv zweidimensionale GaAs-Epischicht geätzt. Der dimensionale Übergang vollzieht sich, wenn die laterale Abmessung der geätzten Struktur die Diffusionslänge unterschreitet. Das stationäre Exzitonen-Diffusionsprofil wird dann korrekt durch die Lösung der eindimensionalen Diffusionsgleichung beschrieben.

Abschließend wurde die Bildung makroskopischer Ringstrukturen freier und gebundener Exzitonen in Volumen-GaAs um einen fokussierten Laserspot demonstriert. Beide Ringstrukturen resultieren aus lokalen Überheizungen des Exzitonensystems, die durch nichtresonante optische Anregung hervorgerufen werden. Zum quantitativen Verständnis des zugrunde liegenden Mechanismus für die Entstehung der beobachteten Ringstrukturen wurde der Temperaturgradient im Exzitonensystem durch eine ortsaufgelöste Linienformanalyse der zweiten LO-Phonon Replik bestimmt. Es wurde gezeigt, dass die Ringstrukturen freier Exzitonen auf natürliche Weise durch das lokale thermodynamische Saha-Gleichgewicht zwischen Exzitonen und ungebundenen Elektron-Loch-Paaren entstehen.

Zusammenfassend wurde gezeigt, dass die quantitative Berücksichtigung von Überheizungseffekten im Exzitonensystem zu einem kohärenten Gesamtbild des Lumineszenzprozesses führt, welches sowohl die zeitaufgelöste Lumineszenzkinetik freier Exzitonen als auch das Auftreten exzitonischer Ringstrukturen unter dem Einfluss räumlicher Ladungsträgerdiffusion erklärt.

Acknowledgements

I wish to express my gratitude to all people who supported me during my doctoral studies and who contributed to the success of the present thesis. Among all colleagues and coauthors, I am particularly indebted to

- Prof. Dr. Wolfgang Ossau for the supervision of my thesis,
- Dr. Tobias Kießling for fruitful discussions,
- Prof. Dr. Laurens W. Molenkamp for providing access to the laboratory facilities of his chair Experimentelle Physik III and for financial funding of my doctoral studies,
- Michael Beck and his colleagues at the Institut für Festkörperphysik, Universität Hannover for cooperation with the investigation of the free exciton photoluminescence rise,
- Raul Stühler for his cooperation with the investigation of geometry effects on free exciton diffusion in etched GaAs wire structures,
- Dr. Tatiana Borzenko, Johannes Brehm, and Adriana Wolf (Technische Physik, Universität Würzburg) for their help with sample fabrication and SEM imaging,
- and Dr. Tobias Henn and Dr. Franz Münzhuber for their friendship and for countless fruitful discussions during the last five years.

Finally, I wholeheartedly thank my wife Sara Anna for her love and unconditional support in whatever I am doing.